Tactile Sensing for Assistive Robotics

by

Emmett Kerr, BEng, MSc.

A Thesis submitted to
Ulster University
for the degree of Ph.D.
in the
Faculty of Computing, Engineering & the Built Environment

May 2018
I confirm that the word count of this thesis is less than 100,000 words

This thesis is dedicated to my wife, Gemma, and my parents, Garvin and Marie Kerr.

CONTENTS

LIST OF TABLES

LIST OF FIGURES

ACKNOWLEDGEMENTS

It is with pleasure that I would like to take this opportunity to thank everyone who was involved in my PhD. Firstly, I would like to sincerely thank my supervisors, Prof. Martin McGinnity and Prof. Sonya Coleman. Their help, guidance and support both academically and personally have been invaluable over the course of my research. Without their time, dedication and advice my time spent as a PhD student would not have been as fruitful. I would like to add a special note of thanks to Mrs. Andrea Shepherd, a medical professional and lecturer of Nursing who provided me with medical advice and guidance for the measurement of vital signs. Without Andrea's input, understanding human vital signs, knowing how to measure them correctly and carrying out data collection on human subjects would not have been possible.

I would like to thank the Department for Employment and Learning (DEL) who provided financial funding for my research project and several conferences over the course of my studies.

I would like to say a heartfelt word of thanks to my colleagues and friends in the Intelligent Systems Research Centre (ISRC). I have been very fortunate to work in a centre with extremely supportive, friendly and intelligent colleagues and friends and I have no doubt that without their friendship and our "tea-time discussions", my PhD journey would have been a little more difficult. I would like to pay a special word of thanks to Dr. Philip Vance, Dr. John Wade, Dr. Dermot Kerr and Dr. Bryan Gardiner for their friendship, advice and continuous support throughout my PhD journey. I would like to thank my friends outside of Ulster University for helping me take my mind of my work when things got tough. In particular, I would like to thank my fellow Sensei's, training partners and friends at Oakleaf Ju-Jitsu Federation. Training sessions at our federation have helped me switch off and provided me with stress relief which, without a doubt, was invaluable to progressing with my research.

Most importantly, I would like to thank my wife, Gemma, and my family. My mum and dad, Garvin and Marie, thank you for always being there to support me through the rough and smooth. You are the most supportive and loving parents anyone could wish for and I would not be where I am today without you. My sister, Dr. Karen Kerr, I am proud to follow in your footsteps and thank you so much for all your support and advice in my research journey to

date and I look forward to that joint publication! My brother, Garvin, thank you for always being there and giving me endless words of encouragement and tears of laughter! Finally, my wife and best friend, my wee Gem. You are my rock and I would be truly lost without you! Thank you for your continuous and unlimited understanding, patience, support and encouragement throughout my PhD journey. You have always been there to listen to me, give advice and pick me up every time I struggled. You have believed in me every second of this journey, even when I may have doubted myself. You have helped me stay focussed on my goals, see things clearly and keep calm under pressure. Without your continuous support, encouragement and love my success simply would not have been possible.

ABSTRACT

Humans perceive the world through information gathered by their five senses. Attempting to replicate some of these senses in intelligent systems has been a focus of research for many years. Due to high quality vision sensors such as cameras and laser scanners being readily available at a relatively low cost for some time now, vision sensing has been heavily researched for many decades enabling systems to distinguish a lot of information such as the size, shape and colour of objects or materials. However, there are attributes of objects, materials and the environment that cannot be determined by vision sensing alone such as compressibility, thermal properties or sub-surface vibration.

This thesis presents methods which demonstrate that tactile sensing can be used to assess a human's current state of health by measuring their vital signs using a biomimetic fingertip, namely BioTAC. It involves three main contributions. The first contribution is a method for classifying materials from tactile sensing alone. Using machine learning approaches, the high sensitivity of the BioTAC tactile sensors is demonstrated via the ability to classify different (and similar) material with high accuracy based on surface texture and thermal properties. The second contribution focuses on the use of the BioTAC fingertip to accurately measure the vital signs of a human by mimicking medical professionals. Algorithms have been developed and evaluated for determining a human's Beats Per Minute (BPM), Pulse to Pulse Interval (PPI), Respiratory Rate (RR), Breath to Breath Interval (BBI) via tactile sensing. Furthermore, algorithms have been developed to measure Capillary Refill Time (CRT) by using a combination of tactile sensing for the control of a robot fingertip and vision sensing to analyse changes in the subjects skin colour. The final contribution is a fuzzy classification algorithm capable of classifying the human's health status based on their BPM, RR and CRT.

Significant contributions in the field of tactile sensing presented in this thesis demonstrate that a robotic system can determine a human's current status of health. This could play a vital role in helping to rescue victims of a disaster or emergency by performing medical triage and determining an order of treatment. In turn, emergency personnel will be able to make a more informed decision on how they should allocate their valuable resources thus preventing unnecessary risk and reducing the further loss of human life.

"Learning is a process of discovery - a process without end."

Bruce Lee

Note on Access to Content

I hereby declare that for 2 years following the date on which the thesis is deposited in Research Student Administration of Ulster University, the thesis shall remain confidential with access or copying prohibited. Following expiry of this period I permit

- the Librarian of the University to allow the thesis to be copied in whole or in part without reference to me on the understanding that such authority applies to the provision of single copies made for study purposes or for inclusion within the stock of another library.
- the thesis to be made available through the Ulster Institutional Repository and/or EThOS under the terms of the Ulster eTheses Deposit Agreement which I have signed.

IT IS A CONDITION OF USE OF THIS THESIS THAT ANYONE WHO CONSULTS IT MUST RECOGNISE THAT THE COPYRIGHT RESTS WITH THE UNIVERSITY AND THEN SUBSEQUENTLY TO THE AUTHOR ON THE EXPIRY OF THIS PERIOD AND THAT NO QUOTATION FROM THE THESIS AND NO INFORMATION DERIVED FROM IT MAY BE PUBLISHED UNLESS THE SOURCE IS PROPERLY ACKNOWLEDGED.

_____

Name

Date

LIST OF ABBREVIATIONS

μMAC Mean Maximum Covariance Analysis. 42

p order of the polynomial kernel. 64, 65

***k*-NN** k-Nearest Neighbour. ii, 27, 32, 33, 36, 38, 41, 44, 49, 53, 72–74, 139

2SFF 2 Stage Filtering Fully-automatic. 108–110, 112, 113, 164, 165, 167, 168, 170, 172–174

2SFS 2 Stage Filtering Semi-automatic. 108–110, 112, 113, 164, 165, 167, 168, 170, 172–174

3SFF 3 Stage Filtering Fully-automatic. 108–110, 112, 113, 164, 166, 167, 169, 171–174

3SFS 3 Stage Filtering Semi-automatic. 108–110, 112, 113, 164, 166, 167, 169, 171–174

AED automated external defibrillator. 129

ANN Artificial Neural Networks. ii, iii, v, vi, 27–29, 37, 38, 44, 46, 48, 49, 53, 60, 63, 68–71, 73, 74, 95, 130, 139

BBI Breath to Breath Interval. iii, v, x, 83, 97, 99, 111–113, 117, 144, 164, 173, 174

BCG ballistocardiogram. 85

BoW Bag-of-Words. 35, 36

BPM Beats Per Minute. v, vii, x, 2–6, 82–84, 86–89, 95–97, 99, 105, 108–113, 116, 117, 120, 121, 130–132, 134–137, 139–142, 144, 164–167

BRL Bristol Robotics Laboratory. 17

CCD charge-coupled device. 16, 36

CI Computational Intelligence. 27

CMOS complementary metal-oxide semiconductor. 16, 86

CNS Central Nervous System. 8, 84, 134

CO cardiac output. 85

CRT Capillary Refill Time. iii, v, vii, x, 2–6, 51, 84, 88, 89, 116, 119–123, 125–128, 130–132, 134–137, 140–142, 144, 175

DOF Degrees of Freedom. 46, 47

DWT discrete wavelet transform. 38, 94, 95, 100, 108, 117, 164

ECG electrocardiogram. 83, 85, 97, 120

EM expectation maximisation. 30, 39, 40, 71

EMG Electromyography. 143

F/T Force/Torque. 57, 92, 122

FF first finger. 90–92

FFT Fast Fourier Transform. 99

FIR finite impulse response. 93

fps frames per second. 123

FSR Force Sensing Resistor. 13

gmf gram-force. 11

GMM Gaussian Mixture Model. ii, 27, 30, 46, 48, 49, 53, 71, 73, 74, 139

GUI Graphical User Interface. vi, 57, 58, 91

HD High Definition. 5

HMM Hidden Markov Model. 41

ICT Information and Communications Technology. 3

IIR infinite impulse response. 93, 99, 100

ISRC Intelligent Systems Research Centre. vi, viii, 15, 90

KF kernel function. v, 29, 63–67, 70, 74

LBP Local Binary Pattern. 37

LDA Linear Discriminant Analysis. ii, 27, 30, 31, 38, 53, 71, 73, 74, 139

LKF linear kernel function. v, 64, 65

LMPKF multi-layer perceptron kernel function. v, 64–66

LS least-squares. 64–66

MDF medium-density fibreboard. 55, 56, 77

MEMS Micro Electro Mechanical Systems. 11

MF middle finger. 39, 90–92

MLBP Multi-scale Local Binary Pattern. 37

MLP Multi-Layer Perceptron. v, 27, 29, 53, 65, 72–74, 139

N Newton. 11, 16, 45

NB Naïve Bayes. ii, 27, 31, 37–39, 42, 44, 53, 71, 73, 74, 139

NHS National Health Service. 131, 137

NN Neural Networks. 27

PA Passive Aggressive Online Learning. 40

PAC dynamic fluid pressure. v, vi, 24, 25, 55, 58, 59, 61, 89, 91, 92, 96, 100, 101, 104–107, 172

PC principal component. 59, 60, 63, 77

PCA principal component analysis. 21, 31, 38, 41, 42, 53, 59, 60, 63, 77, 139

PDC absolute fluid pressure. v–vii, 24, 25, 55, 58, 59, 61, 89, 91, 92, 96, 100, 102, 104–106, 108, 110–112, 167–169, 173

PDF probability density function. 30

PEP pre-ejection period. 85

PKF polynomial kernel function. v, 64–66

PPG photoplethysmography. 85, 86, 89

PPI Pulse to Pulse Interval. iii, v, vii, x, 83, 88, 97, 99, 111, 112, 114–117, 144, 164, 172

PST Pressure Sensor Tactiles. 90

PTT pulse transit time. 85

PVDF Polyvinylidene Fluoride. 18, 20, 21, 38, 44, 88

PZT Lead Zirconate Titanate. 18, 20

QKF quadratic kernel function. 64–66

QP quadratic programming. 64–66

QTC Quantum Tunnel Composites. 13

RBF radial basis function. 64–67

RBFKF radial basis function kernel function. 64

RF Radio Frequency. 86

RGB red, green, blue. 6, 87

ROS Robot Operating System. 91

RR Respiratory Rate. v, vii, x, 2–6, 83–90, 92, 96–99, 105, 110, 111, 113, 116, 117, 120–122, 130–132, 134–137, 139–142, 144, 164, 167–171

SIFT Scale Invariant Feature Transform. 35

SMO sequential minimal optimization. 64–66

SOM Self Organising Maps. 42

SPA Smart Phone Application. 108, 109, 164

SPI Serial Peripheral Interface. 57

SPL spline. 94, 95

SPO2 blood oxygen saturation degree. 120

STCW Stepped Frequency Continuous Wave. 86

SV stroke volume. 85

SVD singular value decomposition. 59, 60

SVM Support Vector Machine. ii, iii, v, vi, 21, 27, 29, 30, 38–42, 44, 46, 48, 49, 53, 63, 65–68, 70–74, 77, 79–81, 130, 139

SVR Support Vector Regression. 47, 49

TAC thermal flow. v, vi, 24, 25, 55, 58–61, 89, 91, 92, 96, 100, 103–107, 110–113, 167, 170, 171, 174

TBI Traumatic brain injury. 134

TDC static temperature. 24, 25, 55, 58–61, 89, 91

TH thumb. 39, 90, 91

TVL Television Lines. 120–122, 142

USB Universal Serial Bus. 57, 121

UU Ulster University. 90

VGA Video Graphics Array. 86

WMAC Weakly-Paired Maximum Covariance Analysis. 42

CHAPTER

ONE

Introduction

Humans perceive a sense of touch from all over their bodies. This sense can be broken down into "sub-senses" such as sensing temperature, contact and pain. These signals and internal sensations are transported to the somatosensory cortex through our spinal cord. It is here that a lot of the pre-processing is done before the manipulated data are sent to the neocortex for final sensory analysis and fusion with other senses. The level of accuracy that we can get from our finger tips and direct contact between our fingers and an object, and being able to sense environment conditions from this contact, is largely founded on the tactile and force sensing capabilities of our hands. Infants, in particular, rely heavily on their sophisticated tactile perception, gathering tactile information from their fingers and mouth as they are relatively slow to develop their visual acuity (Gibson, 1988). Furthermore, adults who are blind from birth develop sophisticated representations of objects and their dexterity by manipulating and characterising them (Marks, 1988; Smitsman and Schellingerhout, 2000). (Rothwell et al., 1982) studied the performance of a participant who was medically diagnosed as deafferented from his elbows to his hands, i.e. he was incapable of feeling cutaneous or proprioceptive touch in this area. Although the participant could assert force with his fingertips and retained exceptional performance in a wide range of grasping tasks, the inability to feel meant that he was incapable of performing the simplest fine motor skills such as writing with a pen, buttoning his shirt or holding a cup. (Johansson and Westling, 1984) evaluate the roles of skin receptors and sensorimotor memory and show that people become clumsy when deprived of reliable tactile information through numbness of anaesthetised or cold fingers. Anyone who has ever experienced having fingers so cold that they were numb can appreciate how the lack of sense of touch can make humans appear clumsy and lack control even in the simplest of grasping tasks. Similar limitations are evident in robotic systems without

tactile sensing (Fishel, 2012). Equipping robotic systems with technology that enables them to measure modalities such as temperature, microvibrations and force and coupling this with effective algorithms to analyse the data collected and form meaningful information about the person or material with which the robot is in contact would provide robotic systems with similar tactile sensitivity and perception that humans rely on to interact with the world.

Although vision has received the majority of attention in robot sensing research, a sense of touch is vital for many tasks, as dexterous manipulation requires control of forces and motions which can only be accomplished through touch (Howe, 1994). In order to produce the tactual perceptions required to learn about object properties, humans perform various types of movements when interacting with an object. Experimental psychologists have identified six general types of exploratory movements: pressure to determine hardness, static contact to determine thermal properties, lateral sliding movements to determine surface texture, enclosure to determine global shape and volume, lifting to determine weight, and contour following to determine exact shape (Lederman and Klatzky, 1987). Any individual action, or combination of these actions, enables a human to collect tactile information which allows them to identify objects and sense micro-vibrations or changes in an environment. Retrieval of this tactile information enables humans to perform delicate tasks using their sense of touch alone, such as reading an individual's vital signs.

Unfortunately, over many years of research, artificial tactile sensing technology has not developed as well as other perception modalities, even though tactile sensory information is vital for effective and informative interaction with environments (Dahiya and Valle, 2013). However, recent developments in tactile sensing technology, in particular the release of a biomimetic finger shaped tactile sensor produced by Syntouch® called the BioTAC^{TM} (Syntouch, 2013) have enabled rapid progress. This sensor allows for the collection of tactile data similar to that of humans, in particular micro-vibrations, thermal data and force data and is the sensor used in the research reported in this work.

Indicators of one's health such as pulse rate in Beats Per Minute (BPM) and Respiratory Rate (RR) can be sensed by touch; a further indicator, namely Capillary Refill Time (CRT) can be assessed using a combination of tactile-based control and vision-based sensing. These are inherent skills for a human due to their sophisticated tactile sensing. However, enabling a robot to complete similarly delicate tasks requires a sophisticated tactile sensor. The aim of this thesis is to develop algorithms capable of measuring vital signs in humans

that could equip a First Responder Robot to triage victims in an emergency scenario or following a natural or man-made disaster. Assessing the vital signs of humans is required to perform an initial evaluation of a victim's current health and hence enable a triage system to be applied in order to prioritise which victims need the most urgent attention. Over the past three decades Information and Communications Technology (ICT) for use in the health-care field has become heavily researched (Ferrigno et al., 2011). Methods in which systems are used to assess a human's current health status, particularly in emergency scenarios, are related to the novel approaches outlined in this thesis. Many methods include wearable sensors or communicating with a trapped person to attempt to assess their health status. However, wearable sensors are not typically found on humans in an emergency scenario and methods to physically assess a human's health status are lacking. Furthermore, it is clear that tactile sensing approaches to human vital sign assessment in robotics are lacking in the literature. Tactile and vision based sensing methods that enable the use of a non-invasive sensor, which is not required to be worn, to accurately measure human vital signs are required for use in disaster zones.

The work in this thesis aims to develop algorithms for effective material identification in order to ascertain the capability of the BioTAC tactile fingertip. Subsequently, this thesis aims to develop algorithms that enable the BioTAC tactile fingertip sensor to measure BPM from the radial artery of a human's wrist, the RR by making contact with a human's chest wall regardless of clothing covering the chest and an accurate measure of CRT by pressing into a human's forehead. This information is used to develop a fuzzy logic classifier for use in triage of victims following an emergency or disaster. Research into using robots as automated triage systems in disaster zones is still quite limited and is focussed on the systems or architectures towards an eventual physical system. The algorithms presented in this thesis could be a significant contribution toward the development of such systems.

1.1 Thesis Contributions

This thesis presents a substantial body of research into the use of tactile sensing for robotic systems. This chapter provides an introduction to the thesis. Chapter 2 provides an overview of tactile sensing and Chapter 3 provides an overview of computational intelligence in tactile sensing. A tactile sensing based algorithm capable of identifying materials from touch alone is presented

in Chapter 4. This is achieved by using a BioTAC^{TM} biomimetic finger-shaped tactile sensor from Syntouch® (Syntouch, 2013) to execute standard exploratory actions on the surface of a material. Numerous machine learning classifiers and hybrid combinations of the classifiers are implemented and evaluated for classifying materials based on their thermal conductivity and surface texture. The best performing machine learning approach is further evaluated against human performance when faced with the same task. All aspects of this research have been published in: (Kerr et al., 2013, 2014a,b) and a journal paper is currently under review in the Elsevier Journal of Expert Systems with Applications (Kerr et al., 2017). The objective of the material classification work, which is presented in Chapter 4, is to ascertain the sensitivity and accuracy of the BioTAC sensors for their suitability for measuring human vital signs.

Novel methods for measurement of key human vital signs such as BPM and RR using a robotic system comprised of the five fingered Shadow Hand with three BioTAC sensors are presented in Chapter 5. The BPM and RR of twelve healthy human participants are measured. The data collected are smoothed to enable the identification of troughs and peaks which are used to calculate the BPM and RR of the participants. The methods presented in Chapter 5 are capable of determining whether a person has a slow heart rate (< 60 BPM), i.e. bradycardic, a normal heart rate ($60 - 100$ BPM) or a fast heart rate (> 100 BPM), i.e. tachycardic. Also, it is possible to determine if a person has a slow, normal or fast breathing rate (RR). The methods presented are evaluated against readings measured by a medical professional on the same participants. The methods presented in this thesis aim to mimic the procedure carried out by medical professionals. The methods for determining BPM have been published in a conference paper (Kerr et al., 2015).

The skin is one of the first organs that the human body temporarily stops supplying with blood, in a state of shock or emergency, in order to allow more blood to travel to vital organs such as the kidneys and liver. Therefore, the measurement of a third vital sign, CRT, is made possible by the methods presented in Chapter 6. Vision is required for the measurement of CRT; therefore, a camera mount was specifically designed for the BioTAC fingertip sensors. The algorithms presented in Chapter 6 are used to determine the time taken for blood to return to the pressed area of the forehead. The force at which the fingertip presses against the participant's forehead is regulated and a novel method for determining the change in colour from vision-based data is presented. This replicates the procedure carried out by medical professionals when

measuring CRT.

A fuzzy based classification algorithm is also presented in Chapter 6 in order to collate the three vital signs measured from the participants and determine an overall indication of their current health status. The fuzzy system is trained and tested with synthetic data and further validated by applying the real data collected from human participants. The algorithms presented, together with the fuzzy classification system would equip a robot with the necessary skills to perform as a triage system in a disaster zone or emergency scenario.

The main contributions presented in this thesis are:

- A new method for tactile sensing-based material classification, capable of outperforming human performance.
- Evaluation of numerous classification algorithms and novel combinations of classification algorithms for material classification.
- Measurement and analysis of human BPM and heart beat rhythm via robotic tactile sensing.
- Measurement and analysis of human RR and breathing rhythm via robotic tactile sensing.
- Measurement and analysis of human CRT via complementary use of robotic tactile sensing-based control and a High Definition (HD) camera.
- Development of a fuzzy based classification system to ascertain an overall status of health.

1.2 Thesis Outline

The thesis is organised as follows:

Chapter 2 outlines an overview of human tactile sensing, highlighting its sophistication and high ability, emphasising why it is so difficult to replicate with an artificial system. This chapter also provides a review of tactile sensing technologies available to date. Finally, a detailed introduction to the BioTAC sensor is provided, this is the sensor used for data collection in this thesis.

In Chapter 3 an overview of computational intelligence methods used with tactile data is presented. Applications of these methods are discussed including

tactile sensing based material identification and machine learning applications that have used the BioTAC sensor.

Chapter 4 presents a machine learning approach to material identification using only tactile sensing. An evaluation of machine learning classifiers and hybrid combinations of classifiers is also outlined in this chapter to ascertain the most effective approach. The algorithm performance for the identification of materials from tactile data is evaluated against human performance for the same experiment. It is shown that the learning algorithms can outperform humans when identifying materials by analysing tactile data such as thermal conductivity and vibration representing surface texture.

In Chapter 5 a review of methods from the literature for the measurement of human vital signs is presented. Novel methods for measuring and analysing a human's pulse and RR are also presented. Pulse and breathing data are collected from 12 human volunteers. Algorithms for smoothing the collected data and identifying heart beats and breaths from the data are presented. The performance of the artificial system is evaluated against a medical professional and found to achieve similar accuracies.

Chapter 6 provides a review of robotic systems used to assist humans in disaster zones. A novel method for accurately determining a human's CRT using a robot hand, biomimetic tactile sensor and a red, green, blue (RGB) camera is presented. As a medical professional can only estimate that a person's CRT is below the threshold of 2 seconds; the method presented in this chapter provides a more accurate measurement of CRT than the current standard method carried out by medical professionals. A fuzzy classification algorithm that combines the measured BPM, RR and CRT and determines an overall status of health is presented. These algorithms combined with the fuzzy classifier can be used to equip a robot with the necessary techniques required to enable a robot to perform medical triage in a disaster or emergency scenario.

Chapter 7 presents a conclusion to the thesis, outlines the contributions made by this research and provides an outline of future work.

CHAPTER

TWO

Tactile Sensors

2.1 Introduction

Humans can grasp objects of varying shapes and sizes (sometimes without ever having previously seen the object) and ascertain properties such as surface texture, compressibility and thermal characteristics. They can perform highly complex tasks and switch between grasps in response to changing task requirements. This is due in part to the physical structure of our hands (multiple fingers with many degrees of freedom), and in part to our sophisticated control capabilities (Howe, 1994).

In contrast, efficient and accurate designs of robotic hands and touch sensors are only now appearing following a few decades of development (Tiwana et al., 2012). Surface texture, compressibility and thermal characteristics can now be determined by the use of artificial tactile sensing systems, albeit with limited performance. As Lee and Nicholls (1999b) indicated in their survey of tactile sensing, the design and build of tactile sensors started in the 1980s, which means most research into artificial tactile sensing was delayed somewhat until after this. It was from 1991 onwards that there was a significant increase in tactile sensing research. Therefore, industrial applications have mainly evolved to rely on technology which has machine vision as the core component, with limited contributions from tactile sensing. This was due to the lack of commercially available tactile sensors for robotic fingers and grippers (Fishel, 2012).

This chapter provides an overview of tactile sensing. Initially a brief description of the human tactile sensing system is presented in Section 2.2. An overview of artificial tactile sensing technologies is then provided in Section 2.3, followed by a detailed description of the BioTAC^{TM} biomimetic finger-shaped tactile sensor from Syntouch® (Syntouch, 2013) in Section 2.4; this is the tactile sensor used

for all of the experiments presented in this thesis.

2.2 Human Tactile Sensing

The human skin is an extremely complex and efficient organ on the body and it is one of the main sources of tactile information together with muscles, joints and tendons. Two main sensory systems have been distinguished in relation to the human sense of touch: kinaesthetic and cutaneous (Dahiya and Valle, 2008). Loomis and Lederman (1986) state that the kinaesthetic system provides information regarding body posture from sensory inputs from receptors within the muscles, joints and tendons. Receptors in the kinaesthetic system include muscle spindles, which respond to changes in muscle length and tendon organs, which provide information on muscle tension (Clark and Horch, 1986). Furthermore, Howe (1994) states that during movement the deformation of skin around joints may provide extra information about the angle of the joint, particularly in the fingers.

The cutaneous system provides information on the stimulation of the outer surface of the skin by means of receptors located within the skin and the associated somatosensory area of the Central Nervous System (CNS) (Lucarotti et al., 2013). The cutaneous system deals with spatiotemporal perception of external stimuli through a large number of receptors including mechanoreceptors for detecting vibration/pressure, thermoreceptors for measuring temperature, and nocioceptors for recognising pain/damage (Johansson and Westling, 1984). These receptors are distributed all over the body with variable density (Dahiya et al., 2010). A small sensory receptor in the subcutaneous tissues is the Pacinian corpuscle, capable of detecting vibrations of frequencies up to 1000Hz; this plays a vital role in the cutaneous sensing of microvibrations in human fingertips which are critical for tool usage, involving the perception of microtextures and reflexive grip control (Fishel, 2012).

The response to mechanical stimulus is mediated by mechanoreceptors that are embedded in the skin at different depths. Their number per square centimetre area is estimated to be 241 in the fingertips and 58 in the palm of adult humans (Johansson and Vallbo, 1979). Figure 2.1 shows a cross-section of human glabrous skin. The tissue includes four kinds of mechanroceptors with each kind located at a specific level: fast adapting nerve endings with small receptive fields, fast adapting nerve endings with large receptive fields, slowly adapting

nerve endings with small receptive fields and slowly adapting nerve endings with large receptive fields. Fast adapting nerve endings produce little response to static loading but strong responses to dynamic loading and slowly adapting nerve endings demonstrate little response to high-frequency stimuli but produce sustained response to static stimuli (Howe, 1994), (Fishel, 2012). On the grasping surfaces of the hand there are approximately 17,000 mechanroceptors (Howe, 1994), with the shallowest and deepest being the Meissner corpuscle and Pacini corpuscle which lie below the surface at approximately 0.7mm and 2mm respectively (Asamura et al., 1998).

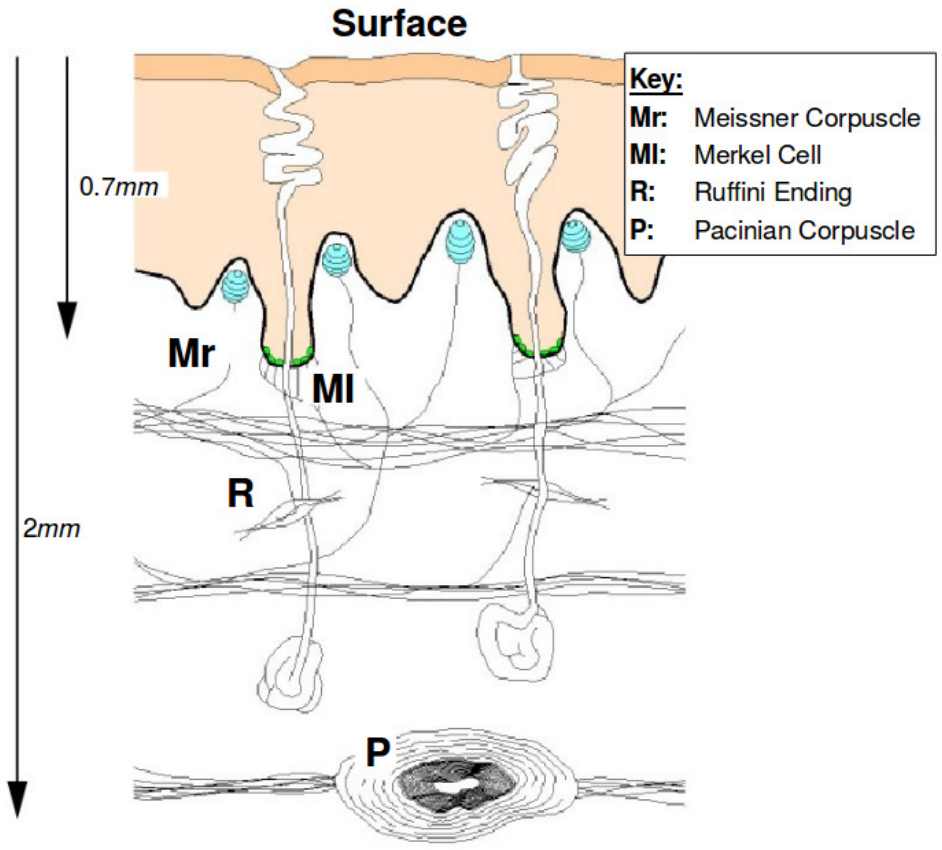

Figure 2.1: Cross-section of Human Glabrous Skin (Asamura et al., 1998)

The hairless glabrous skin on the palm of the hand possesses different receptors and characteristics to hairy skin found elsewhere on the body (Fishel, 2012). For example, to enable humans to conform to the wide range of objects encountered on a daily basis, the glabrous skin in the palm and fingertips is thicker and more compliant than hairy skin (Fishel, 2012). Furthermore, Vallbo and Johansson (1978) describe that there is a higher density of mechanoreceptors in glabrous skin particularly at the fingertips. Papillary ridges, or fingerprints, unique to glabrous skin have been hypothesised to assist with the transduction of vibra-

tions (Loeb and Fishel, 2009), (Scheibert et al., 2009). Rather than perceiving each small surface feature individually, humans perceive a surface as textured if the features are less than approximately 1mm apart (Howe, 1994). Furthermore, the minimum perceivable height of a static raised feature on a smooth surface was found to be 0.85 microns (Johansson and Westling, 1984).

According to Loomis and Lederman (1986), tactual perception, where both the kinaesthetic and the cutaneous systems supply significant information about events and distal joints, is referred to as haptic perception. Analogous with the kinaesthetic and the cutaneous systems in humans, robotic systems could be equipped with extrinsic/external and intrinsic/internal sensors respectively, for example force sensing at the servo or motor of the joint. (Wettels et al., 2014) emphasise that extrinsic tactile sensors provide considerably more precise, multi-modal information about object or material properties through interaction than intrinsic tactile sensors. Retrieving similar precise information through interaction requires a sophisticated tactile sensor, one which mimics the sensing capabilities of human skin, at least to some extent. The most advanced tactile sensor available that is capable of collecting similar data is the sensor used for all of the experiments in this thesis, the BioTAC sensor from Syntouch.

2.3 Tactile Sensing Technology

Stand alone tactile sensors or those fitted to robotic hands or grippers have received considerable attention over the last few decades and some excellent designs and proposals have been presented, e.g. (Shimojo et al., 2010). The literature outlines that in general a robotic tactile system should be cost effective and have the following characteristics (Dario and De Rossi, 1985; Howe, 1994; Dahiyal et al., 2007; Dahiya and Valle, 2008):

- There should be a small number of tactels, in order to minimise the processing time of tactile images, typically estimated as 25-256 elements. A tactel (derived from a combination of *tac*tile *el*ement) is a single sensing point on a tactile sensor array. It is also known as a taxel (derived from *ta*ctile pi*xel*) modelled on a pixel,
- Spatial sensitivity similar to that of humans, i.e. 1mm distance between the centres of neighbouring tactels,
- Sensitivity to forces in the range of 1gram-force (gmf) (0.01Newton (N))

to 1000gmf (10N) with incremental force resolution of 1gm,

- Negligible hysteresis and reasonable response linearity,
- Capability to measure characteristics such as compressibility, temperature etc. (Dahiya and Valle, 2008).

There have been various tactile sensors and sensing arrays presented in the literature with or without the aforementioned characteristics. Tactile sensors have utilised a range of transduction principles such as resistive sensors, capacitive sensors etc. to measure tactile data. Figure 2.2 shows an outline of the types of tactile sensors and some of their advantages and disadvantages. The sensor types are summarised in the sections outlined in the diagram.

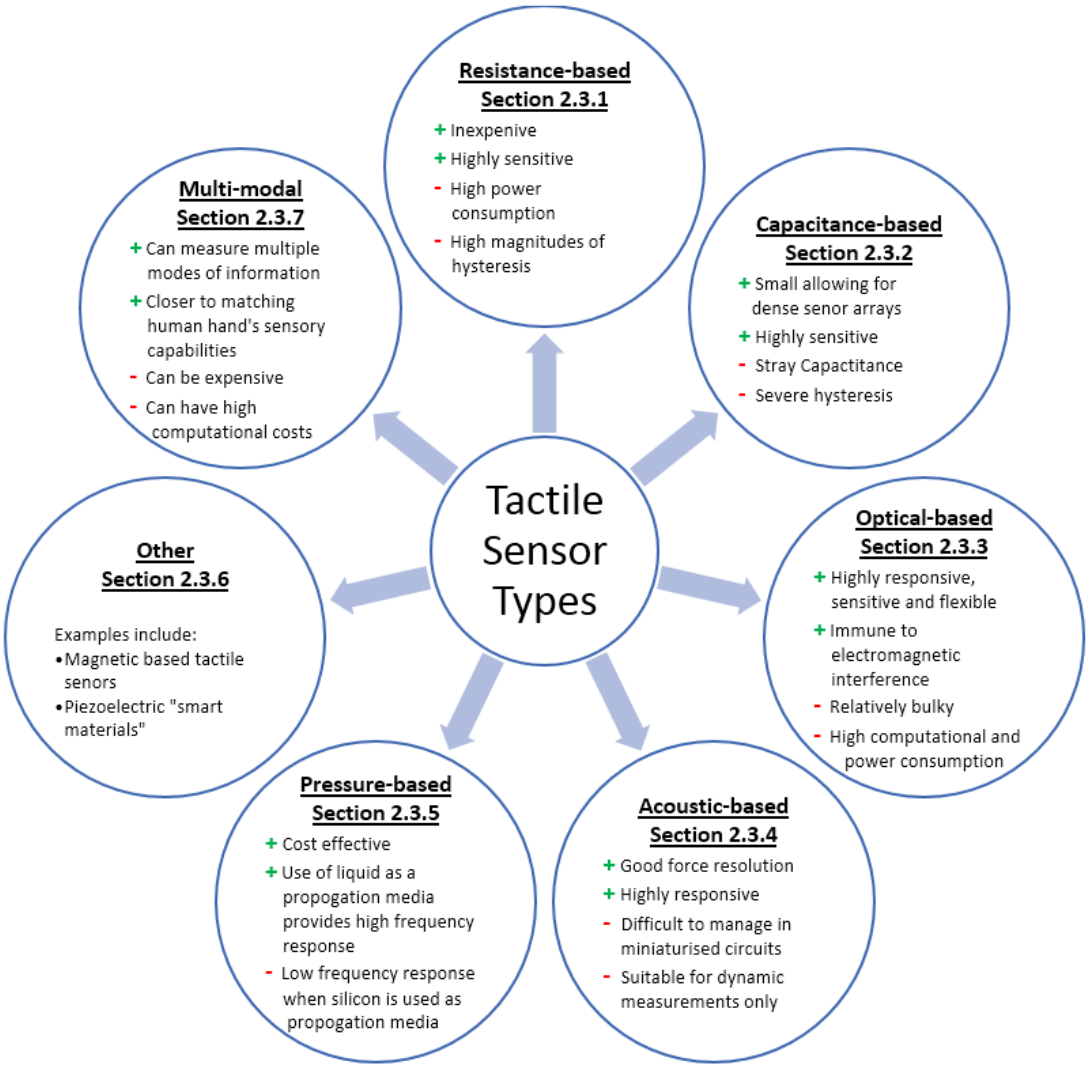

Figure 2.2: Diagram outlining various types of tactile sensors and their advantages and disadvantages

2.3.1 Resistance-based Tactile Sensors

In a resistive sensor, the resistance across the sensor changes according to a change in the sensors' environment. In terms of resistive tactile sensors, they usually consist of two conductive sheets separated by air or insulating fabric. A voltage gradient is generated on one of the sheets by applying a reference voltage to one end of the sheet and ground to the other end. The second sheet acts like the slider in a linear potentiometer when brought into contact with the first sheet by an applied force, enabling detection of contact and the location of the contact point to be calculated. Although the sensors are generally inexpensive and sensitive, they are expensive in terms of power consumption and are limited to measurement of only one contact location. Zhang and So (2002) presented an improved design of a resistive tactile sensor which involves arranging the sensors in an array therefore enabling measurement of many contact points.

Piezoresistive touch sensors are made from materials whose resistance changes when force or pressure is applied to them and have been proposed for use in anthropomorphic hands (Weiss and Worn, 2004). Generally the resistive materials are an elastomer, a conductive rubber or conductive ink which is pressure sensitive (Tiwana et al., 2012). This type of sensor is particularly popular in Micro Electro Mechanical Systems (MEMS) and silicon based tactile sensors (Wolffenbuttel and Regtien, 1991; Beebe et al., 1995). A lot of position sensing devices such as joysticks use Force Sensing Resistors (FSRs) which are based on piezoresistive sensing technology. There are numerous FSRs commercially available from Tekscan (2017) and Weiss Robotics (2017) that use carbon enriched silicon rubber in their rigid tactile sensors. Eeonyx (2017) supply a piezoresistive fabric and Inaba Rubber (2017) manufacture a pressure conductive rubber for use in research and industrial applications for example detecting the position of objects and slip detection. Another commercially available sensor based on piezoresistive technology is the Nano17 sensor produced by ATi industrial Automation (ATi, 2017) shown in Figure 2.3 and this sensor is used throughout the work presented in this thesis to calibrate and verify force applied to various surfaces throughout the experimental work. Although FSR sensors are low cost with good sensitivity, they provide high non-linear responses and can suffer from high magnitudes of hysteresis (Vidal-Verdú et al., 2011). Furthermore, an elastic material may never regain its initial form following multiple deformations and as a result piezoresistors suffer from lower repeatability than some other forms of tactile sensors (Kappassov et al., 2015).

Figure 2.3: Image of ATi Nano17 force Sensor (ATi, 2017)

Quantum Tunnel Composites (QTC) sensors (known as tunnel effect tactile sensors) are capable of transforming from near perfect insulators to a metal like conductor when deformed by stretching, twisting or compressing the material. The resistance drops exponentially throughout the transition from insulator to conductor, following a smooth and repeatable curve. The metal particles within the QTC get so close to each other that quantum tunnelling of electrons takes place between the particles but they never actually come in contact with each other (Dahiya and Valle, 2008). Walker (2004) used QTC tactile sensors in earlier versions of the Shadow Hand. Zhang et al. (2013) also use their own developed flexible QTC tactile sensor in an anthropomorphic artificial hand. Kappassov et al. (2015) state that QTC sensors are more technologically advanced than capacitive or piezoresistive sensors and Maheshwari and Saraf (2006) present a sensor based on the electronic tunnelling principle with a spatial resolution of $\approx 40\,\mu m$, which is better than that of a human fingertip.

2.3.2 Capacitance-based Tactile Sensors

A common form of tactile sensors is capacitive sensors (Almassri et al., 2015; Prescott et al., 2015). They consist of a dialectric material sandwiched between two conductive plates (Lucarotti et al., 2013). Schmidt et al. (2006) present examples of capacitive touch sensors which consist of a plate capacitor in which the relative position of the plates are shifted when force is applied changing the distance (d) between the plates or the effective area, as demonstrated in Figure 2.4(a). The plates are separated by a compressible dielectric material as demonstrated in Figure 2.4(b). The distance between the plates reduces when force is applied which in turn changes the capacitance. Capacitive sensors are a very common form of sensing transducers and used by some robot manufactures. For example, as presented by Schmitz et al. (2011) they are used in the iCub humanoid robot for sensing capabilities in the palm (Figure 2.4(c)) and

they were used by Willow Garage as tactile sensors in the grippers of the PR2 robot as seen in Figure 2.4(d) (Romano et al., 2011).

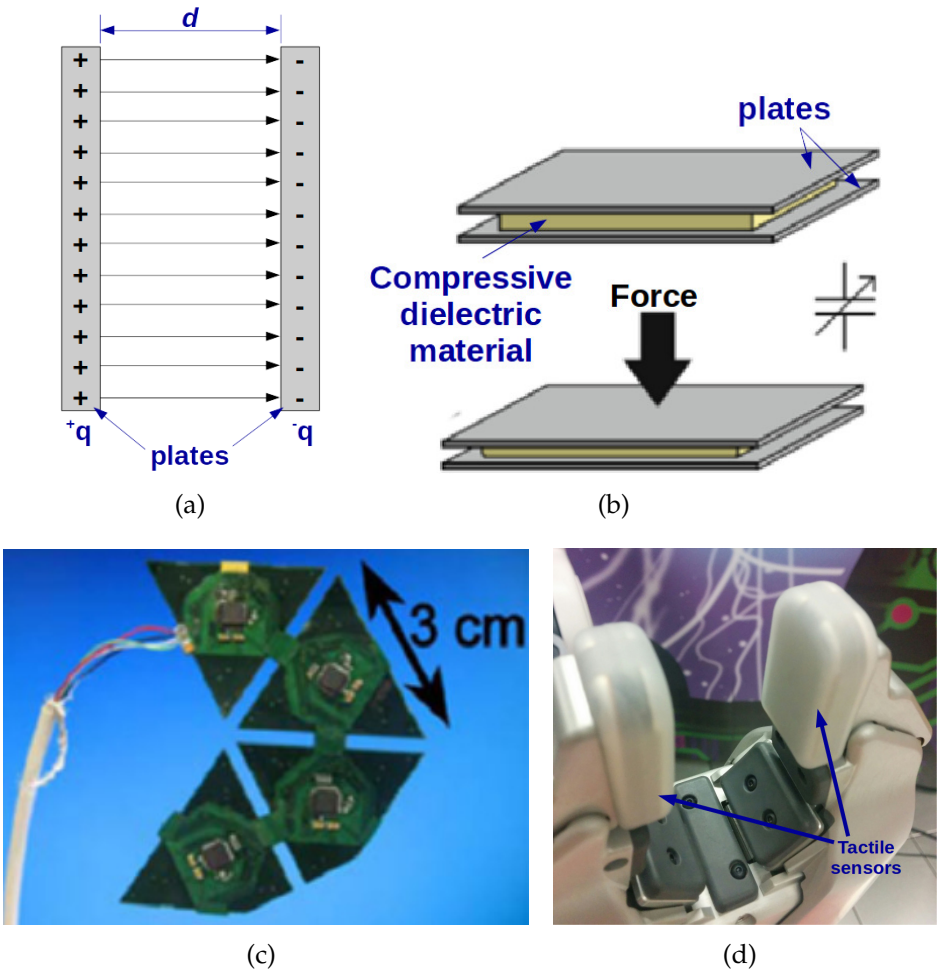

Figure 2.4: a) Sketch demonstrating that the capacitance of a parallel plate capacitor depends on the area of the plates and the distance between the plates, d.(Fraden, 2003); b) Sketch showing the two conductive plates separated by a dielectric material (Balasubramanian and Santos, 2014); c) A mesh of the triangular capacitive sensors from the palm of the iCub robot (Schmitz et al., 2011); d) Image showing the tactile sensors in the gripper of the PR2 robot at the Intelligent Systems Research Centre (ISRC).

Capacitive touch sensors also allow for the production of dense sensor arrays as they can be produced to be very small in size. Bhattacharjee et al. (2012) present a method using capacitive touch sensors consisting of a 24×24 array of relatively large tactels measuring $9 \times 9mm$. The large tactile array sensor covers the forearm of the Meka A1 robot and the authors classify objects with which the arm comes in contact, into four categories: rigid-fixed, rigid-moveable, soft-fixed and soft-moveable. Gray and Fearing (1996) present an 8×8 capacitive tactile sensing array of $1mm^2$ area and a spatial resolution at least 10 times

better than the human limit of $1mm$. Due to their sensitivity and resolution capacitive sensors are the basis of many touch screen technologies (Dahiya et al., 2010). However, although capacitive sensors can be very sensitive, severe hysteresis and stray capacitance are major drawbacks (Dahiya and Valle, 2008).

2.3.3 Optical-based Tactile Sensors

Most optical based tactile sensors use the properties of optical reflection between mediums of different refractive indices (Lee et al., 2013). They consist of a light source, a clear plate and a compliant membrane stretched above, but not in contact with, the clear plate. Light is directed along the edge of the plate. When there is no force applied, the light passes via total internal reflection and when there is force applied it suffers through diffuse reflection. Placing charge-coupled device (CCD) or complementary metal-oxide semiconductor (CMOS) cameras in the imaging area allows for the light leaving the plate to be recorded and the intensity of the light is proportional to the magnitude of force between the plate and the object (Dahiya and Valle, 2008). An optical three-axis tactile sensor also sensitive to shear forces was developed by Yussof et al. (2009) for use on the fingertips of a two-fingered hand. The sensor consists of a CCD camera, a light source, an optical fibre-scope and 41 sensing elements made from silicon rubber; the use of the sensor enables the hand to manipulate a light paper box. Kampmann and Kirchner (2014) present a three-fingered robot gripper with embedded fibre optic sensors combined with the use of both piezoelectric sensors to measure dynamic forces and strain gauge sensors to measure absolute forces in their multi-modal sensing system to measure force distribution. Schunk (2017) released a commercially available SDH multi-jointed 3-finger gripper (shown in Figure 2.5(a)). The hand has the option of having optical-based tactile array sensors fitted to the end of the grippers (shown in Figure 2.5(b)) to allow for basic force readings to be calculated when in contact with objects.

A flat 3×3 optical tactile sensor array was developed by Xie et al. (2014) where elements of the sensor were magnetic resonance compatible so that they could be used in Magnetic Resonance Imaging. Heo et al. (2006) present an optical fibre based tactile sensor with spatial resolution of $5mm$ capable of measuring forces as low as 0.001N. Although these sensors are highly responsive, sensitive, flexible and immune to electromagnetic interference they are relatively bulky, can suffer from signal distortion due to loss of light caused by micro bending

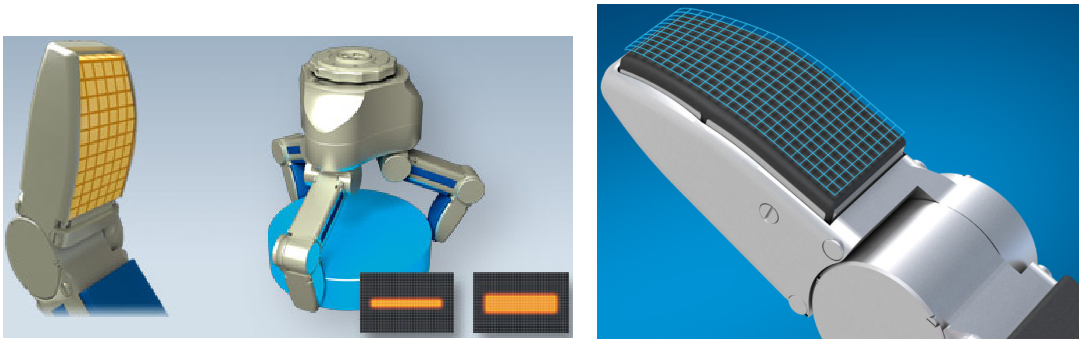

(a) (b)

Figure 2.5: a) Image showing the Schunk SDH multi-jointed 3-finger gripper grasping an object.(Schunk, 2017); b) Sketch illustrating the optical-based tactile array sensor (Schunk, 2017)

(Liu et al., 2017) and are known to have high computational costs and power consumption (Dahiya and Valle, 2013; Tiwana et al., 2012).

The "TACTIP" biologically inspired biomimetic sensor was developed by Bristol Robotics Laboratory (BRL) (Chorley et al., 2009). Papillae pins are located on the inside of the sensor skin and deformation caused by interacting with objects is measured optically by tracking the movement of the papillae pins, which represent the intermediate epidermal ridges of human skin. The original TACTIP sensor was 40mm in diameter, a schematic of the original TACTIP fingertip can be seen in Figure 2.6(a). The TACTIP sensor was later revised and reduced in size to 20mm to further replicate a human fingertip and be suitable for use on a robotic hand (Winstone et al., 2012). A schematic of the revised fingertip can be seen in Figure 2.6(b).

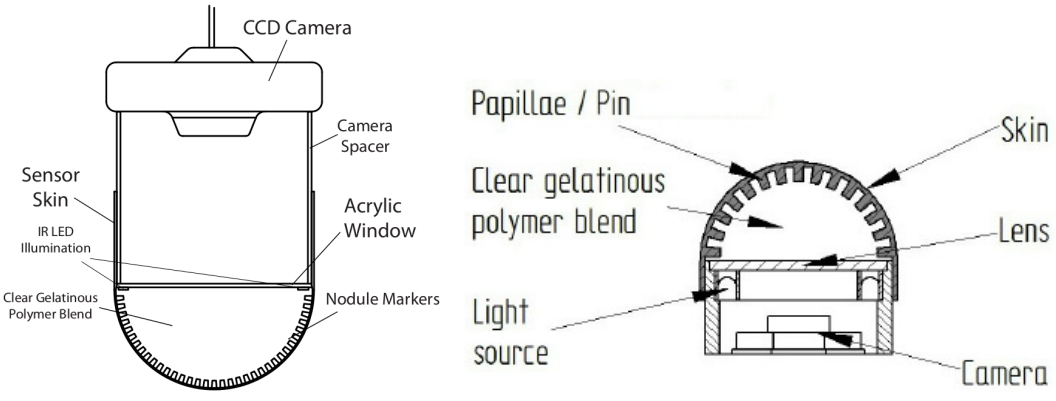

(a) (b)

Figure 2.6: a) Image showing a schematic of the original TACTIP sensor (Chorley et al., 2009); b) Image showing a schematic of the revised TACTIP sensor (Winstone et al., 2012).

Roke et al. (2012) used the TACTIP as part of a mechanical teleoperated device to detect and localise embedded objects in a synthetic skin material, representing lumps in teleoperated surgery. Test participants palpated a number of artificial tissue models in order to identify lumps a varying stiffness. It was shown that the addition of a tactile feedback system in the form of the TACTIP sensor decreased the time users spent locating the lump from an average of 37 seconds in comparison to 55 seconds when using a mechanical device without tactile feedback for the same task. Furthermore, the addition of tactile feedback improved the accuracy of lump detection from 64% to 98% and reduced the localisation error from 18mm to 11mm. Based on the premise that the human finger is known to be highly sensitive to lateral skin deformation, Roke et al. (2013) evaluated the effects of retrieving lateral information together with tactile feedback from the mechanical teleoperated device from the authors previous work (Roke et al., 2012). Surprisingly, it was proven that no improvement was gained in the participants' ability to detect and localise lumps in the form of embedded objects by adding lateral feedback (Roke et al., 2013). The sensor has since been developed as a 3D printed sensor and the designs are available to the tactile sensing research community as open-source designs (BRL, 2016). However, the sensor was not released until after the majority of the experimental work in this thesis was completed.

2.3.4 Acoustic-based Tactile Sensors

Acoustic ultrasonic sensing technology has been used for tactile sensing by using microphones to detect surface noise caused during slip or motion. Milighetti et al. (2006) present a sensor that detects contact events from their ultrasonic emission at a point of contact. The device consists of a Polyvinylidene Fluoride (PVDF) polymer in a 2×2 array of receivers on a silicone rubber sensing dome capable of localising the point of contact; it is stated to be very effective in identifying surface roughness during movement and detecting slip. Ultrasonic tactile sensors have also been used to measure the hardness/ softness of a material as presented by (Omata et al., 2004). This is achieved by measuring the change in resonance frequency of Lead Zirconate Titanate (PZT) in accordance with an object's acoustic impedance. Although acoustic tactile sensors have good force resolution and are very responsive, material such as PZT is difficult to manage in miniaturised circuits (Alonso-Martín et al., 2017).

Structure-borne sound signals can be utilised for tactile sensors. Möser (2009)

states that "structure-borne sound" is the term used for vibrations and waves in solid structures. Structure-borne sounds occur at initial contact with an object or during slippage in manipulation tasks and can serve as indicators to inform the manipulator of details about the placement of the object in pick-and-place tasks. Microphones and accelerometers can be used as detecting devices for structure-borne sounds (Kappassov et al., 2015). Romano et al. (2011) use a highly sensitive 3-axis accelerometer in their approach for example in the base of the PR2 robot gripper, shown in Figure 2.7. The sensor is used to detect when contact is made between the object and a table which determines when to release the object. Although these types of sensors have a wide bandwidth, they are suitable for dynamic measurements only.

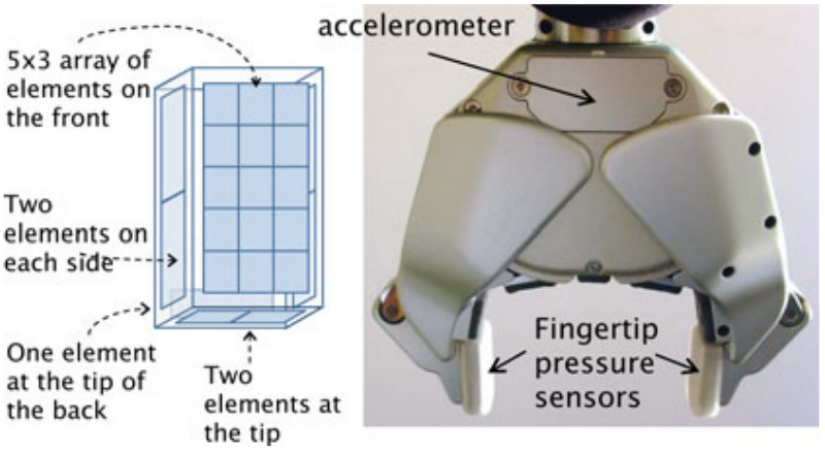

Figure 2.7: Image of the PR2 Tactile Sensors with the accelerometer rigidly mounted to a printed circuit board in the palm (Romano et al., 2011)

2.3.5 Pressure-based Tactile Sensors Types

Barometric measurement-based tactile sensors use pressure transducers to measure the pressure in air and liquids (Fraden, 2003). Deformability of a sensor together with a high frequency response can be achieved by using liquid inside the sensor where changes in pressure values are a representation of vibration (Fishel, 2012). A sensing system which incorporates the use of electro-conductive fluid to produce both dynamic and constant vibration signals is presented by (Wettels et al., 2014). The exterior surface of the sensor is textured similar to that of the human fingerprint. Therefore, any motion over the textured surface or slippage of the surface against another causes micro-vibrations, which propagate as sound waves through the liquid medium to a pressure transducer (Fishel et al., 2008). With a bandwidth of 1kHz, the sensor

is suitable for slip detection applications by analysing the vibration signals. This type of sensor is embedded in the BioTAC^{TM} biomimetic finger-shaped tactile sensor from Syntouch® (Syntouch, 2013) shown in Figure 2.8, which is discussed in more detail in Section 2.4.

Figure 2.8: Photo of the BioTAC Biomimetic fingertip (Syntouch, 2013)

As an alternative to using liquid as a medium for sound waves to travel and represent vibration, Tenzer et al. (2014) present a sensor with a barometer fitted in each tactel moulded within a silicon rubber which acts as a membrane. When the sensor makes contact with an object within the environment the rubber is deformed causing changes in the pressure values in the barometer. It was found that although these sensors, with a barometer moulded into silicon rubber, are cost effective they also have a low frequency response due to the elasticity of the silicon rubber. However, Wettels et al. (2014) showed that sensors incorporating liquid and barometers have a high frequency response, therefore the use of liquid as a propagation media is more suitable than other media such as silicon rubber, in relation to frequency response.

2.3.6 Other Tactile Sensor Types

Nowlin (1991) presents techniques that use magnetic based tactile sensors which measure changes in the flux density of a small magnet when forces are applied to it. The measurement of flux density can be made by either a magneto resistive device or a Hall Effect as presented by Jamone et al. (2006). These types of sensor boast many advantages such as a linear response, no measurable mechanical hysteresis, robustness and high sensitivity and dynamic range. However, they involve complex computations and they cannot be used in a magnetic medium (Dahiya and Valle, 2008).

The piezoelectric effect is produced in quartz crystals (Kappassov et al., 2015) or in man-made piezoelectric materials. They are classed as 'Smart Materials' because they can be used as either sensors or actuators due to the fact that they generate charge/ voltage proportional to the applied force or, alternatively, they are able to generate force due to electrical output (Tiwana et al., 2012). A piezoelectric film with structural electrodes was used by Chuang et al. (2013) in the development of a flexible tactile sensor which was used to lift an object of unknown weight. Some ceramics such as PZT have good piezoelectric properties; however, it is polymers such as PVDF or its copolymers that are normally used for touch sensors such as those presented by Dargahi et al. (2000) and Yuji and Sonoda (2006). This is due to the attractive properties of PVDF polymers as they are chemically stable and flexible (Flanagan and Wing, 1993). One major concern with the use of piezoelectric materials as touch sensors is their sensitivity to temperature change (Lucarotti et al., 2013).

2.3.7 Multi-modal tactile sensors

Tactile sensors which use more than one method of transduction allow for the measurement of multiple modes of information such as vibration, force and thermal characteristics. Dahiya and Valle (2008) show that studies of human skin and tactile performance have inspired the development of such tactile sensors which generally utilise softer materials rather than solid or fairly rigid materials. Someya et al. (2004) present a number of touch sensors which use conductive rubber as a transducer by taking advantage of the impedance change due to the force applied. Furthermore, Johansson and Flanagan (2009) state that a robot should be equipped with a multi-modal tactile sensor if it is to be expected to match the human hand's sensory capabilities. Wade et al. (2015) present a hand-held multi-modal sensor consisting of a fabric-based tactile sensor for force estimation, a contact microphone and accelerometer to measure vibration and acceleration, a fast response thermistor for temperature sensing and a sensor for measuring heat transfer. The authors collected data from common objects found in a bathroom, used principal component analysis (PCA) to reduce data dimensionality and a Support Vector Machine (SVM) to complete binary classification between pairs of the objects, achieving up to 100% accuracy in some instances, for example classifying between a toothbrush and a countertop.

Some more recent tactile sensors have been constructed using a combination of

piezoelectric and piezoresistive materials and therefore have the ability to sense dynamic and static contact forces (Kappassov et al., 2015). Goger et al. (2009) present an example of such material consisting of piezoresistive rubber with PVDF which is integrated with an anthropomorphic fluidic hand (Schulz et al., 2004). Also, Choi et al. (2006) present a four-fingered robot hand which utilises a pressure variable resistor ink with PVDF as a sensing mechanism. Kawamura et al. (2013) present a hybrid sensing system consisting of a combination of static and dynamic transducers by combining a force tactile sensor and a carbon micro-coil touch sensor. Hasegawa et al. (2010) presented a method that enhanced autonomous grasping by integrating pressure and proximity sensors on an artificial fingertip. Friesen et al. (2015) analyse the mechanical properties of the human fingertip when pressed against a surface and present a biologically inspired artificial fingertip that resembles the behaviour of the human fingertip when pressed against the surface. The fingertip consists of a rigid aluminium core with a soft sponge surrounding it, a stiffer outer skin-like membrane and a very thin outer layer of textured acrylic paint to represent the stiff stratum corneum of the human fingertip (Friesen et al., 2015). Two types of rubber were evaluated for the skin-like membrane. It was found that the response of the fingertip to transient mechanical perturbation and the force-deformation characteristics of the fingertip were both in qualitative agreement with the human fingertip. Also the fingertip exhibits friction reduction when subjected to transverse ultrasonic vibrations through interactions with variable friction tactile displays (TPads). These fingertips contain no means of collecting force, vibration or temperature based data at this stage, however Friesen et al. (2015) provide an alternative method for constructing an artificial fingertip that is approximately the same shape and size of the BioTAC sensor and the human fingertip.

Lin et al. (2009) present the BioTAC biomimetic tactile sensor which is shaped like a human fingertip, as seen in Figure 2.8. This sensor is capable of measuring thermal, force and microvibration modalities simultaneously. Syntouch have also released an updated design of the BioTAC sensor, namely the BioTAC SP^{TM} which can be seen in Figure 2.9(a). The BioTAC SP has the same functionality as the original BioTAC sensor only it has a greater contact surface area. The electronics of both the BioTAC and BioTAC SP are protected inside the rigid core of the sensors therefore providing the aforementioned multiple sensory capabilities without placing any sensors directly onto the skin. Furthermore, Syntouch have recently released their NumaTac^{TM} Technology as seen in Figure 2.9(b). This sensor distils all the sensory capabilities of the BioTAC and

BioTAC SP and can be designed and manufactured to cover large and complex areas such as a torso, feet, hands, limbs etc., (Syntouch, 2013).

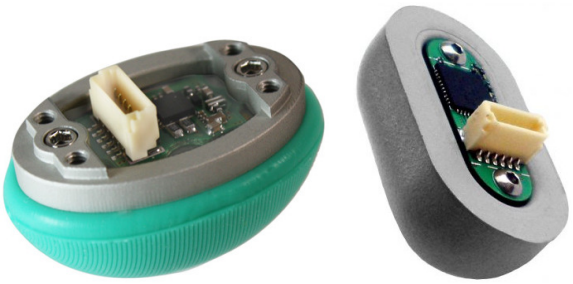

(a) (b)

Figure 2.9: a) Photo of the BioTAC SP Biomimetic fingertip (Syntouch, 2013); b) Photo of the BioTAC NumaTac Technology (Syntouch, 2013)

A highly sensitive sensor capable of measuring multiple modalities is required to achieve the aims of this programme of research. The state-of-the-art sensor at the time the experiments were completed was the original BioTAC; hence this is the sensor used throughout this research and is explained in detail in Section 2.4.

2.4 BioTAC Biomimetic Tactile Sensor

Loeb et al. (2011), define biomimetic design as the process of designing machines that incorporate principles of operation of living organisms. The BioTAC^{TM} biomimetic tactile sensor proposed by Syntouch® is a finger-shaped sensor array that provides simultaneous information about contact forces, microvibrations and thermal fluxes induced by contact with external objects (Yamamoto et al., 2012; Lin et al., 2009). The design of the fingertip incorporates the low-pass filter effects of fluid and cosmetic skin into the transduction process in a similar manner to a biological fingertip (Wettels et al., 2008). A solid core containing all of the finger's electronics and a conductive fluid surrounding the core are enclosed by a silicone elastomer skin and a plastic finger nail. Wettels et al. (2008) discuss how various textures for the inner surface of the skin were evaluated by using simplified finite element models in the development of the silicone elastomer skin. Analysing impedance versus force relationships of various moulded skins enabled the selection of the appropriate material for the skin which, when coupled with the appropriate fluid, proved to greatly reduce hysteresis and diffusion loses (Wettels et al., 2008). Initial testing of impedance

when the sensor was systematically probed in a 4×5 grid demonstrated a spatial resolution of below 2mm in relation to the point of contact (Wettels et al., 2008). Wettels et al. (2008) state that by analysing data collected from the array of electrodes during contact with an object, it is possible to determine the contact force magnitude and direction, the location of force centroid, the object shape (e.g. curvature, sharp edge etc.), the object hardness/softness and contact transients and vibration. Figure 2.10 shows a cross section view of the BioTAC fingertip in which is seen a hydro-acoustic pressure sensor housed in the rigid core, which also houses the impedance sensing electrodes and thermistor at the tip of the finger.

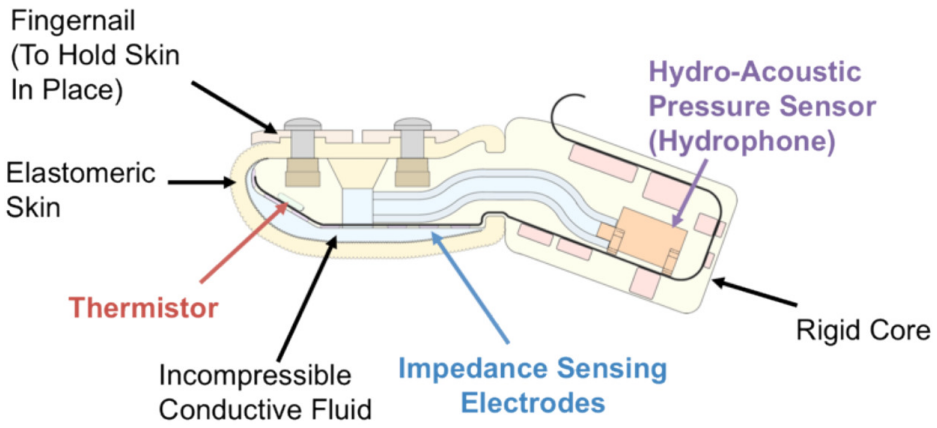

Figure 2.10: Cross Section View of BioTAC Fingertip Tactile Sensor (Syntouch, 2013)

There are various sensors on the fingertip that enable retrieval of the aforementioned sensory information. An array of 19 electrodes measures the force applied on the fingertip by reading the impedance between each electrode and four common excitation electrodes. As the impedance over a sensing electrode increases, the measured voltage decreases demonstrating contact in that area of the finger. Having a 19 electrode array allows the exact point of contact on the fingertip to be derived. Furthermore, it enables multiple points of contact to be derived at any instance. Inside the core of the fingertip there is a pressure sensor (located in the rigid core). This sensor reads pressure changes in the conductive fluid located between the hard core and the elastomeric skin. The skin has a fingerprint, similar to that of a human, moulded on its surface. When contact is made with a material, microvibrations are caused by the movements within the fingerprint causing the pressure change in the conductive fluid. The vibration sensor outputs two different data types; one is the static fluid pressure i.e. absolute fluid pressure (PDC), which is the reading obtained after passing through a low pass filter. The other is a measurement of the microvibrations

sensed from the electro-conductive fluid, i.e. dynamic fluid pressure (PAC), which has been passed through a band pass filter. The PAC data represent the extent of the vibration that the fingertip has sensed when in contact with objects or materials. The final sensory data that can be retrieved from the BioTAC fingertip are the static temperature (TDC) and thermal flow (TAC) data. The TAC data represent the rate at which heat is leaving the fingertip and transferring to/from the object or material with which it is in contact. This is made possible by the thermistor which is located in the tip of the fingertip. Table 2.1 shows the maximum range, resolution and frequency response of the sensory modalities available in the BioTAC when the high sampling PAC is interleaved with the other channels (PDC, TAC, TDC, Electrodes 1-19) at a rate of 4.4kHz (Fishel, 2012).

Table 2.1: Table specifying the range, resolution and frequency response of the sensory modalities available in the BioTAC sensor (Fishel, 2012)

Sensory Modality	**Symbol**	**Range**	**Resolution**	**Frequency Response**
Impedance	E	$0 - 3.3V$	$3.2mV$	$0 - 100HzV$
Fluid Pressure	PDC	$0 - 100kPa$	$36.5Pa$	$0 - 1040HzV$
Microvibration	PAC	$\pm 0.76kPa$	$0.37Pa$	$10 - 1040HzV$
Temperature	TDC	$0 - 75°C$	$0.1°C$	$0 - 22.6HzV$
Thermal Conductivity	PAC	$0 - 75°C/s$	$0.001°C/s$	$0.45 - 22.6HzV$

These data are used throughout this thesis, however due to the equipment used the frequency of data collection changes. This is explained in more detail, as necessary, in Chapter 4, Chapter 5 and Chapter 6.

2.5 Conclusion

This chapter has provided a brief overview of human tactile sensing, highlighting its complexity and how difficult it is to replicate. An overview of existing tactile sensors and their capabilities and an introduction to the BioTAC tactile sensor that is used to collect all tactile data utilised in this work have also been presented. Hardware utilised for collecting tactile data has also been discussed. Chapter 3 builds on this and focuses on research which utilises tactile data to learn information from objects following direct contact.

CHAPTER

THREE

Computational Intelligence in Tactile Sensing

3.1 Introduction

Humans can quickly gain information about an object or material simply by viewing it from different angles; for example they can estimate how it might feel to touch or how heavy it may be. This is due to our highly sophisticated visual capabilities and ability to adapt prior knowledge learned from similarly shaped and known objects. However, regardless of our heavy dependence on vision as our primary sense, there are some properties which are difficult or even impossible to detect by vision alone, for example thermal conductivity, compressibility or a determination of the material an object is made from. In order to learn these characteristics and remember them for future interactions, physical manipulation of an object is required. Distinguishing between objects and materials of different compressibility, temperature and texture or sensing small vibrations such as a human pulse on a wrist can be achieved by performing complex manipulation tasks such as squeezing or rubbing.

This chapter provides an overview of commonly used computational classifiers for tactile-sensing based experiments such as object or material identification. Furthermore, a summary of research utilising tactile sensing, particularly in material identification, is presented followed by a review of recent research conducted using the BioTAC sensor.

3.2 Machine Learning

Two popular machine learning classifiers are Artificial Neural Networks (ANN) and Support Vector Machines (SVMs) and therefore these classifiers, and combinations of them, are primarily used in this work for material identification in Chapter 4. Variations of ANN, such as Multi-Layer Perceptron (MLP), together with other classifiers such as Gaussian Mixture Models (GMMs), Linear Discriminant Analysis (LDA), Naïve Bayes (NB) and *k*-Nearest Neighbour (*k*-NN) are also evaluated for material identification and therefore are briefly explained. A Fuzzy logic based classification system is utilised in Chapter 6 for identifying the health status of a human and is therefore also briefly explained in this section. All classification algorithms are utilised from tool boxes within (MATLAB, R2013) and R from the (R Core Team, 2013). A detailed description of the inner workings and mathematics behind the algorithms is not presented but, references throughout the descriptions provide extra detail if desired. Novel hybrid combinations of the utilised algorithms were designed and evaluated.

3.2.1 Artificial Neural Networks (ANN)

The brain may be considered to be a complex, non-linear and parallel computer. It has the ability to perform complex tasks such as pattern recognition, perception and motor control much faster than any electronic computer, even though events occur in the *nano*-second range for silicon gates, and *milli*-seconds range for natural neural systems (Engelbrecht, 2007). One of the aims of computational Intelligence is to replicate this ability in artificial systems. An ANN is just one example of a paradigm of Computational Intelligence (CI) which, according to Engelbrecht (2007), is *the study of adaptive mechanisms to enable or facilitate intelligent behaviour in complex and changing environments*.

Neural Networks (NN) are networks or circuits of biological neurons. ANNs are a computational tool modelled on the interconnections of neurons in the nervous system of the human brain. ANNs mimic the hugely dense and parallel processing ability of the brain (Wasserman, 1989) and are comprised of large arrays of interconnected computational elements, know as neurons. The brain consists of approximately 10^{11} neurons (Jain et al., 1996), each having the possibility of being connected to 1000-10000 other neurons, resulting in approximately 10^{14} to 10^{15} synaptic interconnections (Schalkoff, 1997). An ANN is a network of many non-linear computational elements connected

by adjustable weights, often implemented as a mixture of serial and parallel executions paths on a standard computer.

Typically an ANN will possess one or more network inputs, an input layer, hidden layer(s) and an output layer with weighted connections between neurons in the same layer and different layers, an activation function, output units and a learning algorithm. The network will consist of interconnected neurons which work in unity to solve particular problems. There are many variations of an ANN (e.g. temporal ANNs, self-organising ANNs, spiking ANNs) but a typical example is a second generation back-propagation feed forward network (with bias). Figure 3.1 shows a sketch of the structure of a second generation ANN.

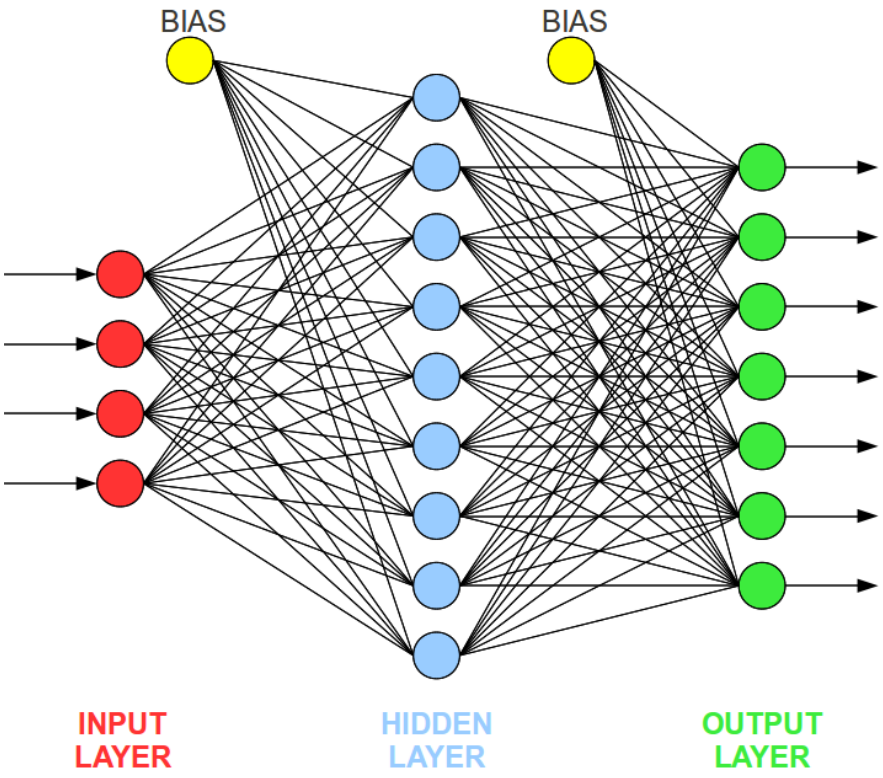

Figure 3.1: An example of a fully connected feed-forward network with one hidden layer

ANNs have been used for a wide range of applications, including diagnosis of diseases, speech recognition, data mining, image processing, robot control, classification, credit approval and many more. More specifically, ANNs have been utilised as a classifier in many approaches using tactile sensory information to classify between materials and/or objects (Drimus et al., 2012; Chathuranga et al., 2013; Ho et al., 2011).

A variation of an ANN is a Multi-Layer Perceptron (MLP). This is a feed-

forward ANN model that maps sets of input data onto a set of appropriate outputs and utilises back-propagation for training the network (Rosenblatt, 1962; Rumelhart et al., 1986). Like any ANN, an MLP has multiple layers of neurons with each layer fully connected to the next one. However, in an MLP each input node is a neuron with a non-linear activation function. As it is a modification of the standard linear perception, an MLP can distinguish data that are not linearly separable (Cybenko, 1989).

3.2.2 Support Vector Machine (SVM)

A SVM is a useful and well established technique used in machine learning to learn and classify data (Cortes and Vapnik, 1995). In their simplest form, SVMs are non-probabilistic binary linear classifiers that build a model based on a set of training samples which belong to one of two categories and is then capable of assigning new samples to one category or the other. The SVM model is a representation of the labelled samples as points in space which are mapped in separate categories with a clear gap between them. Based on the learned information, new samples are then mapped onto the same space in the model and therefore predicted to belong to one category or the other (Cortes and Vapnik, 1995).

However, a common difficulty with a SVM is that it is not possible to linearly separate the data (Press et al., 2007). Therefore in a non-linear SVM, it is required to map the input data to a higher dimensional space through the use of a kernel function (KF) (ϕ), as represented by the image in Figure 3.2.

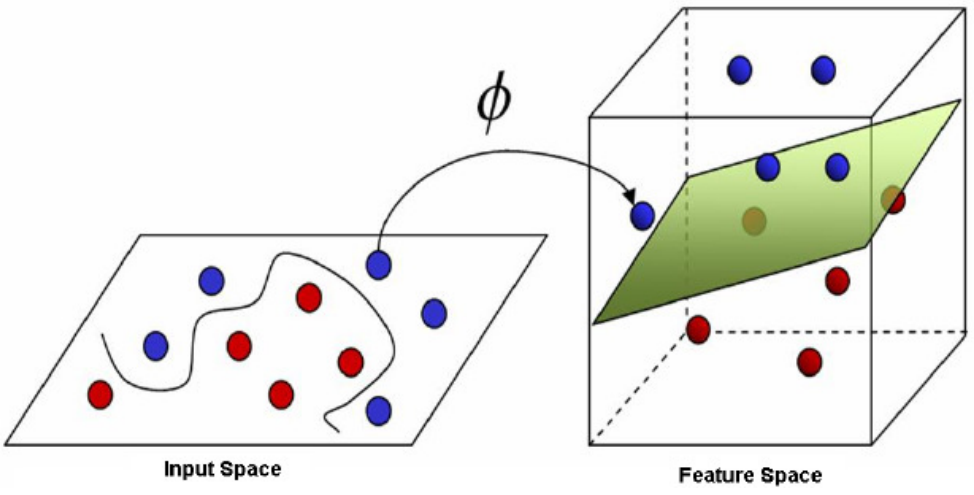

Figure 3.2: A sketch representing the use of a kernel function for non-linear SVM classification (Moreira, 2011)

Binary classification alone is not suitable for the material classification task in Chapter 4; therefore, the standard SVM algorithm has been adapted to enable multi-class classification for materials. Two common ways of utilising binary SVM classification techniques, to allow for multi-class classification, are by either having a sequence of numerous one-versus-one binary classifiers or by having a multiple one-versus-all classifier (Duan and Keerthi, 2005). The approach utilised in this work is a series of one-versus-all classifiers in which the system is trained with each class classified against the samples of all the other classes, to develop a SVM multi-class classifier.

3.2.3 Gaussian Mixture Model (GMM)

The Gaussian probability density function (PDF) is a bell shaped curve defined by two parameters, mean and variance. The Gaussian distribution is commonly used for approximating a class model shape in a selected feature space. It is assumed that the class model is truly a model of one basic class, however if the actual PDF is multi-modal it fails. A GMM is a mixture of several Gaussian distributions and is therefore able to represent different subclasses within a class. The resulting probability density function is defined as a weighted sum of the Gaussian distributions that make up the GMM. The PDF of the GMM can be used to calculate the likelihood of any new input data within each class and identify the class for which the PDF generates the maximum likelihood, hence classifying the data. The expectation maximisation (EM) algorithm is an iterative method for calculating the maximum likelihood distribution in GMMs (Dempster et al., 1977).

3.2.4 Linear Discriminant Analysis (LDA)

LDA finds a linear combination of features that characterises or separates two or more classes of objects or events by creating the linear combination which yields the largest mean differences between the classes (Martinez and Kak, 2001). It is a generalisation of Fisher's linear discriminant (Mika et al., 1999; Müller et al., 2001; Fukunaga, 1990) and it is a widely used method in statistics, pattern recognition and machine learning. The linear combination can then be used as a classifier or for dimensionality reduction before classification. Similar to principal component analysis (PCA), which is also used for dimensionality reduction, LDA looks for linear combinations of variables which best explain

the data (Martinez and Kak, 2001). LDA explicitly attempts to model the difference between the classes of data. The accuracy of LDA and indeed any of the classification techniques can be defined as

$$CA(\%) = \frac{\text{Tests classified correctly}}{\text{Total Tests}} * 100 \tag{3.1}$$

In the case where there are more than two classes (instead of dimensionality reduction), LDA can still be used in a variety of different ways. For example, a "one against the rest" approach could be applied where points from one group are put into one class and all the rest of the points from the other groups are put into another, then LDA applied. Another common method is pairwise classification, where a new classifier is created for each pair of classes with individual classifiers combined to produce a final classification. In this work LDA is used for multi-class classification to identify materials individually and into their groups, although it can be used for binary or multi-class classification.

3.2.5 Naïve Bayes (NB)

NB is a family of classifiers capable of binary or multi-class classification. Rather than the classifier taking all features of a class into account collectively to describe the class, all NB classifiers assume that the value of a particular feature is completely independent of any other feature in the class. Hence NB classifiers can be trained very efficiently during a supervised learning task, (Rish, 2001).

A NB classifier is a simple probabilistic classifier based on applying Bayes' theorem with strong (naïve) independence assumptions. Although quite a simple classifier, it has proven to be very effective in some texture classification approaches (Ho et al., 2011). The NB classifier is based on the assumption that given the target value of the instance, the probability of observing the conjunction of attributes is just the product of the probabilities for the individual's attributes. Therefore, the NB classifier reduces a multivariate problem to a group of univariate problems by ignoring the possible dependencies (correlations) among the inputs (Islam et al., 2007). Hence the NB classifier is much simpler than a standard Bayesian learning algorithm, although this does mean that it is not as effective for more complex classification problems, especially since only one simple joint probability distribution is used per class (Klawonn and Angelov, 2006). However, considering its simple nature, it is rather straightforward to implement and therefore is very commonly considered and evaluated

for many classification tasks.

3.2.6 *k*-Nearest Neighbour (*k*-NN)

k-NN is a non-parametric method that can be used for classification or regression. *k*-NN is quite a simple algorithm and straightforward to train and use and this is likely to be the reason why it is still a popular choice as a classifier (Drimus et al., 2012). There are three main elements to this approach: a set of labelled objects stored in a database (e.g. tactile array images, forces applied, credit history, stock market records), a calculation of the distance between the objects and the value of *k* itself, which is the number of nearest neighbours.

When used for classification, an object is assigned to the class which is most common amongst its *k* nearest neighbours following a majority vote. The number of neighbours is defined by the user and is normally a small positive integer, for example if *k*=1 then the object is assigned to the class of the single nearest neighbour or if *k*=3 then the most popular class amongst the three closest neighbours is the class that the object will be assigned to.

However, *k*-NNs also have their weaknesses; the main weakness being that generally, in its simplest form, *k*-NN makes the assumption that all features are of equal importance and therefore assigns equal weight to each, regardless of whether they are relevant or not. So not only does this mean that it is not possible to distinguish between more and less relevant features but it also means that totally irrelevant features can have an adverse effect on the outcome.

k-NN assumes that each $x = \{x_1, x_2, ..., x_n, x_c\}$ is defined by a set of n features, where x_c is x's class value (discrete or numeric). Given a query q and a case library L, *k*-NN retrieves the set K of the k most similar features (i.e. of least distance from the query) in L and predicts their weighted majority class value as the class value of q. The distance that is defined for all points in a dataset is described as:

$$\text{Distance}(x, q) = \sqrt{\sum_{f=1}^{n} (w_f \times \text{difference}(x_f, q_f)^2)} \tag{3.2}$$

where w_f is the parameterised feature weight value assigned to feature f and the value of k is a smoothing factor affecting the classification. When there is noise or outliers present in the input data, a small k may result in misclassification. Conversely, a large k can lead to over generalisation, hence the range of k values

that is tested for each problem is very important. However, this can lead to a further disadvantage of the *k*-NN algorithm considering the increase in the calculations to be performed when the training space is large.

3.2.7 Fuzzy Logic

Zadeh (1965) first developed fuzzy logic in his seminal work on fuzzy sets. In a traditional set, an element is either in or not in the set. In contrast, a fuzzy set is a generalisation of the traditional set in which an element can have partial membership to one or more sets. The driving force behind fuzzy sets was to model uncertainly and slight inaccuracies within the reasoning process (Zadeh, 1965). It is not always possible to describe things in an absolute state. For example, we describe the temperature in weather with terms like "cold", "a little bit cold", "hot, "really hot" etc. It is these properties which makes Fuzzy logic the ideal selection for determining the health status of humans based on the combined vital sign measurements, as presented in Chapter 6.

Each element in a fuzzy set is mapped by a value of "trueness" for its membership to a set. This value is between 0-1, where 0 represents complete non-membership of the fuzzy set and 1 represents complete membership. This mapping is called the membership function and it completely describes the fuzzy system. Examples of membership functions can be triangular, trapezoidal or Gaussian in shape (Kuncheva, 2012). A Gaussian membership function is commonly used in Fuzzy-based classifiers and an example set of Gaussian membership functions can be seen in Figure 3.3.

Using the decomposition theorem, fuzzy sets can be decomposed into crisp sets (Yuan et al., 2011). The three elementary set theoretic operations of two fuzzy sets are union, intersection and complement. Using these operations, the user can define and interpret fuzzy sets. Each fuzzy rule consists of two parts - the premise and the consequent. The premise is the "if" part and the consequent is the "then" part (Abe, 2012). Using a series of these rules the user can configure the fuzzy system to fuzzily classify events or data inputs into non-rigid descriptors.

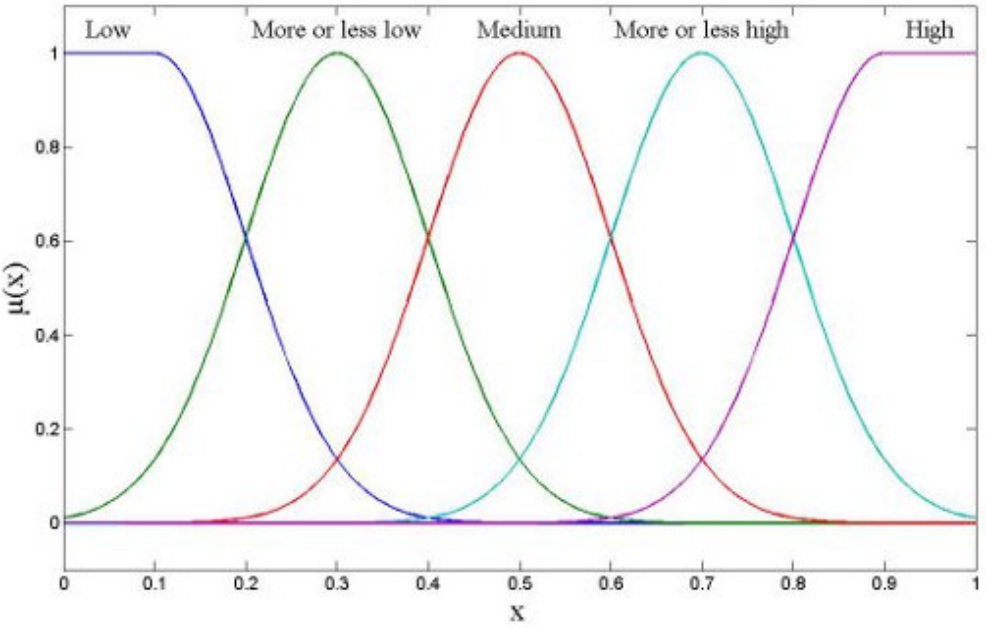

Figure 3.3: A graph showing Gaussian membership functions with a Fuzzy Classifier (Hameed and Sorensen, 2010)

3.3 Machine Classification using Tactile Sensing

For tactile information retrieval there is a need for physical contact to be made with the object, material or human. Therefore, full exploration of the object can be time consuming as contact can only be made in patches equivalent to the size of sensor being used. However, tactile sensors supply various attributes about objects they contact that vision sensors simply cannot, for example compressibility. This section reviews current literature on machine learning methods used for tactile sensing based material identification.

3.3.1 Material Classification using Tactile Images

Despite initially receiving less focus than vision based methods for material identification, research into tactile methods for object attribute learning and identification is now very active. Although tactile information is retrieved through a range of available sensors, for example tactile array sensors or simple force pressure sensors, many approaches convert tactile information to image based representations for learning an object. A common characteristic of an object that can be represented by tactile images is compressibility, i.e. is it rigid or deformable? Tiest (2010) described the compressibility or stiffness of

the object as the ratio between the force applied to an object and the resulting displacement of the object. The compressibility of the object will determine how much force is required to grasp the object firmly. If the object can be squeezed to half its width, for example, then it will be important that the correct amount of force is applied by a robot manipulator to ensure a non-destructive grasp. In contrast, if the object is not compressible at all, i.e. it cannot be squeezed, then it is equally as important to ensure that there is not excessive force applied which may crack or smash an object. Pezzementi et al. (2011) presented an approach which utilises computer vision algorithms to allow tactile sensor readings, representing compressibility, to be considered as images. The tactile array sensor explores the object and images representing contact made with the array are produced. Six feature descriptors including the well known Scale Invariant Feature Transform (SIFT) (Lowe, 1999) and MR-8 (Varma and Zisserman, 2005) are used to extract features from these images. The Bag-of-Words (BoW) approach (Jurie and Triggs, 2005), commonly used in computer vision methods, is then used to learn and classify the objects based on these features. The majority of evaluation was carried out in simulation and some on real world datasets collected from objects using the tactile array sensor. It was stated that although this method showed some promise for object detection from physical contact, there is still some work required. Another similar approach by Schneider et al. (2009) used low-resolution intensity images from a tactile array sensor, which were obtained when the robot grasped an object. A BoW approach was then applied to model the appearance of images and by the use of unsupervised clustering on training data, a vocabulary from tactile observations was learned that is used to generate a histogram codebook. The method was capable of an average recognition rate of 84.6% across household and industrial objects. However, the method struggled somewhat when classifying between industrial objects only (such as a cylinder, triangle, cuboid and a handle) with a classification rate of 58%. It was stated that further work on the method for grasping the objects was required. Drimus et al. (2011), present a technique to classify between rigid and deformable objects using a sensor they developed and compared their results to those obtained using a commercial sensor. Ten rigid and deformable household objects are squeezed in a gripper with force sensors fitted. The squeeze is described as "palpation" motion as the gripper closes on the object until contact is made. After contact is made, the gripper closes by a further 1mm for five iterations or until a maximum force is achieved, depending on the compressibility of the material being grasped, i.e. the object is solid with no compression or it cannot be compressed any further. A set of tac-

tile images for the force applied to each area of the tactile array was collected for each complete set of "palpation" grasps of each object. The first two moments of each tactile image were extracted as two independent features to reduce dimensionality. The first feature corresponded to the average of the image and the second to the standard deviation of the pixels in the image. The Dynamic Time Warping algorithm (Sakoe and Chiba, 1978) was used to calculate the distance between the time series of images. A *k*-NN classification was utilised to classify the different objects, based on their compressibility. The results showed that the algorithm was more successful when it took data from both sensors (i.e. from each gripper) and features into account rather than either one individually. Classification accuracy of up to 92% was achieved for 10 objects ranging from a rubber ball to a plastic bottle. The algorithm struggled to distinguish between similarly compressible objects even though the objects were very different, for example a "bad orange" and an empty bottle were found to have similar compressibility and therefore the algorithm failed to classify these objects correctly. Luo et al. (2015) also present an approach which utilises tactile images and a BoW approach to object recognition. An optimised BoW approach and dictionary were produced by considering different outputs of the classic BoW with different dictionary sizes for different views of objects. The classification performance of this optimised approach was compared against the performance of the classic BoW model utilising 12 objects. It was found that the proposed approach outperformed the classic BoW model particularly for classification of objects with similar features. Sato et al. (2008) also turn tactile sensing into a purely visual approach. They utilise a fingertip manufactured out of a clear, compressible rubber and there are tiny blue and red markers embedded in this rubber. These markers move location when contact is made on the finger and the rubber is compressed. The markers are monitored by a small charge-coupled device (CCD) camera embedded where the finger nail would be. This camera tracks the motion of the markers and then force vector field calculations are utilised to calculate the magnitude of the force applied and where contact is made on the fingertip.

A novel "Gelsight" tactile sensor was proposed by Johnson et al. (2011) to produce tactile images of surface texture. It consists of a camera capable of up to 2 microns resolution and an elastomer coated with a reflective membrane. Later, Li and Adelson (2013) proved that this sensor was capable of measuring surface texture across 40 classes of textures made from materials such as wood, sandpaper and fabric. The "Gelsight" produces a height map when it is pressed against a surface which the authors treat as an image and process

it using standard tools for visual texture analysis. A novel texture recognition system, Multi-scale Local Binary Pattern (MLBP) based on the standard Local Binary Pattern (LBP) system (Ojala et al., 2002), enhanced by using a multi-scale pyramid and a Hellinger distance metric, classifies material surfaces with an accuracy of 99.79% across the 40 test surfaces. Although these methods have shown that they can be used to identify or classify between materials and objects in the majority of cases, a lot of the methods struggle with distinguishing between materials or objects that have similar compressibility or texture. This is due to assessing just one modality when classifying the material. The work presented in this thesis aims to take more than one modality into account when using machine learning techniques for material identification.

3.3.2 Material Classification based on Surface Texture

According to Tiest (2010), roughness is the most studied material property in the context of tactual perception. Chathuranga et al. (2013) investigate the ability of a biomimetic fingertip developed by the authors to discriminate between different fabrics based on the texture of their surface alone. The proposed biomimetic fingertip is designed to mimic the functions of a human fingertip, although to allow for the use of commercially available sensors it is approximately two and half times the size of the average human thumb. The fingertip contains five accelerometers and eight force, single contact point, sensors and is fixed horizontally to the test materials and then moved in an exploratory motion called the active touch (moved forward initially, stopped for 0.5 seconds and then moved back in the same path). The experiment was carried out on seven types of materials, six of which are fabrics and one is a polished aluminium surface. The fingertip's ability to classify between the textures was evaluated. Using ANNs as classifiers, accuracies of up to 85% were achieved. However, some textures were frequently misclassified such as polyester and acrylic. Ho et al. (2012) assess the ability of their developed sensors to classify between three different materials (denim, a photo and tape). Multiple machine learning algorithms are tested, such as NB, a multilayer ANN with input extracted from autoregressive models and an ANN with input extracted from the discrete wavelet transform (DWT). It was found that the ANN with input extracted from DWT performed the best out of all of the machine learning techniques with classification of 91% accuracy between two very different materials, i.e. denim and a photo. However, as well as performing the best out of all the learning algorithms tested, this was the

most computationally expensive by far. In contrast the NB was very simple in implementation, although the accuracy of classification was much lower, dropping to 67% between denim and a photo. It is shown that neither method can distinguish accurately between the two similar materials, namely the photo and tape.

Drimus et al. (2012) presented an active exploration approach using a piezoelectric Polyvinylidene Fluoride (PVDF) thin film sensor mounted inside a silicone shell. Contact is made with the test materials using a contact and release procedure and features are extracted in order to classify different objects by their surfaces. During feature selection, methods such as PCA, LDA and Bayes Optimal LDA are tested for dimensionality reduction. The best results were achieved by removing selected features from the original set and using Bayes Optimal LDA. Three classification algorithms were considered for learning the features; *k*-NN, ANN and SVM. Five artificial (man-made) surfaces (i.e. grades of sandpaper) and six 'natural' (found in everyday life) textures (i.e. dish cloth, floor cloth, polished wood, aluminium, unpolished wood and plexiglass) where used as test materials with 20 training samples acquired for each. It was found that the *k*-NN and SVM performed equally well with average classification rates of over 90%. Although this approach could distinguish between different grades of sandpaper it struggled with the common problem of being able to distinguish between two similar materials, such as two types of cloth. A similar approach by Decherchi et al. (2011), assessed the suitability of computational intelligence approaches for tactile data-processing. Various learning algorithms were tested considering the trade-off of accuracy versus computational efficiency. The SVM was found to have obtained the best results. However this method also struggled to distinguish between similar surfaces, for example distinguishing between wood and brass. This is a drawback of many approaches to surface classification and identification. Jamali and Sammut (2010) propose a method which used an artificial fingertip to slide along materials and collect vibration data. A total of seven materials were tested including sponge, carpet, wood, two tiles of different roughness and two pieces of vinyl of different roughness. A Bayes classifier was trained with the Fourier coefficients of the sensor output data retrieved from the sliding motion over each material. It was shown that the authors' classifier performed well for classification between dissimilar surface textures; however, their approach was unable to distinguish between two types of tiles, as the texture of the surfaces were similar. Jamali and Sammut (2011) extended this work to evaluate multiple classifiers and added a majority voting algorithm. In a similar way to their previous work, data

were retrieved from the fingertip making contact with test materials. The test materials included the same seven as in their previous work with the addition of a second type of carpet (different roughness), making eight material surfaces in total. Whilst the fingertip was being rubbed over each surface, different textures induced different intensities of vibration in the silicon fingertip. As in their previous work, the data from the fingertip were pre-processed and the Fourier coefficients of the sensor outputs were used as inputs to various classifiers that were implemented in the WEKA machine learning toolkit (Hall et al., 2009). It was found that the best performance of 95%$\pm$4% was achieved using the NB tree (NBTree). The system struggled most when trying to classify between materials of similar roughness.

Kaboli and Cheng (2015) use the Shadow Hand fitted with a BioTAC tactile sensor on each finger and the thumb to identify objects whilst in-hand, based on their surface texture. The method uses prior knowledge obtained from six objects to attempt to distinguish between four new objects. The objects are held in place by the Shadow Hand, while the middle finger (MF) and thumb (TH) are used to slide the BioTAC sensor over the object for 1cm. The Shadow Hand is controlled by a Cyber Glove configured to enable the Shadow Hand to mimic the actions of the human wearing the Cyber Glove. The expectation maximisation (EM) algorithm was utilised to differentiate between different categories of objects based on their texture properties. When attempting to identify the four new objects based on their category determined by the EM algorithm, there were many objects that were confused with previous dissimilar objects which may have had similar surface textures. However, when training a Least Squared SVM with one data set per each of the four objects the system achieved 83% accuracy in identifying the four objects and when the training samples are increased to 10 and the priori knowledge of six objects from previous experiments is added, 100% accuracy is achieved. Although impressive, it is important to remember that this is identifying between just four objects. However, it is an interesting approach to utilise previous knowledge. The authors improved upon this work by collecting data from 20 household objects held in the Shadow Hand, calculating tactile descriptors from the data and using these to train different learning algorithms to successfully discriminate between the objects (Kaboli et al., 2015). The data were used to train the SVM, Passive Aggressive Online Learning (PA) and EM learning algorithms for comparison. The SVM algorithm performed best with up to 97% accuracy, followed by the PA algorithm which achieved up to 87% and lastly the EM algorithm which achieved 82% accuracy across the 20 objects. Even though these accuracies are

extremely high, the algorithms struggle to distinguish between similar objects such as a spongy ball and a rough ball.

3.3.3 Material Classification based on Thermal Characteristics

Another characteristic of a material that can be assessed and possibly used to identify a material/object is thermal characteristics. Although one can generally tell the difference between materials that feel hot and cold, one would struggle to relate a list of similar materials to their actual thermal conductivity. What human fingers detect thermally is not the absolute temperature of the material alone, but also its thermal conductivity and diffusivity. This is due to the fact that the human finger is at a consistent temperature, approximately 34° Celsius, and therefore will be different from the ambient temperature of most objects we encounter. The nerves of the finger detect the flow of heat from the source, suggesting that human temperature sense may be emulated by thermal conduction sensing (Monkman and Taylor, 1993).

Jianfeng et al. (2011) use a thermal sensor to classify between materials of different roughness. A simulation is run using ANSYS software to simulate the change in temperature from the time of contact with the test material. For the practical experiment a "Surface Air Layer" is proposed to examine the affect of having a thin layer of air on a material during contact. Classification between six materials of different surface roughness was achieved, but a specific accuracy was not given. It is discussed that the simulation was not as accurate as the practical experiments and some behaviours were different at the point of initial contact; the behaviours discovered during the practical experiments were much more difficult to model. The system struggled to distinguish between materials of different roughness' and the "Surface Air Layer" improved this slightly but not sufficiently.

Bhattacharjee et al. (2015), present another approach that focusses on material classification. Their approach uses a tactile sensor consisting of a thermistor that is capable of measuring solely thermal properties and they focus on classification within a short period of time, for instances where longer term contact is not viable. Three classification algorithms are considered, SVM+PCA, *k*-NN+PCA and Hidden Markov Model (HMM). It was found that SVM+PCA performed best with classification rates of 84% with 0.5 seconds of contact and 98% with 1.5 seconds of contact across 11 materials with varying initial con-

ditions and 3-fold cross validation. Although the classification rates achieved are impressive, the materials tested varied widely in thermal conductivity and the purpose of the sensor is solely to determine thermal properties; it therefore cannot measure material properties such as texture or compressibility, thus limiting the applications for which it can be used. Bhattacharjee et al. (2016) continued this research and presented a method for distinguishing between contact with inanimate objects and humans, using a new portable handheld device developed by the authors consisting of three tactile sensing modalities: a force sensor to detect contact, a heat-transfer sensor that is actively heated, and a small thermally-isolated temperature sensor (Wade et al., 2015). Data was collected from the arms of 10 human participants from 3 different locations on the right arm and 80 objects consisting of 8 similar objects from 10 different bathrooms (Bhattacharjee et al., 2016). The effect of varying durations of contact made with the human participants and the objects was also evaluated. A SVM was used to learn to classify between an object and human in the first instance and it achieved an average classification accuracy of 98.75% when contact was held for 3.65 seconds, 93.13% for 1.0 second of contact and 82.13% for 0.5 seconds of contact. High classification accuracies were also achieved when generalising to new contact locations within the same bathroom with an average of 92.14% for 3.65 seconds of contact, 91.43% for 1.0 second and 84.29% for 0.5 seconds. However, when generalising to new environments, i.e. similar objects in different bathrooms, accuracies were lower achieving 84.00% for 3.65 seconds of contact, 71.00% for 1.0 second and 65.00% for 0.5 seconds. Like many other methods it struggled to identify similar objects especially when the environment changes.

3.3.4 Material Learning Classification based on Multiple Characteristics

Johnsson and Balkenius (2008) compared mono-modal and multi-modal approaches measuring just texture or both texture and hardness of materials. They found that the multi-modal approach was more effective at recognising the hardness of more objects although it was less effective at recognising individual objects. Although Johnsson and Balkenius (2011) progressed this work by modelling the object shape, texture and hardness by grasping and manipulating the object, they also struggled to distinguish between very similar objects. Their approach used Self Organising Maps (SOM) to learn the shape of the objects

and their surface features. Kroemer et al. (2011) present an approach to classify surface texture using a straightforward oscillator-based designed tactile sensor consisting of a compliant pin that makes contact with the surface and a capacitor microphone that can detect the pin's vibrations at 44.1 kHz. The training phase of the experiment also incorporates visual information of the surface's texture. Pairings amongst the data modalities are correlated in order for the system to learn each surface. During the testing phase only the tactile sensor is used to collect data and determine the classified surface. The three dimensionality reducing algorithms evaluated were PCA, Mean Maximum Covariance Analysis (μMAC) and Weakly-Paired Maximum Covariance Analysis (WMAC). It was found that WMAC dimensionality reduction was the most robust method, however both the μMAC and WMAC methods are capable of enabling the surface texture to be classified from tactile sensing alone following their use for dimensionality reduction of both visual and tactile data in the training stage. It was stated that for effective use in object identification further work on effective pre-processing of both the visual and tactile data is required.

Hoelscher et al. (2015) use a BioTAC fingertip sensor to collect several features from a range of 49 objects to develop a system capable of identifying material and recognising objects. The objects are made of materials including plastic, metal, stone ceramic, paper etc. They collect data by making static and lateral contact on each material with the BioTAC sensor. The authors then compare seven different methods of extracting features from their processed data, including temporal data, PCA reduced dimensionality raw data, pressure features, electrode features, physically motivated features, temperature features and mean features. The authors compare two generative (NB and Gaussian) and two discriminative (SVM and Random Forests) classifiers to evaluate identification of the materials and objects from the collected data. The best performing method consisted of an SVM classifier with dimensionality-reduced mean values of filtered data, achieving a classification accuracy of material identification of over 97% across a range of surfaces from 49 objects some of which had very different surfaces. However, the algorithm struggled to classify between similar surfaces within a material category, for example 58% classification accuracy was achieved when classifying different ceramic materials.

Xu et al. (2013), presented an algorithm which considered three key properties of a material to enable classification; compliance (compressibility), texture and thermal conductivity. To collect data for these three key properties a BioTAC fingertip was mounted on a Shadow Robot Hand. Based on a Bayesian explo-

ration approach in the authors' previous work (Fishel and Loeb, 2012a) three exploratory movements were selected and used to explore ten test materials. A classification accuracy of 99% using 10 materials was achieved with the only failure being that a damp sponge was classified as a feather. The approach in Xu et al. (2013) also obtained 99% classification, but this was using 10 substantially different materials, varying from a brick to a light feather. Therefore, the materials have very different properties allowing for more straight forward classification. Furthermore, all three tactile properties were used making the system both slow and computationally expensive.

It may be concluded that using just one material property does not allow for desirable classification of materials and combining modalities can lead to high computation cost. The ideal scenario would be to design a system that can perform classification with accuracy similar to that of Xu et al. (2013), using similar materials, with reduced computational burden and hence run in real-time (or close to). An overview of the best performing machine learning methods for the application of material identification using tactile sensing can been seen in Table 3.1. It demonstrates that the biggest difficulty in classification of materials is between similar materials or materials of similar roughness. Although, this is to be expected, it is still an ongoing challenge within the field.

In order to attempt to solve the difficulty of distinguishing between similar materials, i.e. two hard, smooth surfaces of wood and brass, more than one characteristic of the material must be measured. State-of-the-art technology in tactile sensing allows this to happen as outlined by Lin et al. (2009) who utilise the BioTAC finger tactile sensor from Syntouch to distinguish not only the roughness or compressibility of a surface but also calculate a temperature transient upon contact with an object to identify general material classes of plastic and metal of different thickness. Fishel and Loeb (2012a) use the BioTAC sensors for a Bayesian exploration method for the intelligent identification of textures. Classification was achieved from a set of 117 textures of everyday materials including 9 paper-like materials, 5 types of glass, 4 tiles and laminates, 3 types of wood, 3 types of foam, 8 types of rubber, 11 cottons and silks, 8 different engineering materials (e.g. milled aluminium), 12 types of vinyl, 6 types of leathers and suedes, 2 furs, 16 coarse weaves (e.g. flannel), 16 other fabrics and textiles (e.g. crushed satin) and 14 art supplies and miscellaneous materials (e.g. velvet paper). This approach related the textures to human style descriptions frequently used in psychophysical literature exploring texture discrimination (i.e. sticky/slippery, rough/smooth). The focus in Fishel and

Table 3.1: Table comparing tactile sensing-based material identification methods

Research Group	**Machine Learning Method**	**Sensor Type**	**Accuracy achieved (%)**	**Description**
(Xu et al., 2013)	Probability Matrices	Multi-modal tactile sensor (BioTAC)	99.00	10 very different materials were used. Continuous exploration and three modalities required therefore high computational costs.
(Hoelscher et al., 2015)	SVM	Multi-modal tactile sensor (BioTAC)	97.00	Struggled to distinguish between similar materials. Required training from all materials in the group
(Drimus et al., 2011)	*k*-NN	Single Mode piezoresistive tactile sensor array	92.0	Classification across just 10 objects. Struggled to identify between similar objects.
(Chathuranga et al., 2013)	ANN	Multi-modal tactile sensor	85.0	Classification across just 7 materials, 6 of which were fabrics.
(Ho et al., 2012)	ANN	Single Mode electro-conductive soft skin sensors	81.0	Reported to be a very computationally expensive approach.
(Drimus et al., 2012)	*k*-NN, SVM	Single Mode PVDF thin film sensor	90.0	Classification across different grades of sandpaper but struggled between similar materials.
(Jamali and Sammut, 2011)	NBTree	Single mode silicon tactile sensor with PVDF films	95.0	Struggled to distinguish between materials of similar roughness.
(Kaboli et al., 2015)	SVM	Multi-modal tactile sensor (BioTAC)	83.0	Classification across just 4 materials.
(Bhattacharjee et al., 2015)	SVM	Single mode thermistor-based tactile sensor	98.0	Longer contact with materials required for maximum accuracy
(Bhattacharjee et al., 2016)	SVM	Multi-modal Hand-held tactile sensor	98.8	Classification accuracies achieved across already learned data, accuracy drops to 84.0% when tested against new data from the same materials.

Loeb (2012a) was to find the most useful exploratory motions on the surface of the material, relating to six general types of exploratory movements that humans make when tactually exploring objects, as outlined by experimental psychologists Lederman and Klatzky (1987). Also, as part of this study Fishel (2012), observed at forces less than 2Newton (N), the change in fluid pressure of the BioTAC was linearly correlated with contact force as shown in Figure 3.4. However, at forces greater than 2N the relationship is no longer linear due to the fact that the skin of the BioTAC comes in contact with the core. The authors used this observation to lower the BioTAC on to the material with a stepper motor whilst monitoring the applied force with a Nano17 sensor and ensuring it did not exceed 2N in preparation for lateral movements and this has been utilised in the design of the experiment in Chapter 4.

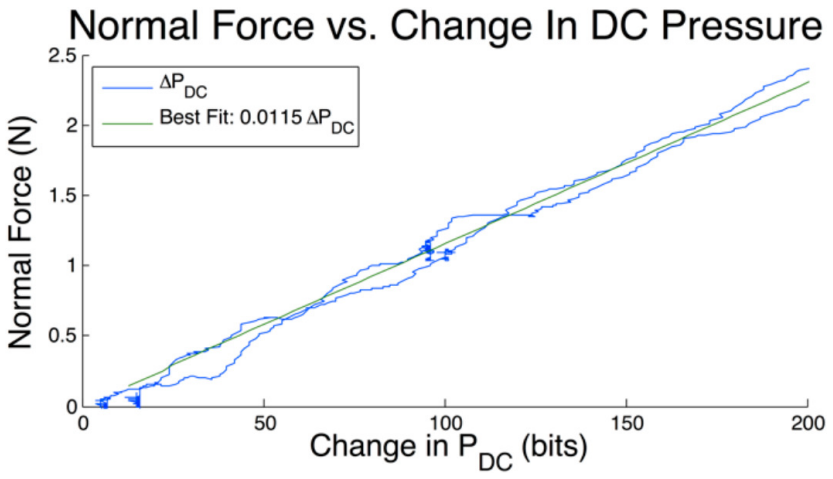

Figure 3.4: Graph showing the change in DC pressure measured by the BioTAC as the normal force increased and decreased during loading and unloading (blue lines) (Fishel, 2012)

3.3.5 Machine Learning using the BioTAC

This section focusses on machine learning algorithms used with data collected from the BioTAC fingertip. Wettels et al. (2009) use the data from the BioTAC tactile sensor coupled with Bayesian inference to calibrate control of an anthropomorphic mechatronic prosthetic hand to adjust the grasp of a cup being filled with liquid at varying rates. The authors collect impedance data from the electrodes housed in the BioTAC sensor and use a Kalman filter to calculate a force from the normalised voltages collected by the sensor. It was found that the sensor could detect slip when the cup was filled at a slow fill rate (between 6-57 seconds to fill 250ml of liquid). However, it was less able to handle very rapid

perturbations (4 seconds to fill 250ml), maintaining hold of the cup by adjusting the grasp according to detected slippage in 4 out of 5 trials in comparison to 100% success rate in the trials with a slower fill rate. Wettels and Loeb (2011) also used the force modality data coupled with numerous machine learning algorithms to identify the point of application of force, force vector and radius of curvature. The learning algorithms included GMMs, SVMs and ANNs and the results indicated that an ANN was the best algorithm for identifying features from the BioTAC data.

Veiga et al. (2015) address the ongoing challenge of in-hand manipulation in robotics by developing a system to predict and counteract slip events when grasping unknown objects. The authors use the BioTAC fingertip sensor mounted on the end of a Mitsubishi PA-10, 7 Degrees of Freedom (DOF) robot arm. An external RGB-D camera, namely an Asus Xtion Pro, is used to capture the robot's work space to record each trial and enable a human to manually determine when slip of the object occurs. Objects ranging in shape and stiffness including a ball, cup, measuring stick, box, marker, watering can and tape are held between the robot fingertip and a vertical plane. Sufficient pressure is applied to hold the object in place and then the robot arm and fingertip are moved away from the object gradually until slip occurs and eventually the object falls. The authors train two classifiers with the slip data, a SVM and a random forest classifier, in order to attempt to learn how to predict when a slip is about to occur. When a slip is predicted the robot arm applied more force to the object in order to prevent it from falling. The random tree classifier was found to perform best for four of the seven objects and on average best overall. The ball was found to be the hardest object to identify or predict when a slip would occur. However, with the delta random forest classifier achieving 95% accuracy for predicting slip, the system was found to be a feasible approach for predicting slip via tactile sensing and stabilising objects by feedback control.

Fishel and Loeb (2012b) present details of the signal processing techniques within the BioTAC finger demonstrating that the accuracy of the micro-vibrations readings of the finger tip can sense a range of very small particles from as light as 0.422mg. The particles are dropped on the finger from a height of 7cm. The BioTAC sensors were tested to determine if they could detect the impact and were compared to five human volunteers who were tested to recognise impact with the same particles. The only particle that could not be detected at all by the BioTAC sensors was the 0.25mm (mass 0.072mg) solder ball; all others were detected with a 100% classification rate. The human participants were also

unable to identify that they felt impact with the 0.25mm solder ball and could only manage 47.5% and 74.86% classification with the 0.45mm (mass 0.422mg) solder ball and 1mm aluminium bearing (mass 1.461mg) respectively. 100% classification was achieved by the participants for the remainder of the particles. The performance of the BioTAC in this experiment was a major breakthrough with regards to the hardware and software available for tactile research.

Ciobanu et al. (2014) present several novel solutions for identifying the point of contact and normal force estimation when contact is made with an object by a Shadow Robot Hand mounted on the end of a Kuka robot arm and equipped with a BioTAC fingertip. The algorithms build on earlier work presented by the authors outlining a pre-processing tool box for tactile data collected using a BioTAC sensor (Ciobanu et al., 2013). Data were collected from the BioTAC fingertip when contact was made with objects of different shapes and a Support Vector Regression (SVR) algorithm was applied to these data in order to identify a point of contact and develop a visual contact map by presenting areas of contact in red and areas of non contact in blue. Although this could be used in many applications to identify a point of contact on the BioTAC sensor, it is reported that the SVR algorithm can be very time consuming to train, up to several minutes in fact which may not be suitable in applications where a rapid identification of contact is required or a system requires regular training to update its suitability for the application.

Pacchierotti et al. (2014) present a novel approach to enable a human to touch objects within a remote environment using a BioTAC sensor which records data and maps them back to a custom made cutaneous device that can be worn by a human. The device is a 3 DOF cutaneous device consisting of two platforms, one at the back of the finger and one at the front of the fingertip. The platforms are connected by three cables whose lengths are controlled by motors that can move the lower plate towards the user's fingertip and re-angle it to simulate contact with surfaces of varying angles. The device then portrays what was sensed by the BioTAC sensor by relating the data to input commands for the cutaneous device motors in real time without using any form of skin deformation techniques. The Approximate Nearest Neighbour C++ library by Mount and Ayra (2010) was used to help map the data collected by the BioTAC to the nearest motor positions in the cutaneous device that reflect the forces and angles felt by the BioTAC. This initial work is significantly extended when the authors extend the data set collected to approximately 4.6 times larger than the original and by carrying out a comprehensive object evaluation by placing the

BioTAC into the cutaneous device and comparing the data collected together with a subjective evaluation of the system involving ten users (Pacchierotti et al., 2015).

Hui et al. (2016) also use the BioTAC to identify artificial tumours by distinguishing between lump-containing and non-lump-containing areas of artificial skin made from Eco-Flex 00-10 silicon rubber in which 25 3D-printed lumps were inserted to simulate tumours. In contrast to the approach used by Arian et al. (2014), Hui et al. (2016) used a palpitation movement of the fingertip against the material to collect data and in turn attempt to classify between regions that contain artificial tumours and those that do not. Two sets of data from the BioTAC palpating at 10,260 points across the artificial skin were collected over two different days. The data collected consisted of readings from 19 electrodes and one DC pressure. A multivariate Gaussian model was fitted to a training set of the data and when tested for classification between lump and non-lump-containing areas, near perfect classification accuracies were achieved. However, when tested on the second set of data the Gaussian learning model was reported to perform dismally. Therefore, the authors transformed the 20 tactile sensor array readings into 190 binary pairwise comparisons, inspired by robust perceptual methods from computer vision. It was found that this novel approach achieved accuracies of approximately 80% across both datasets. Although the pairwise comparison method outperformed the Gaussian model, the authors suggest that feature extraction could further improve the pairwise comparison models.

Table 3.2 shows an overview of machine learning algorithms that have been used with BioTAC data. It can be seen that there have been a wide range of applications where the BioTAC has been utilised, however the learning methods that are common and perform best are ANN, SVM and GMM. Although a wide range of applications and learning algorithms have been applied to data collected from tactile sensors and in particular the BioTAC sensor, there are still many remaining research problems in the field of tactile sensing. In terms of material classification, the problem of distinguishing between materials of similar texture and/ or compressibility remains a challenge. Furthermore, there has been no work completed to date on using tactile data collected from the BioTAC to assess human vital signs. Both of these research areas are addressed in this work. A number of the learning algorithms discussed in this chapter and novel hybrid combinations of them are utilised for the application of material classification in Chapter 4. Noise reduction algorithms discussed in this chapter

Table 3.2: Table comparing Machine learning methods used on BioTAC data

Research Group	**Machine Learning Method**	**Application**	**Description**
(Wettels et al., 2009) (Wettels and Loeb, 2011)	GMMs, SVMs and ANNs	Control of an anthropomorphic mechatronic prosthetic hand	ANN proved to be the best algorithm for identifying features
(Veiga et al., 2015)	SVM, Random Forest	predict and counteract slip events	Random Forest classifier was found to be best for detecting slip
(Fishel and Loeb, 2012b)	Band-pass filtering for noise reduction	Compare the sensitivity of the BioTAC with a human fingertip	BioTAC could sense particles from a weight of 0.422mg. Only one particle that could be sensed by humans could not be sensed by the BioTAC.
(Ciobanu et al., 2014) (Ciobanu et al., 2013)	SVR	Identifying the point of contact and estimation of normal force	The SVR algorithm was found to be very time consuming to train, making it not suitable for applications where a rapid identification of contact is required.
(Hui et al., 2016)	*k*-NN, A multivariate Gaussian model	Tumour Detection	Gaussian model performed very poorly. Authors transformed sensor array readings into 190 binary pairwise comparisons and used computer vision techniques achieving great success.

coupled with novel methods to assess human vital signs using data collected via a BioTAC sensor are presented in Chapter 5 and Chapter 6.

3.4 Conclusion

This chapter has provided an overview of computational intelligence methods using tactile data. The work in this thesis work presents the use of computational intelligence techniques in real-life applications. Machine learning approaches are utilised to classify materials in Chapter 4 and for combining human vital signs in order to ascertain a human's health status in Chapter 6. A review of the current research in material identification achieved using tactile sensing and machine learning was presented. Section 3.3 provided a background of the machine learning methods utilised to date for material identification, leading to the proposed method for tactile-based material identification presented in Chapter 4. Also, a focussed review on computational intelligence techniques using data collected from the BioTAC sensor for material identification and other purposes was presented, as this is most relevant to the work in this thesis. This overview highlights the sensitivity of the BioTAC sensor and confirms its suitability for collecting highly sensitive data such as a human's pulse or breathing, as detailed in Chapter 5. Furthermore, approaches which utilise a mix of both tactile and vision data were discussed in Section 3.3.5, as a mixed approach consisting of tactile sensing based control and vision sensing based analysis is utilised in Chapter 6 to measure a human's Capillary Refill Time (CRT).

CHAPTER

FOUR

Tactile Sensing Based Material Classification

4.1 Introduction

Research into tactile methods for object attribute learning and identification is now a very active field of research, despite initially receiving less focus than vision based methods for object identification. Due to the lack of sophisticated sensors available for tactile sensing research in recent decades, the field progressed slower than other fields such as vision focussed research (Lee and Nicholls, 1999a). However, Syntouch® recently developed the BioTAC™ biomimetic tactile sensor which is capable of achieving tactile perceptions similar to that of humans, enabling the possibility of identifying objects and their properties including texture, compressibility and thermal properties (Fishel and Loeb, 2012a) and (Xu et al., 2013). The BioTAC sensor has been used in all experiments reported in this thesis.

Identification of the material from which an object is made is of significant value for effective robotic grasping and manipulation. Compressibility, surface texture and thermal properties are characteristics which can each be retrieved from physical contact with an object using tactile sensors. In order to produce the tactual perceptions required to learn about object properties, humans inherently perform various types of movements when interacting with an object. As outlined in Chapter 1, experimental psychologists, such as Lederman and Klatzky (1987), have identified six general types of exploratory movements. Humans can complete these exploratory movements very fast and rapidly evaluate the object leading to possible identification.

One of the main application areas of an artificial tactile sensing system is

expected to be in robotics. In order to retrieve the necessary tactual perceptions, it is probable that a robot must explore an object in a similar manner to that of a human. However, in comparison to humans, these exploratory movements may be slow for a robot and could lead to the evaluation of a great volume of acquired data, thus being computationally expensive. It would be a useful skill for a robot if it could complete a preliminary evaluation of the object by quickly identifying the physical nature of the material (e.g. metal, wood, plastic etc.) through completing a small number of initial basic actions, thus removing the need for extensive manipulation. These initial basic actions could include the retrieval of thermal information upon initial contact with the material, which may provide an indication of its physical nature. Furthermore the texture of a material could possibly be identified by sliding a robotic hand or finger along the material, i.e. determining if it is rough or smooth.

This chapter presents a system for texture classification by collecting data using a BioTAC fingertip in contact with various materials and then using these data to classify the materials both individually and into groups corresponding to their type. Following acquisition of data, principal component analysis (PCA) is used to extract features. These features are used to train seven different classifiers and hybrid structures of these classifiers for comparison. The seven classifiers implemented and tuned are a standard feed-forward Artificial Neural Networks (ANN), Support Vector Machine (SVM), Gaussian Mixture Model (GMM), Linear Discriminant Analysis (LDA), Naïve Bayes (NB), *k*-Nearest Neighbour (*k*-NN) and a Multi-Layer Perceptron (MLP) ANN. For comparison, an experiment for evaluating human performance when classifying the same materials is also presented. The goal of the work presented in this chapter is to determine the sensitivity of the BioTAC sensor in order to determine its full potential in tactile based sensing.

The work in this chapter was published in the:

- IEEE International Conference on Robotics and Biomimetics (ROBIO), China (Kerr et al., 2013). This work detailed the methods developed for the classification of materials by their thermal conductivity and was presented in China in December 2013.
- IEEE International Conference on Control, Automation, Robotics and Vision (ICARCV), Singapore (Kerr et al., 2014a). This work extended the work detailed in (Kerr et al., 2013) by introducing the analysis of the texture of materials coupled with their thermal conductivity to achieve

improved classification accuracy and was presented in Singapore in December 2014.

- Irish Machine Vision and Image Processing, Northern Ireland (Kerr et al., 2014b). This work presented further extension to the work detailed in (Kerr et al., 2014a) by evaluating more classifiers and developing a two-stage approach to material classification and was presented in Northern Ireland in August 2014.

Furthermore, the work outlined has been submitted as a journal article to the Elsevier Journal of Expert Systems with Applications (Kerr et al., 2017) and is currently under review.

4.2 Methodology

Using the BioTAC fingertip, two actions were performed on different materials in order to determine if the fingertip sensory system is capable of distinguishing between them. The first action was a press action where the fingertip was pressed into the material at a constant force. The second action was a slide action where the fingertip was dragged across the surface of the material at a constant force. Both actions replicate, to some extent, two of the actions that a human completes when inspecting an unknown material for the first time, namely static contact to determine thermal properties and lateral sliding movements to determine surface texture. The thermal flow (TAC) and static temperature (TDC) values only are extracted from the press action as they represent the thermal difference between the fingertip and material; collecting the vibration data from this action would not be beneficial as there is no lateral movement therefore changes in vibration would be minimal. Furthermore, it was determined that changes in the impedance values during a press action would not be suitable for classification of the material type in these experiments. Firstly, the impedance reading would relate to compressibility for the material which was not the focus of this work and secondly, as the BioTAC is a highly non-linear device susceptible to drift (Syntouch, 2013) it was empirically determined that continuous calibration would be required to prevent the drift in the impedance readings. The TAC, TDC, dynamic fluid pressure (PAC) and absolute fluid pressure (PDC) values are extracted from the slide action. This is because significant change is expected in vibration and thermal based data due to the lateral movement of the fingertip being rubbed across a material. These data are subsequently used for classification, as described in Section 4.2.1.

Fourteen materials are used in both the press and slide experiments. Some of the materials are similar (i.e. two types of metal, two types of wood and two types of cardboard) in order to determine if the approach is capable of classifying the type (group) of material and furthermore distinguishing between similar materials within a group. The 14 materials are Acrylic (Ac), Rough Acrylic (AcR), Copper (Cr), Aluminium (Al), Rough Copper (CrR), Rough Aluminium (AlR), Redbrick (R), Glossy Cardboard (GC), Plain Cardboard (PC), Soft Foam (S), Carpet (Ct), Doormat (D), medium-density fibreboard (MDF) (M) and Pine (P). Although similar to three of the other materials, the rough materials have a very rough surface in comparison with their smooth counterparts. This roughness was apparent when dragging a finger across the surface. Examples

of each material can be seen in Figure 4.1; 15 trials of each material were completed.

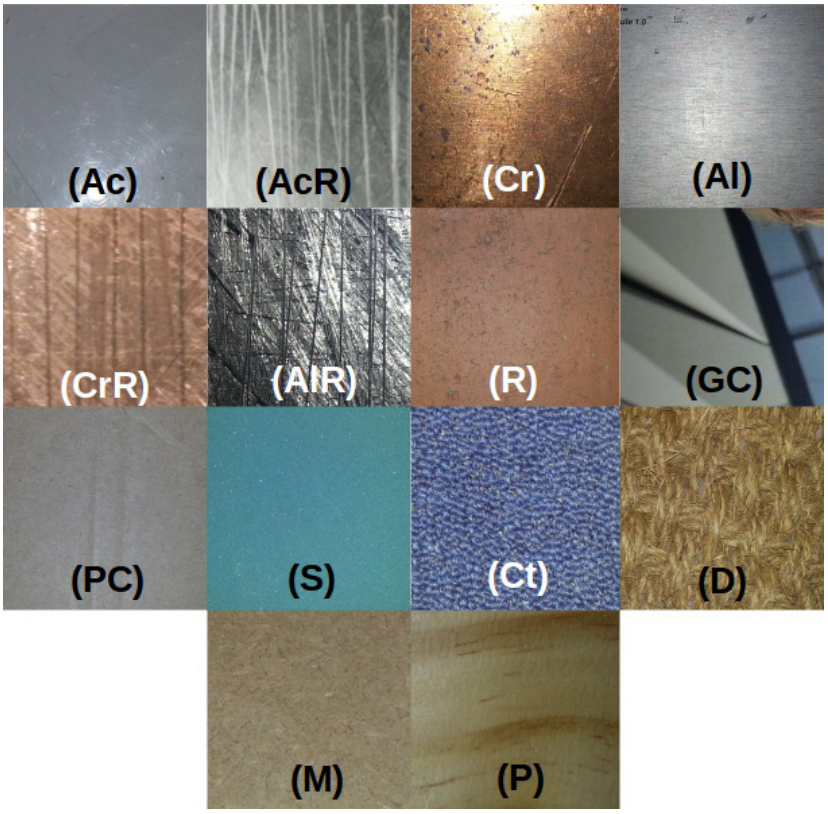

Figure 4.1: Samples of the 14 materials used in the experimental set-up.

The aim of this research is to initially classify each material in terms of its group type, for example MDF and pine are both in the wood group. The materials tested were split into six groups. The individual materials and the groups to which they belong are shown in Table 4.1. Subsequently, the aim is to classify each material individually within each material group. This helps to establish the sensitivity of the BioTAC sensor.

4.2.1 Data Collection

Analogous with the experiments reported by Xu et al. (2013), in these experiments the BioTAC fingertip was powered on and left to rest for 15-20 mins to allow it to reach its steady state temperature (approximately 35°C, 10°C above ambient). A rig including a motorised arm and turntable was designed and built for the experiments carried out in Chapter 4. We designed the metal structure of the rig and it was manufactured by a local engineering company as per our designs. All the other non-electrical components for the rig were designed

Table 4.1: Table showing the individual materials and the groups to which they belong.

Material	Group
Acrylic (Ac)	Plastic (P)
Rough Acrylic (AcR)	Plastic (P)
Copper (Cr)	Metal (Me)
Aluminium (Al)	Metal (Me)
Rough Copper (CrR)	Metal (Me)
Rough Aluminium (AlR)	Metal (Me)
Redbrick (R)	Masonry (Ma)
Glossy Cardboard (GC)	Cardboard (C)
Plain Cardboard (PC)	Cardboard (C)
Soft Foam (S)	Fabrics (F)
Carpet (Ct)	Fabrics (F)
Doormat (D)	Fabrics (F)
MDF (M)	Wood (W)
Pine (P)	Wood (W)

by us using the Solid Works 3D design package (SolidWorks, 2016) and manufactured on a 3D printer within Ulster University. Two stepper motors (one for the arm and one for the turntable) were connected to an Arduino Uno™ board and a Graphical User Interface (GUI) was developed using Python to control the motors. An image of the experimental rig and GUI can be seen in Figure 4.2(a) and (b) respectively. The BioTAC fingertip was placed at the end of the motorised arm so that it could be moved towards or away from the material. A Serial Peripheral Interface (SPI) protocol for digital communication from the BioTAC was used and a "Cheetah" high-speed SPI/Universal Serial Bus (USB) device manufactured by Total Phase (Total Phase, 2017) was used to connect the fingertip to the computer and retrieve data. A GUI developed and supplied by Syntouch on LabVIEW (National Instruments, 2017) was used to communicate with the SPI controller and collect the data. The various test materials were placed on the motorised turntable to allow them to be moved below the finger to replicate a sliding action.

To produce the thermal exploratory movement, the fingertip is pressed onto the material with a constant force of 3N, measured by an ATI Nano17 6-axis Force/Torque (F/T) Sensor (ATi, 2017). To allow time for the heat flow to stabilise, all data for the press action were collected from the fingertip for 20 seconds after initial contact. Fishel (2012) state that for a lateral exploratory movement, contact force should be kept at less than 2N in order to maintain

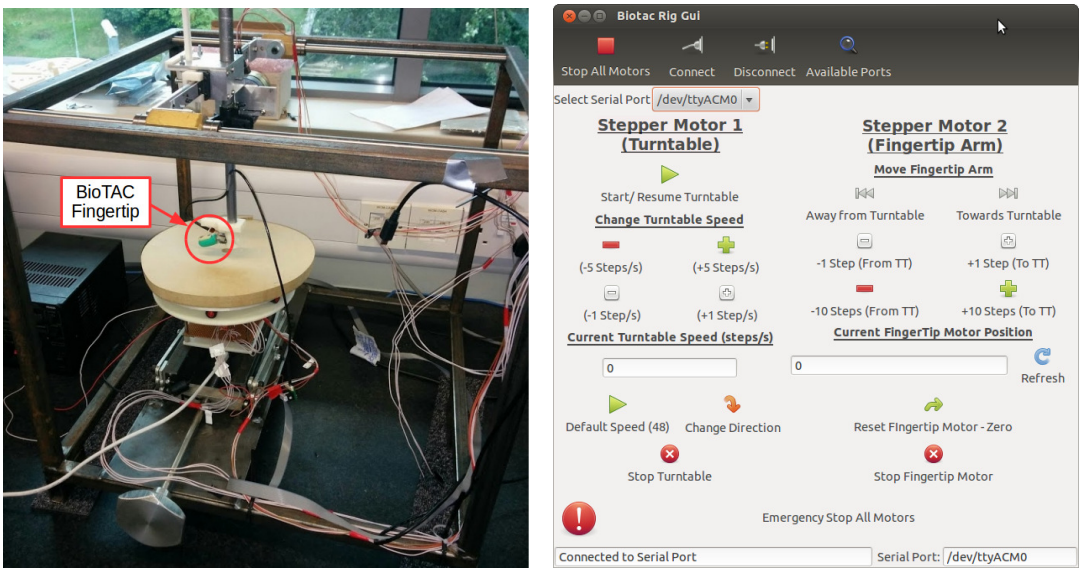

(a) (b)

Figure 4.2: a) Image showing the experimental rig; b) Screen shot of the developed GUI.

a linear relationship between contact force and fluid pressure. Therefore, to produce the slide action, the fingertip was pressed down on the surface of the material again, this time with a constant force of 1.59N (also measured with the aforementioned force sensor), and slid along the surface for a distance of approximately 5 cm. When using the manufacturers software to collect data, the data from the BioTAC fingertip are recorded at 4400Hz and in a sequence, with the PAC values and the individual electrode values alternating (i.e. PAC data are recorded at 2200Hz). All other values such as TDC (static temperature), TAC (thermal flow rate) and PDC (static vibration) are given at the end of each sequence of values. An example of this sequence can be seen in Figure 4.3. All values are sampled with 12-bit resolution. These values are extracted and individual datasets for PAC, PDC, TAC and TDC data are obtained using MATLAB.

4.2.2 Pre-Processing

The area of interest in the thermal conductivity time series data is the behaviour following the point where maximum force of contact is made. Therefore, data that occur prior to the point of maximum force of contact (the point of highest thermal conductivity) are excluded from the TAC and TDC datasets corresponding to the press experiment. Empirically it was found that a period of 8 seconds

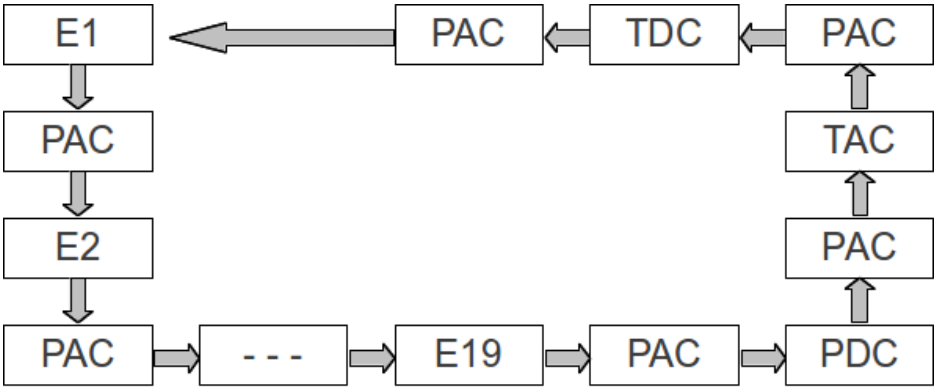

Figure 4.3: Diagram showing the Sequence of Data from the BioTac Fingertip

was sufficient for the thermal conductivity data to stabilise hence representing a constant thermal flow rate and therefore data for a period of 8 seconds after maximum contact were included. These datasets for TAC and TDC each consist of 800 values. For sliding movements, it is important to crop the beginning of the data in order to allow the data to stabilise and avoid noisy sensor signals caused from the establishment of contact, as confirmed by Hoelscher et al. (2015). Therefore, a subset of 220 pieces of data for each of the four modalities (TAC, TDC, PAC, PDC) is selected from the data collected during the slide motion.

Preliminary experiments using raw data as inputs to various machine classifiers were performed but poor performance was achieved during training. Therefore, PCA was applied to the modalities' datasets to reduce the dimensionality of the inputs. PCA projects the original dimensional space onto a linear subspace where the latter is always smaller than the original dimensional space, such that the variance in the data is maximally explained with the smaller subspace represented by principal components (PCs). Features (or inputs) that have little variance are therefore removed, (Engelbrecht, 2007). In this chapter, PCA is used to extract the features of the time series data for TAC, TDC, PAC and PDC in order to reduce their dimensionality into smaller datasets, which are a representation of the TAC, TDC, PAC and PDC data for each material.

PCA can be completed in two ways; by calculating the eigenvectors in order to perform Eigen-decomposition of a data covariance matrix or by singular value decomposition (SVD) of a data matrix. The data are normalised in both instances before the application of PCA. To calculate PCA by Eigen-decomposition the covariance matrix of the normalised data matrix X was calculated for each data modality, giving XX^T. X is a $n \times p$ matrix where n is the total number of data samples collected across all materials and p is the number of data points

for each set. In the matrix X, n consisted of 14 materials with 15 trials of each, totalling 210 data samples and p consisted of 800 data points for data collected during the press experiments or 220 data points for data collected from the slide experiment. We then calculate the eigenvectors and their associated eigenvalues from the covariance matrix. The eigenvectors with the greatest eigenvalues are the PCs of the data matrix. In contrast, when calculating the PCs by using SVD we decompose the matrix X (considering that $n \neq p$) using SVD to get:

$$X = USV^T \tag{4.1}$$

where U is a $n \times n$ orthogonal matrix of the left singular-vectors, S is a $n \times p$ matrix of the singular values of the matrix X and V is a $p \times p$ orthogonal matrix of the right singular-vectors.

As $n \neq p$ and each row of X is centred in all of the matrices of data, the principle components are represented by the left singular vectors. The diagonal elements in S represent the square of the eigenvalues. Finally the principal component scores, which are the coordinates of the assays in the space of principal components, are contained in the matrix SV^T. Both variations of PCA were tested to validate which method would provide the best principal components with which to train the classifiers. A range of classifiers were evaluated in preliminary experiments with raw data, PCs obtained from applying PCA using Eigen-decomposition and PCA using SVD in order to classify between 14 individual materials. With these data, using the PCA Eigen-decomposition based approach for generating PCs generated the best inputs to the classifiers, as determined by the training accuracies of multiple experiments. For example the training accuracies for an ANN were 70.60% when using raw data, 90.36% when using PCs obtained from applying PCA using Eigen-decomposition and 89.05% when PCs obtained from applying PCA using SVD. Therefore, the method and results presented in subsequent sections are based on the use of PCA with Eigen-decomposition. In initial experiments, where thermal properties only were considered, PCA was applied to the combination of TAC and TDC (a total of 1600 values), requiring 100 PCs to represent the modalities for each material. Although this was a relatively successful method, it proved to be computationally expensive. Therefore all approaches outlined in this chapter apply PCA to each individual modality first. This allows combinations of the different modalities to form a matrix of the principal components for each material to suit each experiment (i.e. the principal components calculated from TAC and TDC for the press experiment and principal components calculated

from TAC, TDC, PAC, PDC for the slide experiment). As described in Section 4.3, these combinations of principal components are used to train the numerous classifiers and hybrid combinations of classifiers evaluated.

4.2.3 Initial Data Analysis

The extracted thermal and vibration data were normalised and are visually analysed in order to determine if the BioTAC sensor is sensitive enough to distinguish between different materials.

Figure 4.4(a) shows an example of the TAC values collected from the fingertip during a constant press of 3N on five of the 14 test materials. It is evident, in the plot for the heat flow (thermal conductivity) of the fingertip, that when contact is made with each material, there are some materials with clear differences in thermal properties.

It can be seen from Figure 4.4(a) that the most thermally conductive material is copper, as the line representing copper plateaus notably above the remaining materials. The lower lines in the graph represent materials with a lower conductivity, e.g. pine, which is also to be expected. It should be noted that the thermal conductivity for the rough metals does not plateau above the other materials like their smooth counterparts. For example, Figure 4.4(a) illustrates a clear difference between copper and rough copper. It is clear that the surface texture affects thermal conduction between the fingertip and the material. Furthermore, there exists a difference between the two different types of cardboard, (one sample of cardboard has a glossy high print quality finish while the other is plain cardboard with no print finish). Even though they are the same core material, the rate of heat flow leaving the fingertip and entering the material differs notably and also plateaus at a different value.

Figure 4.4(b) illustrates a subset of the PDC values collected from the fingertip during a constant slide action along four of the 14 materials. It is evident that the surface texture of some materials results in clear differences in the magnitude of vibration detected when the fingertip was slid along the material. Figure 4.4(b) illustrates that the material that caused the largest magnitudes of vibration (i.e. the roughest material) was the doormat, whereas smoother materials such as acrylic present a constant smooth line representing very small magnitudes of vibration. This initial analysis clearly illustrates that material classification using learning algorithms should, in theory, be possible.

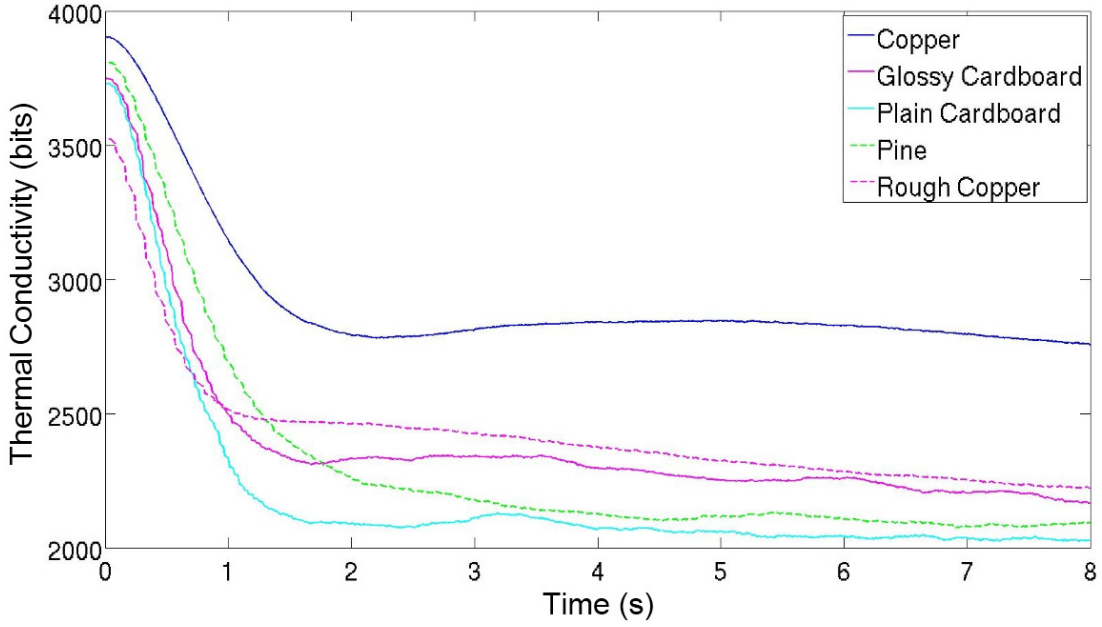

(a)

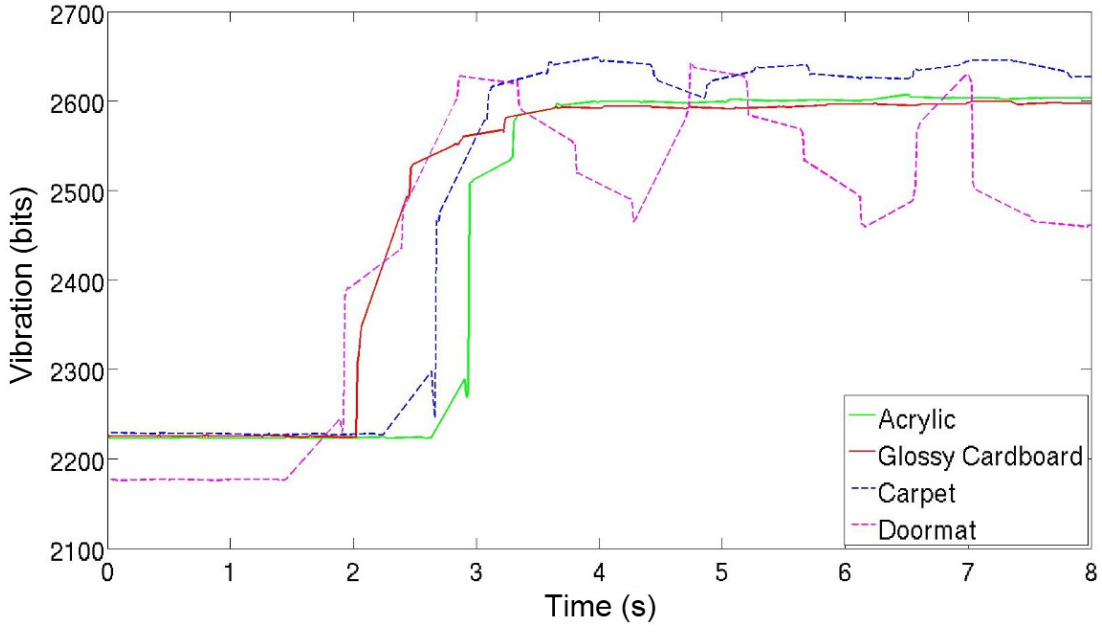

(b)

Figure 4.4: a) Thermal conductivity behaviour following point of maximum force of contact for five of the fourteen test materials; b) Vibration measured during a slide action along four of the fourteen test materials.

4.3 Classifiers

PCA using Eigen-decomposition was applied to the data collected from the fingertip during the press and slide experiments in order to extract features. Following the evaluation of various quantities of principal components to represent the modalities' data sets, it was empirically determined that the optimal number of PCs for each dataset using PCA is three, providing the best trade off for performance versus speed. Therefore, as there are six modalities in total to represent each material (two from the press action and four from the slide action), there is a total of 18 inputs (three PCs per modality, 12-bit values) to each classifier for each experiment. Average classification accuracy is obtained using 5 fold cross validation. The MATLAB package (MATLAB, R2013) and R package (R Core Team, 2013) were used to implement the range of classifiers. As noted in Chapter 2, two common classifiers in tactile sensing applications are SVM and ANNs. Variations and combinations of these two classifiers have been implemented and evaluated in this work along with other popular classifiers; this section outlines the details of the classifiers used.

4.3.1 One-stage Support Vector Machine

A standard binary SVM configuration was used for instances where there were only two material groups to be classified. However in the majority of instances, there were more than two materials or groups to be classified and therefore a series of one-versus-all classifiers, in which the algorithm is trained with each class classified against the samples of all the other classes, are developed to form a multi-class SVM classifier. Although there are many types of kernel functions (KFs) available to overcome the difficulty of linear separation of the data, five are evaluated and their performances compared. Within each KF there are various parameters that can be changed to optimise the performance of the classifier. One common parameter is the *soft margin* (sometimes known as the *box constraint*), C. The purpose of the soft margin is to modify the SVM algorithm to tolerate training errors by intuitively tolerating a few outliers on the wrong side of the hyperplane. Deciding on the size of the margin requires parameter tuning and optimisation. The KFs evaluated for the classification of materials and their respective parameters that were optimised are:

- Linear kernel function (LKF), quadratic kernel function (QKF) and multi-layer perceptron kernel function (LMPKF): Soft margin value (C) is opti-

mised.

- Polynomial kernel function (PKF): Two parameters are optimised in this KF; the soft margin value (C) and the order of polynomial (p). Various combinations of values were evaluated in order to find the best performing combination of parameters.
- Radial basis function kernel function (RBFKF): Two parameters are optimised in this KF; the soft margin value (C) and the gamma parameter for the Gaussian radial basis function (RBF) (γ). The Gamma parameter is a positive number representing the scaling factor of the RBF. Various combinations of values were evaluated in order to find the best performing combination of parameters.

Two separate experiments were conducted: one for the classification of the materials into their six respective groups and one for the classification of the fourteen individual materials. All KFs were evaluated and their parameters optimised for both experiments. For each optimised KF implemented and evaluated, three different methods for calculating the separating hyperplane were also implemented and evaluated. The three standard methods evaluated were sequential minimal optimization (SMO), quadratic programming (QP) and the least-squares (LS) method. A summary of the classification accuracies for classifying the material groups is shown in Table 4.2, with the best performing parameter configurations for each method highlighted in bold text and the worst performing highlighted in italic text.

For the PKF and the RBF KF, as well as a range of values for the soft margin parameter (C) being evaluated for each KF and separating hyperplane method, a range of values for the order of the polynomial kernel (order of the polynomial kernel (p)) were evaluated for the PKF and a range of gamma (γ) values for the RBF KF were evaluated. A summary of the classification accuracies for classifying the material groups for these ranges of values is shown in Table 4.3, with the best performing parameter configurations for each method highlighted in bold text and the worst performing highlighted in italic text.

It can be seen from Table 4.2 and Table 4.3 that the worst performing KF was RBF and the best performing KFs were the QKF and PKF. It can also be seen that in some cases the QP method failed to calculate the separating hyperplane and therefore a classification accuracy could not be calculated. It is evident that the best method for calculating the separating hyperplane for the QKF and PKF was SMO.

Table 4.2: Table comparing the SVM classification accuracies for a range of C values for the linear KF, quadratic KF and MLP KFs

Kernel Function	**Soft Margin Parameter (C)**	**Accuracy with SMO (%)**	**Accuracy with LS (%)**	**Accuracy with QP (%)**
LKF	0.01	67.62	70.00	*71.43*
LKF	0.10	75.71	75.24	79.05
LKF	1.00	78.57	77.62	**79.52**
QKF	0.01	**86.19**	**83.81**	-
QKF	0.10	77.14	76.67	-
QKF	1.00	77.14	70.00	-
LMPKF	0.01	37.62	57.14	-
LMPKF	0.10	46.67	28.10	-
LMPKF	1.00	*40.00*	*24.76*	-

Table 4.3: Table comparing the SVM classification accuracies for a range of C values for the LKF, PKF and LMPKF

Kernel Function	**Soft Margin Parameter (C)**	**p / γ Parameter**	**Accuracy with SMO (%)**	**Accuracy with LS (%)**	**Accuracy with QP (%)**
PKF	0.01	p=1	67.62	70.00	71.43
PKF	0.01	p=2	**86.19**	**83.81**	**85.71**
PKF	0.01	p=3	79.05	75.24	80.96
PKF	0.10	p=1	75.71	75.24	79.05
PKF	0.10	p=2	77.14	76.67	81.43
PKF	0.10	p=3	79.05	73.33	79.54
PKF	1.00	p=1	78.57	77.62	79.52
PKF	1.00	p=2	77.14	70.00	-
PKF	1.00	p=3	79.05	71.91	-
RBF	0.01	γ=0.01	*14.29*	*14.29*	*14.29*
RBF	0.01	γ=0.10	*14.29*	*14.29*	*14.29*
RBF	0.01	γ=1.00	61.43	63.81	63.81
RBF	0.10	γ=0.01	*14.29*	*14.29*	*14.29*
RBF	0.10	γ=0.10	*14.29*	*14.29*	*14.29*
RBF	0.10	γ=1.00	60.00	66.67	66.67
RBF	1.00	γ=0.01	*14.29*	*14.29*	*14.29*
RBF	1.00	γ=0.10	*14.29*	*14.29*	*14.29*
RBF	1.00	γ=1.00	62.86	63.33	63.33

A summary of the best performing configuration for each KF can be seen in Table 4.4. As outlined in Section 4.3.1, following evaluation of classification accuracies and run times, the best configuration for the SVM method is by using the PKF with a soft-margin value of 0.01 and a polynomial order of 2.

Table 4.4: Table comparing the SVM KF classification accuracies.

Kernel Function	**Best Performing Method**	**Optimised Parameters**	**Classification Accuracy**
Linear	QP	$C = 1.00$	79.524%
QKF	SMO	$C = 0.01$	**86.190%**
LMPKF	LS	$C = 0.01$	*57.143%*
Polynomial	SMO	$C = 0.01$ $p = 2.00$	**86.190%**
RBF	QP	$C = 0.10$ $\gamma = 1.00$	66.667%

It can be seen that the two best performing KFs with a classification rate of 86.19% are the QKF and the PKF. Although the two KFs performed equally well in terms of classification, the PKF was found to be marginally more efficient than the QKF at achieving the highest classification rate. The QKF took 0.49 seconds to train for one fold of data whereas the polynomial KF took 0.47 seconds. Therefore the PKF with a soft-margin value of 0.01 and a polynomial order of 2 was used in the SVM implemented in this approach.

This configuration of the SVM method with data collected from the press and slide actions was used for both experiments (group and individual classification) with the only difference being the number of classes (g) that the SVM had to classify. For the first experiment, i.e. classifying the materials into their six groups, $g = 6$ and for the second experiment involving 14 individual materials, $g = 14$ as described in Section 4.2.

4.3.2 Two-stage Support Vector Machine

In contrast to the one-stage approach described in Section 4.3.1, this section explains a two-stage approach to material classification. This approach utilises the multi-class SVM classification algorithm explained in Section 4.3.1 to firstly classify the materials into their groups and then uses this information to further classify the materials individually using a mixture of binary and multi-class SVM classification in the second stage.

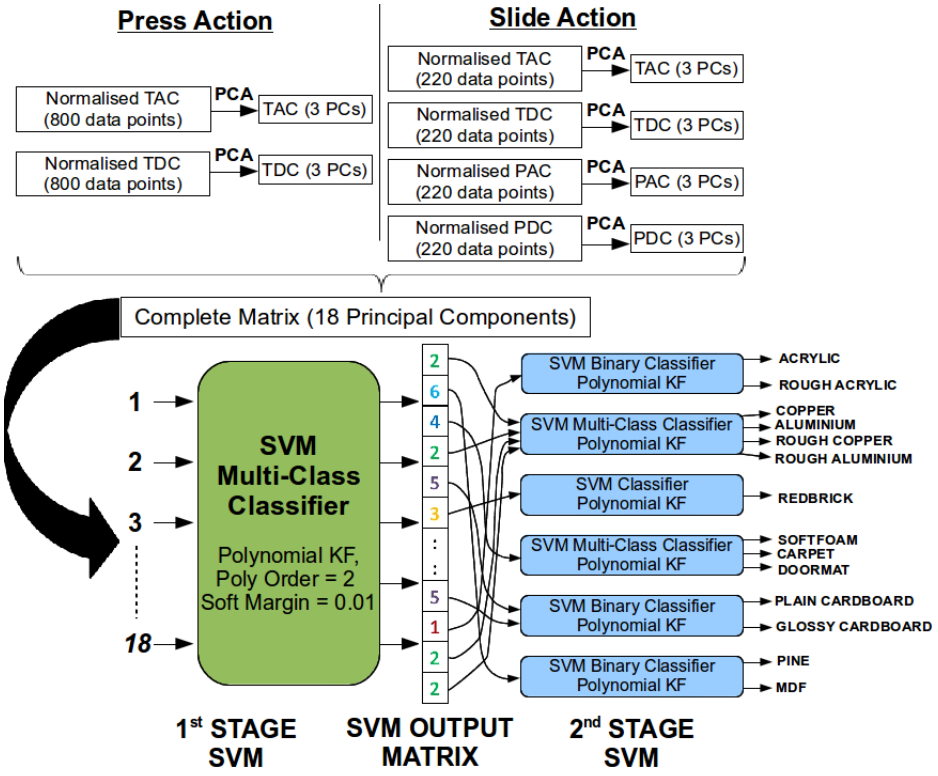

Figure 4.5: Diagram showing the two-Stage SVM approach used for material classification

The same SVM design as outlined in Section 4.3.1 is used in the first stage of this two-stage approach. For the second stage, 6 SVM algorithms are trained, one for each material group, some of which have different numbers of outputs/ groups for the individual materials within them, requiring the need for binary classification in some cases and multi-class classification in others. These SVM algorithms are saved and later used for testing the data input at the second stage. Similar to the development of the SVM in the one-stage approach, five different KFs with a range of parameters and hyperplane calculation methods were evaluated for the second stage SVM classification algorithm. The three equally best performing KFs in the second stage were the Quadratic KF, the Polynomial KF and the RBF KF, with the most efficient proving to be the Polynomial KF. Therefore the Polynomial KF was used in the second stage SVM.

Upon completion of material group classification in the first stage, the results of the classification are used as the inputs to the second stage. A model of the two-stage SVM approach can be seen in Figure 4.5. If a material is correctly classified into a specific group in the first stage then this activates the second SVM to classify the individual material within this material group. However, if the material group is incorrectly classified in the first stage then it is recorded

as an incorrect classification in the final output matrix and is not classified in the second stage to improve efficiency. Likewise, if the material is classified incorrectly in the second stage in comparison with the ground truth (i.e. it has been correctly classified in its group but incorrectly classified individually), then it is recorded as an incorrect classification in the output matrix.

4.3.3 One-stage Artificial Neural Networks

The ANN used is a back propagation ANN. In order to establish the best performing structure for an ANN for classifying materials individually and into groups, a range of number of hidden layers and training epochs were evaluated and it was empirically found that one hidden layer with 1500 training epochs provided the best trade off for performance versus speed. Furthermore, a range of number of hidden layer neurons was evaluated and a summary of the training accuracies of the best performing number of neurons in the hidden layer is shown in Table 4.5.

Table 4.5: Table comparing the training accuracies of different ANN structures.

No. of Neurons in Hidden Layer	**Average Training Accuracy (%)**
25	88.33
50	88.69
75	90.36
100	86.67

It is evident from Table 4.5 that the best performing structure for the ANN consisted of 75 neurons in the hidden layer. Therefore, this configuration of one hidden layer consisting of 75 neurons and training for 1500 epochs was used for the ANN classifier throughout all experiments. A model of the ANN is shown in Figure 4.6.

The same structure as shown in Figure 4.6 was used for both experiments with the only difference being the number of outputs (n). For the first experiment, $n = 6$ (six material groups) and for the second experiment $n = 14$ (fourteen individual test materials), as described in Section 4.2.

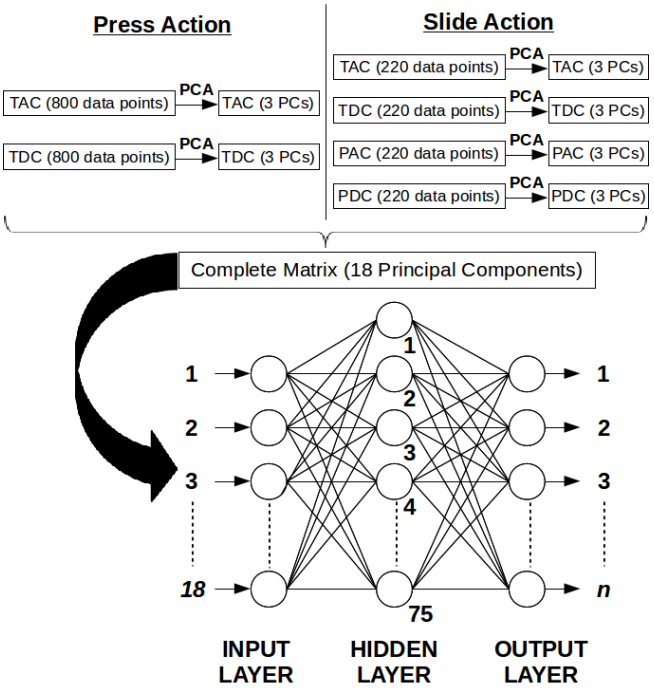

Figure 4.6: Diagram showing the ANN used for material classification

4.3.4 Two-stage Artificial Neural Networks

A two-stage ANN using a series of back propagation ANNs, each with one hidden layer, where the output of the first ANN is the input of the second to allow for group classification first followed by individual classification is also considered. The two-stage approach structure can be seen in Figure 4.7.

The ANNs used in the two-stage approach are similar in structure to the ANN used in the one-stage approach explained in Section 4.3.3. The first ANN is used to classify the materials into groups and the second stage of the ANN is comprised of six individual ANNs for each material group (i.e. plastic, metal, masonry, fabrics, paper and wood). These ANNs are all trained individually with their respective outputs relating to how many materials there are in each group, for example plastic has two outputs for the two plastic materials whereas metal had four outputs for the four metal materials in that group. After training, these networks are used for classifying the resulting output from the first ANN. In order to avoid identification of false positives, a threshold is set for testing the materials within the group. If the output of the neuron fired for the material sample being tested is not greater than 0.3 (1.0 being the maximum), then it is considered to be a failed classification.

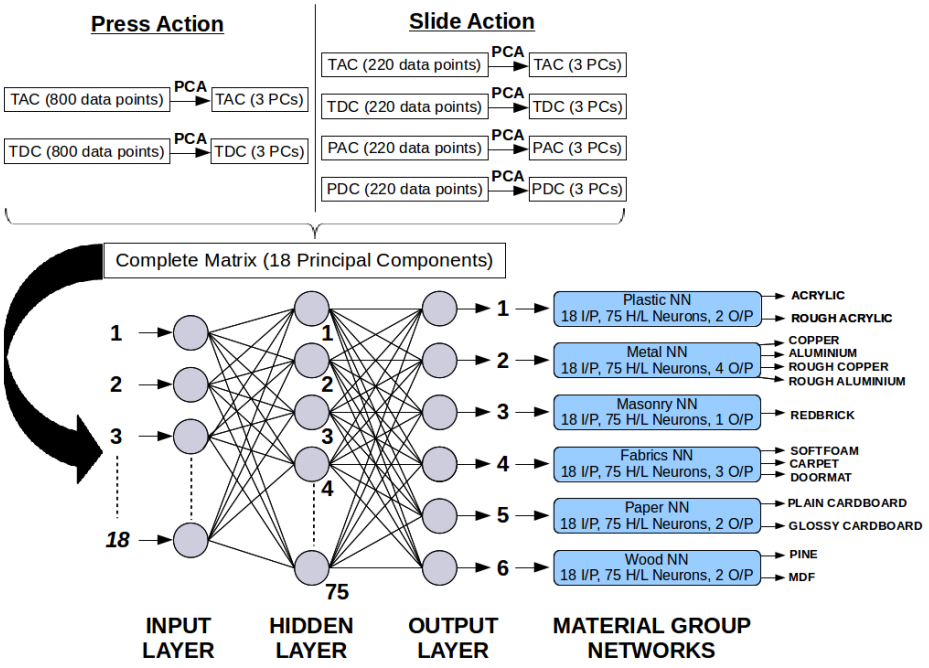

Figure 4.7: Diagram showing the two-stage ANN used for material classification

4.3.5 Support Vector Machine and Artificial Neural Networks hybrid algorithm

A hybrid approach was also developed comprising of a SVM classifier for material group classification and a separate ANN classifiers for the individual material classification. The structure of the hybrid algorithm can be seen in Figure 4.8.

A SVM classifier, as described in Section 4.3.2, is used first to classify the materials into their material group (i.e. using the polynomial KF with a polynomial order value of 2 and a soft margin value of 0.01). Then an output matrix is formed and the values in this matrix initiate the second stage of the hybrid approach with six ANNs for individual material classification within each of the material groups. The ANNs are constructed as described in Section 4.3.4 (i.e. with one hidden layer of 75 neurons and trained for 1500 epochs). As with the other two-stage approaches outlined in this section, in order to improve efficiency only materials correctly classified into their group are classified in the second stage.

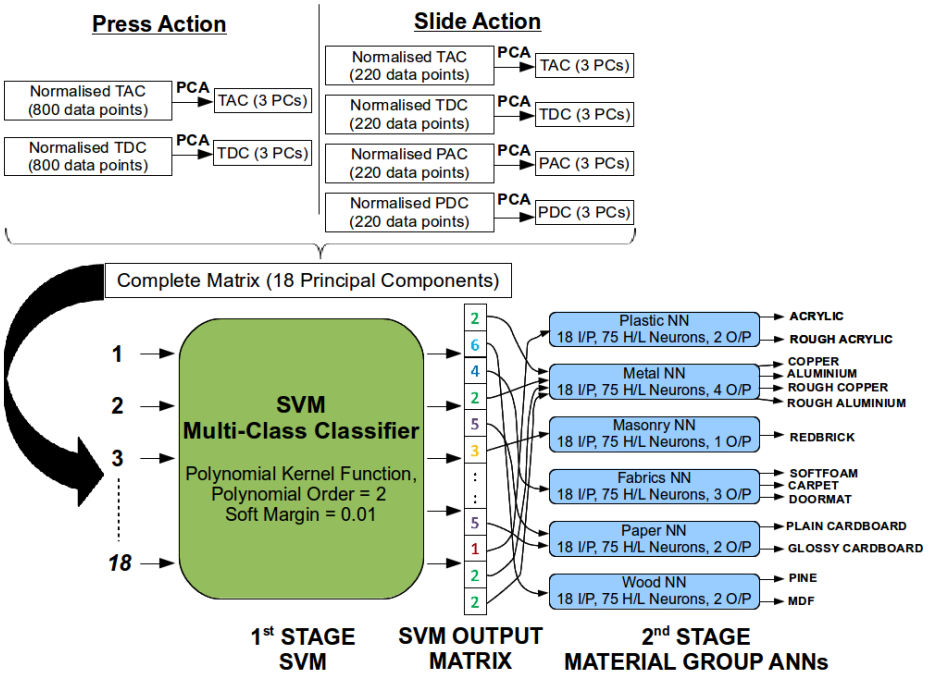

Figure 4.8: Diagram showing the SVM+ANN hybrid approach used for material classification

4.3.6 Other Classifiers Evaluated

Together with evaluating the performance of SVM, ANN and combinations of these classifiers other well known classifiers were also evaluated. The other classifiers evaluated and the configuration of these classifiers are outlined below:

- Gaussian Mixture Model: GMMs are calculated to represent each material (cluster centres are initialised randomly and the *k*-means algorithm is used for calculating convergence). The expectation maximisation (EM) algorithm is then used to calculate the maximum likelihood and the associated class label is selected. These classified labels are used to form an output matrix. As the cluster centres are initialised randomly 10 runs of each classification (i.e. material groups and individual materials) were completed and an average classification accuracy calculated.

- Linear Discriminant Analysis: In this work LDA is used for multi-class classification to identify materials individually and into their groups, although it can be used for binary or multi-class classification.

- Naïve Bayes: In this work NB is used firstly to classify materials individually and secondly classify them into their groups.

- *k*-Nearest Neighbour: In this work *k*-NN is used for multi-class classification of materials. A range of *k* values was tested to identify the most accurate number of neighbours to take into account for maximum classification accuracy. The *k* value that proved to be most effective for classifying the materials individually and into their groups was *k*=5.
- Multi-Layer Perceptron: Networks of varying complexity from 1-38 layers and 1-20 neurons in each layer, were evaluated in order to find the optimal structure for the MLP. The structure of the MLP used in this work to classify the materials into their groups and individually was a network consisting of 10 layers containing 19 neurons each.

4.4 Evaluation Results

In order to determine the best performing classifier for the material identification algorithm, analysis comparing the various classifiers was conducted. In addition, the best performing artificial algorithm was evaluated against human performance. The results of the evaluation of the aforementioned classifiers and their performance in comparison to human performance are presented in this section.

4.4.1 System Testing

A comparison of the results obtained for all of the classification algorithms presented and the average classification accuracies of the participants are shown in Table 4.6. As specified in Section 4.3, the results for the artificial algorithms are calculated by computing the average of the classification rates using 5-fold cross validation.

As shown in Table 4.6, SVM has outperformed the other approaches for both the classification of the materials into their groups and for classification of the individual materials. The two-stage SVM has proven capable of maintaining the group classification accuracy for the classification of the individual materials in its second stage. Considering that in three out of the six groups, the classification is binary and the most materials to classify between in the other groups is four, then it was possible for the SVM classifier to achieve such high classification accuracies in the second stage. Although it requires classifying the materials into groups initially and subsequently classifying them individually, using a

Table 4.6: Table comparing the material classification experimental results.

Modalities Utilised	**Run Time (to train one fold)**	**Material Group**	**Individual Materials**
Human Participants - Thermal Only	N/A	61.00%	50.90%
Human Participants - Thermal and Vibration	N/A	79.76%	69.64%
One-Stage ANN - Thermal Only	4.94secs	73.00%	60.90%
One-Stage ANN - Thermal and Vibration	5.47secs	83.81%	79.05%
Two-Stage ANN - Thermal and Vibration	7.66secs	83.81%	70.48%
One-Stage SVM - Thermal and Vibration	0.48secs	86.19%	72.38%
Two-Stage SVM - Thermal and Vibration	0.55secs	86.19%	86.19%
Hybrid SVM and ANN - Thermal and Vibration	2.66secs	86.19%	82.86%
GMM - Thermal and Vibration	13.35secs	86.14%	80.24%
LDA - Thermal and Vibration	1.52secs	78.57%	80.95%
NB - Thermal and Vibration	1.68secs	71.43%	80.95%
k-NN - Thermal and Vibration	0.95secs	71.43%	64.29%
MLP - Thermal and Vibration	5.45secs	71.43%	66.67%

two-stage approach provides an increase in classification accuracy of individual materials.

The second best performing algorithm is the SVM and ANN hybrid approach. The SVM and ANN hybrid approach using the polynomial KF achieved 82.86% accuracy. The GMM approach was also a highly performing classifier with 86.14% for material groups and 80.24% for individual materials. However, it can be seen in Table 4.6 that aside from the fact that it achieved slightly less accuracy in comparison with the two-stage SVM algorithm, like the other algorithms, the GMM algorithm also takes significantly longer to train (taking 13.35 seconds to train for one fold of data) than the SVM algorithm (taking 0.48 seconds to train for one fold of data). Interestingly the LDA and NB classifiers both performed better when classifying the materials individually rather than into their groups. This is contrary to what was expected as there are 14 outputs when classifying into individual materials compared with only 6 outputs for group classification. As a consequence, LDA and NB both performed marginally better than GMM for classifying the individual materials with 80.95% accuracy, but performed poorer than GMM however for the classification of material groups with 78.57% accuracy for LDA and 71.43% accuracy for NB. k-NN was found to perform optimally when $k = 5$ with a fast training time of 0.95 seconds for one node, however in comparison with the other classifiers it is still lacking in accuracy for classifying materials individually and into their groups. MLP was found to be relatively slow to train and was out performed by the majority of the other classifiers. The training times presented are based on training one fold of data for each classifier and the training was completed in Matlab on a desktop PC with an Intel® Xeon® CPU E5-16070 @ 3.00GHz x 4 processor and 16Gb of RAM. Therefore it is concluded that the two-stage SVM algorithm is the best performing and most efficient algorithm for the task of material classification.

4.4.2 Evaluation of Human Performance

The study participants consisted of 12 healthy humans, two female and ten male, all aged between 23-56 years and all participants used their preferred hand. It was determined that ethical approval was not required for these experiments as no data was collected from or about the participants other than age and sex. Each of the materials was enclosed in a box, out of sight of the participants, during the entire experiment, in order to ensure that the participants were classifying between the materials based on tactile sensing alone (to compare

fairly with the artificial system experiment). The participants were informed about what each material is during the training phase. Then the materials were presented to the participants again in a random order and the participants were required to identify each material. They could select a material more than once or state that they couldn't identify it and therefore give a null response. One testing phase per participant was completed, allowing for both the slide and press actions. Before the experiment commenced, the participants were given clear instructions on how to make contact with the material. For the press experiment, they were instructed:

1. to press down on the material with their index finger,
2. to leave it on the material for a maximum of 20 seconds (similar to the artificial fingertip),
3. to lift their finger away from the material,
4. that it was prohibited to move their finger laterally or slide/ rotate their finger at any time when in contact with the material.

For the slide experiment they were instructed to:

1. reapply their finger to the material,
2. slide their fingertip along the material for a distance of 10cm,
3. lift their finger away from the material.

The 14 materials were presented to the participants one by one. In the first experiment, the results from the participants were analysed to determine the humans' ability to classify the material groups. In the second experiment, the results were analysed to determine the humans' ability to classify the individual materials. In terms of analysis, if a participant selected the correct group (regardless of whether it was the correct particular material or not) in the first experiment then one point was awarded for group classification. For each individual material that the participant correctly identified in the second experiment, one point was awarded for individual material classification. A percentage accuracy was calculated for human classification of material groups and individual materials with the maximum each participant could score in the two experiments being six points and fourteen points respectively. A breakdown of the results of the human evaluations for each material can be

seen in Table 4.7. The second column shows the accuracies of participants successfully identifying the materials from a press action alone and therefore sensing thermal properties only. The third column shows the accuracies of the participants identifying the test materials from using both the press and slide action therefore utilising both thermal properties and surface texture.

Table 4.7: The percentages accuracies for each material from the human evaluation experiments.

Material	**Identified Percentage - Thermal Only**	**Identified Percentage - Thermal and Vibration**
Acrylic	40.00%	100.00%
Copper	40.00%	58.33%
Redbrick	20.00%	58.33%
Soft Foam	100.00%	100.00%
Pine	30.00%	41.67%
Carpet	100.00%	100.00%
MDF	40.00%	50.00%
Glossy Cardboard	20.00%	66.67%
Plain Cardboard	30.00%	83.33%
Doormat	100.00%	100.00%
Aluminium	60.00%	58.33%
Rough Copper	-	41.67%
Rough Aluminium	-	58.33%
Rough Acrylic	-	75.00%
Average	53.00%	70.83%

Table 4.7 shows that every participant achieved 100% identification of the soft foam, the carpet and the doormat when considering thermal properties only and when using thermal and surface texture properties. It also shows that 100% of participants were able to correctly identify the smooth acrylic when using thermal and surface texture properties in comparison with only 40% of the participants correctly identifying it when considering thermal properties only. Indeed, in comparison to when the participants were sensing thermal

properties only, the identification accuracies for all of the individual materials, except aluminium, either increased or stayed at a maximum when the vibration (i.e. texture) analysis was permitted. This clearly shows that exploration of the texture, via the sliding action, plays a vital part in the identification of materials, and indeed is a critical characteristic that humans use to identify materials. The results in Table 4.7 also show that pine and rough copper were the most difficult materials for the participants to identify.

4.5 Discussion

Initially, the participants were evaluated for identification of material groups. It is found that the average accuracy was 79.76%. Secondly, the participants were evaluated for identification of individual materials and it is found that the participants achieved an average accuracy of 69.64%. It can be seen from Table 4.6 that all of the classification algorithms presented have outperformed the participants (when performance is averaged across all test materials). However, the best performing artificial algorithm consists of data reduction by using Eigen-decomposition based PCA to produce PCs as inputs to the best performing classification algorithm, i.e. the two-stage SVM. This configuration is the algorithm that is evaluated against the human performance for the remainder of this discussion. The artificial algorithm outperformed the participants by over 6% for material group classification and by over 16% for individual material classification. This is due to the fact that it is easier for a human to determine what group a material would belong to (i.e. identify that the material is definitely metal) than it is for them to identify a specific material within that group (i.e. is it copper or aluminium). It can be seen from the confusion matrix in Figure 4.9(a) and 4.9(b) that both the artificial algorithm and the participants successfully classified the soft foam in every instance and did not get it confused with any other material. It can also be seen from Figure 4.9(a) that where the artificial algorithm classified the pine material correctly on 60% of the instances, the highest misclassification was with MDF, another material with similar properties and in the same material group. Likewise, for classifying MDF, the largest misclassification was with pine. This misclassification can also be witnessed as a common misclassification amongst the participants as only 50% of the participants correctly classified MDF. Furthermore, in almost 42% of the instances the participants misclassified MDF as pine as shown in Figure 4.9(b). It is shown in Figure 4.9(a) that a common misclassification of the

artificial algorithm was a confusion between acrylic and glossy cardboard, with glossy cardboard being classified correctly for 40% of the instances however in just over 33% of the instances it was misclassified as another material with similar texture and thermal conductivity properties: acrylic.

Interestingly, the participants struggled with the identification of the rough materials, with only 2 out of 12 being able to identify all three rough materials. For example, one of the most challenging materials for humans to identify was the rough copper, and interestingly it was commonly misclassified as redbrick, as shown in Figure 4.9(b). This is due to the fact that the redbrick is perceived as cold and rough by the participants, in a similar manner to how metals are perceived. Therefore this is one of the instances where the artificial algorithm outperforms the participants as the algorithm can analyse thermal conductivity much more accurately than the participants and therefore not misclassify it as a masonry material. This is shown in Figure 4.9(a) where the artificial algorithm classifies the rough copper in just over 93% of the instances with the only misclassification being with another rough metal: aluminium. This misclassification is also evident when classifying the materials into their groups, as shown in Figure 4.10(a) and 4.10(b). The artificial algorithm outperforms the participants when classifying materials in both metal and masonry groups. The majority of instances of misclassification for the participants when classifying masonry objects is confusing them with a metal object, as both are perceived as cold.

It is evident from the results that the introduction of tactile texture analysis via vibration has increased the accuracy of classifying materials for the participants and particularly when identifying the material groups. It should be noted that due to the nature of some materials, humans can intuitively take other characteristics into account, for example compressibility (i.e. soft foam is much more compressible than the other materials). The artificial algorithm was trained to analyse only the thermal properties and surface texture of the material and not compressibility. This may have given the human participants a slight advantage in identifying some materials. This is evident when comparing the accuracy of the artificial algorithm for classifying fabrics as a material group (80%) with the accuracy of the participants (100%), as shown in Figure 4.10(a) and 4.10(b). The participants have no misclassification of the fabrics when identifying their material group. It can be assumed that this is due to the participants being able to identify the compressibility of the objects like soft foam and carpet whereas the artificial algorithm was not trained to analyse

	Ac	Cr	R	S	P	Ct	M	GC	PC	D	Al	CrR	AlR	AcR
Ac	60.0	0.0	0.0	0.0	0.0	0.0	0.0	20.0	6.7	0.0	0.0	0.0	13.3	0.0
Cr	0.0	100.0	0.0	0.0	0.0	0.0	0.0	0.0	0.0	0.0	0.0	0.0	0.0	0.0
R	0.0	0.0	66.7	0.0	20.0	0.0	6.7	6.7	0.0	0.0	0.0	0.0	0.0	0.0
S	0.0	0.0	0.0	100.0	0.0	0.0	0.0	0.0	0.0	0.0	0.0	0.0	0.0	0.0
P	0.0	0.0	13.3	0.0	60.0	0.0	20.0	6.7	0.0	0.0	0.0	0.0	0.0	0.0
Ct	0.0	0.0	0.0	0.0	0.0	80.0	0.0	6.7	6.7	0.0	0.0	0.0	6.7	0.0
M	6.7	0.0	0.0	0.0	20.0	0.0	73.3	0.0	0.0	0.0	0.0	0.0	0.0	0.0
GC	33.3	0.0	0.0	0.0	13.3	0.0	0.0	40.0	0.0	0.0	0.0	0.0	13.3	0.0
PC	6.7	0.0	0.0	0.0	0.0	6.7	0.0	6.7	73.3	0.0	0.0	0.0	6.7	0.0
D	6.7	0.0	20.0	0.0	6.7	0.0	0.0	0.0	6.7	53.3	0.0	0.0	6.7	0.0
Al	0.0	13.3	0.0	0.0	0.0	0.0	0.0	0.0	0.0	0.0	80.0	0.0	6.7	0.0
CrR	0.0	0.0	0.0	0.0	0.0	0.0	0.0	0.0	0.0	0.0	0.0	93.3	6.7	0.0
AlR	13.3	0.0	0.0	0.0	0.0	0.0	0.0	6.7	0.0	6.7	6.7	0.0	66.7	0.0
AcR	6.7	0.0	0.0	0.0	0.0	0.0	0.0	13.3	0.0	0.0	0.0	0.0	13.3	66.7

(a)

	Ac	Cr	R	S	P	Ct	M	GC	PC	D	Al	CrR	AlR	AcR
Ac	100.0	0.0	0.0	0.0	0.0	0.0	0.0	0.0	0.0	0.0	0.0	0.0	0.0	0.0
Cr	0.0	58.3	0.0	0.0	0.0	0.0	0.0	16.7	0.0	0.0	25.0	0.0	0.0	0.0
R	0.0	0.0	58.3	0.0	8.3	0.0	0.0	0.0	8.3	0.0	0.0	8.3	0.0	16.7
S	0.0	0.0	0.0	100.0	0.0	0.0	0.0	0.0	0.0	0.0	0.0	0.0	0.0	0.0
P	8.3	0.0	0.0	0.0	41.7	0.0	25.0	8.3	0.0	0.0	16.7	0.0	0.0	0.0
Ct	0.0	0.0	0.0	0.0	0.0	100.0	0.0	0.0	0.0	0.0	0.0	0.0	0.0	0.0
M	0.0	8.3	0.0	0.0	41.7	0.0	50.0	0.0	0.0	0.0	0.0	0.0	0.0	0.0
GC	16.7	8.3	0.0	0.0	0.0	0.0	8.3	66.7	0.0	0.0	0.0	0.0	0.0	0.0
PC	0.0	0.0	0.0	0.0	0.0	0.0	8.3	0.0	83.3	0.0	0.0	0.0	8.3	0.0
D	0.0	0.0	0.0	0.0	0.0	0.0	0.0	0.0	0.0	100.0	0.0	0.0	0.0	0.0
Al	8.3	8.3	8.3	0.0	16.7	0.0	0.0	0.0	0.0	0.0	58.3	0.0	0.0	0.0
CrR	0.0	0.0	25.0	0.0	0.0	0.0	0.0	0.0	0.0	0.0	0.0	41.7	16.7	16.7
AlR	0.0	0.0	8.3	0.0	0.0	0.0	8.3	0.0	0.0	0.0	0.0	25.0	41.7	16.7
AcR	0.0	0.0	0.0	0.0	0.0	0.0	0.0	0.0	0.0	0.0	0.0	25.0	0.0	75.0

(b)

Figure 4.9: a) Confusion matrix showing the percentage accuracy of the artificial algorithm (using one-stage SVM) for classifying all the materials individually; b) Confusion matrix showing the percentage accuracy of the human participants for classifying all the materials individually.

	P	Me	Ma	C	F	W
P	90.0	0.0	0.0	3.3	3.3	3.3
Me	0.0	100.0	0.0	0.0	0.0	0.0
Ma	0.0	0.0	73.3	6.7	0.0	20.0
C	13.3	0.0	0.0	76.7	6.7	3.3
F	0.0	0.0	4.4	4.4	80.0	11.1
W	0.0	0.0	10.0	10.0	0.0	80.0

(a)

	P	Me	Ma	C	F	W
P	87.5	12.5	0.0	0.0	0.0	0.0
Me	10.4	68.8	10.4	4.2	0.0	6.3
Ma	8.3	16.7	58.3	8.3	0.0	8.3
C	8.3	8.3	0.0	75.0	0.0	8.3
F	0.0	0.0	0.0	0.0	100.0	0.0
W	4.2	12.5	0.0	4.2	0.0	79.2

(b)

Figure 4.10: a) Confusion matrix showing the percentage accuracy of the artificial algorithm (using two-stage SVM) for classifying all the materials into groups; b) Confusion matrix showing the percentage accuracy of the human participants for classifying all the materials into groups.

this modality. However, even though the artificial algorithm did not utilise a key modality for humans, namely compressibility, overall it still outperformed humans.

4.6 Conclusion and Future Work

A range of classifiers and combinations of classifiers that were implemented, tuned and evaluated for the classification of materials into their respective groups and the classification of individual materials has been presented in this chapter. This classification was based on a combination of the thermal and surface texture properties of the materials. It is proven that a two-stage SVM approach performs best and is the most efficient method in completing the material classification task. Performance evaluation has been conducted using human participants and, although the machine-based algorithm is slower than humans at classification due to training requirements, it was found that the average performance of all biologically-inspired learning algorithms across all test materials exceeded that of the participants' average performance. The two-stage SVM approach outperformed humans by over 16% accuracy in material identification.

The success of the challenging task of material identification presented in this chapter proved invaluable in providing familiarity with the use of the BioTAC fingertip and the analysis of the data it presents. Whilst getting familiar with the sensitivity and accuracy of the BioTAC, it became apparent that because of its high sensitivity, it may be capable of measuring biomedical parameters, namely human vital signs such as a human pulse. Therefore, this directed the remainder of the research in this thesis towards the automated collection and analysis of human vital signs based on tactile perceptions.

CHAPTER

FIVE

Human Pulse and Respiratory Signal Analysis

5.1 Introduction

Being able to accurately and quickly assess a person's condition in an emergency or search and rescue situation could, in critical scenarios, mean the difference between life and death. Two key indicators of human health are pulse and respiratory rate. The pulse can be measured from numerous points around the human body, for example, from the finger artery, the brachial artery on the inside of the upper arm, the posterior tibial at the ankle, the carotid artery at the neck or the radial artery at the wrist. The heart pulse rate is the speed of the heart measured in Beats Per Minute (BPM). Although heart rate can vary depending on one's age, physical size and activity, amongst other factors, it is considered that a normal pulse (heart rate) for a resting adult ranges from 60-100BPM. A rate slower than 60BPM is defined as bradycardic and a rate higher than 100BPM is described as tachycardic. However, it is not solely how many BPM that the heart makes which determines the health of a person's heart as the rhythm of their heart beats must also be considered. With a heart rate of 60-100BPM and a regular rhythm of beats, an adult is considered to have a normal heart rate and be in sinus rhythm (i.e. have a healthy heart rate). However, an individual may have a normal pulse (heart rate) of 60-100BPM but may have an irregular rhythm of beats. When the heart is not beating in a consistent pattern, it is referred to as arrhythmia. It is also possible for an individual to have a regularly-irregular form of arrhythmia; for example if their heart is not beating at regular intervals but it is consistently following an incorrect pattern, this is classed as sinus arrhythmia. Likewise, it is possible

for an individual with bradycardia or tachycardia to still be in sinus rhythm, i.e. their pulse is outside of the normal rate of 60-100BPM, however it has got a healthy rhythm. Arrhythmia and/ or irregularities in the aforementioned measurements of blood flow can sometimes indicate disease. To read and analyse the pulse can require high levels of skill and experience from medical personnel.

Measuring Respiratory Rate (RR) requires counting how many times the chest rises in one minute. This is a difficult procedure as it is often completed visually and if the person is breathing weakly or visibility is poor, it may be difficult to distinguish movement in the chest (particularly through clothing) and therefore requires skilled medical personnel. It is estimated that a healthy adult should breath 12-20 times per minute when at rest (Barrett et al., 2010). This chapter presents novel algorithms that will equip a robot with the necessary skills to assess a human's BPM and RR. Algorithms that calculate heart BPM, Pulse to Pulse Interval (PPI), RR and Breath to Breath Interval (BBI) are presented. The aim of this work is provide a "first response" service to an elderly or disabled user in a home assist scenario, or to determine a human's health status in an emergency rescue scenario before risking further human life.

The BPM is used to classify if a heart rate is normal, bradycardic, or tachycardic. PPI is used to determine if the pulse rate is regular or in a form of arrhythmia. The RR and BBI are used to determine if the human's breathing is normal and regular. The results in this chapter show that pulse and breathing can be successfully measured and a participant's BPM and RR calculated using trough and peak detection methods respectively. Furthermore, the robotic system proved to be capable of classifying the pulse as being regular or arrhythmic and the RR as being regular or irregular.

5.1.1 Assessing Human Vital Signs

There are numerous key vital signs that can be measured from a human in order to ascertain their current health status. Some require more equipment and time than others but may provide more detail; for example a complete 12-lead electrocardiogram (ECG) requires the connection of electrodes on the patient's limbs and the surface of the chest in order to measure the heart's electrical potential over a period of time, usually 10 seconds. Although this procedure would not be suitable for first response or in a disaster zone, it does provide a trained clinician with a large amount of information about the

function of the heart's electrical conduction system along with heart rate and rhythm (Walraven, 2011). Assistive technologies have been developed to help with the nursing of elderly care, particularly with the manual handling aspect of moving patients etc. (Hu et al., 2011) or to enable a doctor to carry out basic remote assessments of a patient's health (Stollnberger et al., 2016). However, in order to complete an accurate assessment of a patient or victim's vital signs it is reported that these systems need much more advanced tactile sensing capabilities (Stollnberger et al., 2016). Key vital signs that can be assessed outside of a medical practice, hospital or home and what they indicate are discussed below:

- Heart/ Pulse Rate (measured in Beats Per Minute (BPM)): A key indicator of a patient's clinical condition. Tachycardia (greater than 100 BPM) may be indicative of circulatory compromise due to cardiac failure, volume depletion or sepsis, pyrexia, metabolic disturbance, cardiac arrhythmia or pain and general distress. Bradycardia (less than 60 BPM) can be more difficult to identify as it could be normal with physical conditioning, or as a consequence of medication. However, it may also be an important indicator of hypothermia, hypothyroidism, Central Nervous System (CNS) depression or heart block (Royal College of Physicians of London, 2012).

- Respiratory Rate (RR): the number of breaths taken by a person in one minute. This is one of the key indicators of current health status. An elevated RR is a powerful sign of acute illness, distress, generalised pain, sepsis remote from the lungs, CNS disturbance and metabolic disturbances such as metabolic acidosis. A reduced RR is an important indicator of CNS depression and narcosis (Royal College of Physicians of London, 2012).

- Capillary Refill Time (CRT): the time taken for the colour to restore in an external capillary bed following blanching caused by pressure being applied. The Capillary Refill Time (CRT) can be measured by pressing on the fingernails, the soft tissue at the kneecap or forearm, the centre of the chest or the forehead (Beckow, 2005). The forehead is usually the most accessible area to press in a disaster zone considering the victims will most likely be wearing clothes. When measured at the forehead, the normal time for CRT should be less than 2 seconds for an adult or up to 3 seconds for an infant (Strozik et al., 1997). A prolonged capillary refill time may be a sign of shock, can indicate dehydration, decreased

peripheral perfusion or that the blood supply has been cut off from the skin.

There has been much work on the design and development of wearable sensors that are capable of monitoring vital signs. For example, Mouradian et al. (2014) presents a wearable photoplethysmography (PPG) sensor that enables continuous monitoring of vital signs such as oxygen saturation, RR, heart rate and blood pressure. The small wearable device enables users to store all the measured data and send it to a remote location. He et al. (2015) developed a different style of wearable sensor in the form of in-ear sensors which measure the ballistocardiogram (BCG) (a measure of ballistic forces on the heart), ECG and PPG (a volumetric measurement of an organ) in order to measure and monitor stroke volume (SV), pulse transit time (PTT), pre-ejection period (PEP) and cardiac output (CO). There have also been efforts to include the wearable sensors within fabric so that the user is not disturbed or inconvenienced in any way by wearing a sensor and also to help a user not forget to put the sensors on (Mahfouz et al., 2011). For example, Gagarin et al. (2014) present a sensor that incorporates their previously designed microwave stethoscope (Gagarin et al., 2012), capable of reading of heart beat, RR, SV and changes in lung water contents. However, the sensors faced numerous problems during testing such as intermittent skin contact, making it difficult to accurately monitor the aforementioned vital signs continuously. Another sensor aimed at being integrated into a standard shirt was presented by Ramos-Garcia et al. (2016). Accuracies of within 1 breath per 10 seconds period was achieved and showed that the sensor could potentially be used as a means of continuously monitoring a person's RR. Someya (2013) also focuses on a wearable sensor with the aim that the user would not be constricted in any way whilst wearing it. The authors are working on a "bionic skin" type wearable sensor that sits on top of skin and will eventually be capable of continuously monitoring vital signs. However, all of these styles of sensors require the users to be wearing them in order for their vital signs to be assessed. These would not be helpful in an emergency or disaster zone as most people do not currently wear any form of health monitoring equipment on a daily basis and certainly not sensors that are connected back to a monitored database. Therefore, one could not depend on wearable sensors as a means of assessing, for example, the current health status of a trapped, unconscious person.

It is evident from a thorough review of the literature regarding non-invasive and non-wearable sensors, that the two most common vital signs measured by

these styles of sensors are BPM and RR. The most common method used for the measurement of these two vital signs is the Doppler effect. Using microwaves and Radio Frequency (RF) to detect small movements such as heartbeat and respiration dates back to the 1970's (Lin, 1975). Gu and Li (2014) explain how the moving of the chest wall causes a Doppler shift and by analysing the phase information in the received radar signals it is possible to determine the RR and BPM. This approach to measurement of RR and BPM has been heavily researched by many research groups, e.g (Choi and Kim, 2009; Lu et al., 2011; Iyer et al., 2013; Boothby et al., 2013) since the initial work by Lin (1975). The majority of radar-based methods can have inaccuracies, particularly in the measurement of the heart rate due to several spurious peaks being produced at harmonics and intermodulation frequencies (Ren et al., 2015). In order to reduce these errors, Ren et al. (2015) apply a signal processing algorithm, based on the state-space method, to the data collected from a human participant using a Stepped Frequency Continuous Wave (STCW) radar in order to extract the cardiac and respiration rates. Accuracies of over 98% for heart rate in static mode and 94% in motion were obtained without producing spurious peaks, although tests were carried out on just one participant. More recently, Kuo et al. (2016) extended their previous work (Kuo et al., 2015) to develop a 60-GHz complementary metal-oxide semiconductor (CMOS) direct-conversion Doppler radar RF sensor with a clutter canceller non-contact vital signs detection system using a single antenna. The clutter canceller which consisted of a Video Graphics Array (VGA) and a 360° phase shifter was reported to greatly increase sensitivity when detecting weaker human heartbeats and breaths. The vital signs could be read from a human up to 75cm away and the sensor was on a $2 \times 2mm$ chip which could eventually be installed onto a mobile robot for use in disaster zones. Although sensors utilising the Doppler effect are heavily researched and their accuracies for detecting human vitals are continuously improving, they would face difficulties when in disaster zones as any other movement within the area would undoubtedly cause numerous artefacts in the signals received.

Another very popular method for measuring vital signs, particularly heart rate, is via camera equipment and image processing techniques. Tasli et al. (2014) use a standard off-the-shelf video camera to implement a remote PPG based technique where variations in the colour of human skin were analysed for observing average heart rate. It was found that although acceptable accuracies were achieved in heart rates measured between 50-90 BPM, anything higher than this tended to be underestimated. Additionally, it was found that changes

in lighting dramatically affected the effectiveness of the method and that the success of this method requires training on a ground truth dataset of personal skin colour which may not always be available. Wu et al. (2012) also use a standard video camera and apply their "Eulerian Video magnification" technique to the video sequence. The authors record a video sequence of a human face and apply their magnification algorithm which applies spatial decomposition and temporal filtering to each of the frames. They then amplify the resulting signal to reveal blood filling and leaving the skin which is not visible to the naked eye. Although a useful method to visualise and analyse human heart rate, this method struggles under changes in ambient lighting. Tran et al. (2015) present a robust real time method that addresses issues relating to challenging environments for vision based heart rate measurements such as low illumination, movement of participants and complicated facial models that include beards and moustaches etc. The proposed method applies a combination of face detection/ tracking and skin detection algorithms and the application of a finite state machine to reduce noise and construct a series of red, green, blue (RGB) images. The method is reported to perform well and is suggested for use in remote health care monitoring, however it would require further evaluation for extreme conditions such as disaster zones. In contrast to using a standard camera, Gault and Farag (2013) use video frames from a thermal imaging camera to calculate heart rate from vascular mapping, blood perfusion and wavelet analysis. Various locations from the images, e.g. forehead, cheeks, chin etc., were evaluated for heart rate detection and accuracies of $> 85\%$ were found when analysing the forehead region. However, like the other vision based heart rate measurement algorithms presented, this method may struggle in uncontrolled environments due to changes in ambient temperatures etc. It is evident that vision based methods for heart rate measurements are highly accurate when good quality vision data are available but other sensors such as sound and tactile sensors are required for use in areas where vision is very poor. The use of these alternative sensing modalities will enable collection of data that vision systems will not be able to measure, such as vibration and thermal data from physical contact.

Another sensor that has been used to measure a heartbeat and RR is an optical interferometer. This is a sensitive device which detects physical changes in the optical fibre length. Šprager et al. (2010) use an optical fibre interferometer placed in a mattress to continuously measure a person's vital signs overnight. A third-order low bandpass filter was applied to the data collected from the sensor and further bandpass filters ranging in cut-off frequencies were used

to detect BPM and RR. Accuracies of approximately 95.7% for heartbeat and 93.8% for respiration were achieved across datasets consisting of 5 males for 60 seconds of data collection. The authors continued this research in later work to test the method on a user during a full night's sleep of 9.75 hours (Šprager et al., 2012). Although higher accuracies of 97.76$\pm$1.04% for heart rate were achieved, these sensors are extremely sensitive and must be used in an embedded environment. Therefore, although they are useful for applications such as overnight monitoring of a patient's vital signs, they would not be useful for measuring vital signs in emergency or disaster zones.

Interestingly, to date force or tactile sensing has not been heavily researched for measurement of human vital signs. Mi and Nakazawa (2014) present a thin multi-point polymer force/pressure sensor that they developed for pulse measurement from the radial artery on the wrist. The sensor is extremely thin measuring just 100 µm and contains 25 sensing electrodes on a charged cellular polymer layer. The authors placed the sensor on the wrist of a human and visually assessed the detection of pulses against a physician's diagnosis in real time and reported that there was a strong correlation meaning the sensor is capable of sensing a heartbeat. Qian et al. (2011) also develop a tactile sensor for measuring pulse from indirect contact with an artery. The sensor is a tactile array consisting of six pieces of Polyvinylidene Fluoride (PVDF) films and is evaluated using a person's wrist, demonstrating effective measurement of pulse from the radial artery. A highly sensitive tunnelling piezoresistive tactile sensor was developed by Chang et al. (2016) for continuous blood pulse wave monitoring. The sensor proved effective at measuring pulse from a human's wrist. The work presented in the literature for tactile sensing focuses mainly on the development of application specific sensors in pulse measurement, however there is little research on using a multi-modal tactile sensor for pulse measurement on a triage robot. The work outlined in this thesis aims to utilise a commercial tactile sensor for pulse measurement and analysis by considering the time between pulses (PPI).

Capillary Refill Time (CRT) is a critical clinical indicator of trauma and detection, however digitised CRT techniques are not readily available or researched (Karlen et al., 2011). CRT is normally assessed by visual inspection at certain points around the body for example the chest, fingertip or forehead by a trained clinician; however, this method is prone to high inter-observer variability (Otieno et al., 2004). Karlen et al. (2011) aim to address this variability by standardising the pressure placed on the finger when using a small portable

device to assess CRT by analysing PPG recordings. They assess the use of their standardised rules on a paediatric dataset to validate 93 readings from fingertips and reliably detected invalid CRT readings, with a sensitivity rate of 98.4%. Invalid readings are caused by numerous issues such as low perfusion signals, insufficient pressure, and artefacts. Although a promising step towards a reliable digital method to validate CRT measurements, it is not capable of directly measuring CRT and requires the use of other algorithms. All of the methods discussed in this section measure BPM, RR or both and one method takes a step towards the measurement of CRT. However, algorithms for use with a tactile sensor that are capable of measuring all three of these vital signs, particularly in areas of poor lighting or visibility, are not available to date. The work in this chapter and in Chapter 6 provides such algorithms.

5.2 Methodology

The five fingered Shadow Hand, made by the Shadow Robot Company, equipped with three BioTAC^{TM} sensors from Syntouch® was used to collect pulse and respiratory data from a human. The Shadow Hand has 21 degrees of freedom and has similar dexterity to a human hand, allowing it to mimic to some extent the actions required to take one's pulse from their wrist and sense movement in their chest. Figure 5.1 shows an image of the Shadow Hand equipped with three BioTAC sensors.

As outlined in Chapter 2, the BioTAC is a tactile sensor which is shaped like a human fingertip and is liquid filled, giving it similar compliance to a human fingertip. It measures force applied across an array of 19 electrodes, absolute fluid pressure (PDC), dynamic fluid pressure (PAC), static temperature (TDC) and thermal flow (TAC). Figure 2.10 showed a cross section view of the BioTAC fingertip. The data source used for the pulse reading is vibration (as is used by a human when reading another's pulse) rather than light or electrical data which are used in the majority of other pulse reading technologies with the most common being through the use of photoplethysmography (PPG) (Allen, 2007). Experiments for measuring respiratory rate along with pulse rate are carried out. The data sources used for measuring breaths are vibration and thermal conductivity, used concurrently to ensure algorithm robustness. In the case of pulse measurement, contact with a human wrist allows for sensing vibration caused by blood flow through the radial artery and contact with the chest allows for sensing vibration signals caused by the lungs inhaling and

Figure 5.1: Image of The Shadow Hand with three mounted BioTAC Fingertip Tactile Sensors

releasing air when breathing. In all cases, this work uses a lowpass filter as a first stage of noise reduction of the data and utilises wavelet algorithms as a second stage of smoothing, thus improving the overall noise reduction in the pulse and respiratory rate waveforms. A further smoothing algorithm based on lateral inhibition is also evaluated in this chapter.

5.2.1 Data Collection

For data collection in the experimental work carried out in this chapter and Chapter 6, three BioTAC sensors were installed on to the first finger (FF), middle finger (MF) and thumb (TH) of a five fingered Shadow Dexterous Hand^{TM}from the Shadow Robot Company (2017) upgrading from the standard single point force Pressure Sensor Tactiles (PST) sensors that are fitted as standard to the fingertips of the Shadow Hand.

Pulse and RR data were collected from 12 human participants, all of whom were volunteers from within the Intelligent Systems Research Centre (ISRC) at the Ulster University (UU) Magee Campus. All participants were male aged between 18-65 years who were in generally good health, have never been diagnosed with a heart or lung condition and have never had surgery on their heart or lungs. Due to the nature of the data recording for respiratory rate and the necessity that the robot hand must rest and apply light pressure to the chest

of the participant, no female participants were recruited at this stage of the investigation. Ethical approval for "category A" research was granted by the research governance at Ulster for all experiments carried out. An exclusion process was carried out for each participant prior to participation to ensure that they met the required criteria. Each successful participant was fully briefed about the experiment and signed a consent form prior to participation. To ensure that the participant was in generally good health at the time of data collection, the researcher collected each participants' temperature using an ear thermometer with a new tip for each participant, following training on how to do so from a medical professional. The medical professional also oversaw the procedure and measured each participant's pulse and respiratory rate in each experiment as ground truth data to verify the accuracy of the artificial system approach described in this chapter.

For collecting both pulse and respiratory data, the BioTAC fingertip is allowed 15-20 mins to reach its steady state temperature (approximately 35°C, 10°C above ambient) after being first powered on. Unlike the experiments in Chapter 4 where the BioTAC fingertip was used within an experimental rig and data were collected and stored through the use of a Graphical User Interface (GUI) at a rate of 4400Hz, in the experiments presented in this chapter the data generated from the BioTAC fingertip are transferred through Ethercat on the Shadow Hand. Therefore, due to the quantity of data being transferred the PAC, PDC, TAC and TDC values from the BioTAC fingertip are recorded at a reduced frequency of 100Hz. These values are recorded using the Robot Operating System (ROS) and a dataset for PAC, PDC and TAC data was formed using Python.

In order to measure pulse, each participant was seated in front of the robot hand and asked to roll up their left sleeve and remove any jewellery from their wrist. They were asked to place their left wrist facing upwards into the robot hand. The PAC values can be used to determine the vibration (of the internal conductive fluid) caused by the pulse when the fingertip is pressed against the radial artery. To press the finger against the radial artery the Shadow Hand positions its TH below the wrist and moves its FF and MF in small increments towards the radial artery on the ventral aspect of the wrist on the side of the thumb of a participant, as illustrated in Figure 5.2(a). Using the electrodes in the BioTAC fingertip the force applied to the finger is constantly measured and once sufficient contact is made with the wrist by the FF and MF, the fingers stop moving and the system begins recording the PAC data. The Shadow Hand

applied a safe level of force similar to that which a human would apply. This force was measured using the ATI Nano17 6-axis Force/Torque (F/T) Sensor (ATi, 2017) from a medical professional mimicking the same procedure for reading pulse from a human wrist. The fingertips are soft and warmed to approximately the same temperature as a human fingertip and therefore did not cause any pain or discomfort to the participants. As seen in Figure 5.2(a), this action replicates the action of a human when attempting to measure a participant's pulse by using the fingers to contact the wrist and count how many beats are felt per minute. Three datasets of 120 seconds each were collected with a short break in between each one. The individual was at rest in each case.

In order to determine the RR of the participant, contact with the chest of each of the 12 participants was made using the Shadow Hand, as shown in Figure 5.2(b). The hand started in an open position and both the FF and MF moved towards the upper left side of the participant's chest in small increments. The electrodes on the BioTAC were constantly monitored until sufficient contact was made with the chest. The required force was determined using the ATI Nano17 6-axis F/T Sensor (ATi, 2017) measuring the force that a medical professional applies to a human chest when attempting to measure respiratory rate. In this case static vibration data (PDC) were used to identify the movements of the chest wall more effectively than PAC. Furthermore, as breathing can cause a lot of added artefacts and noise, another modality was measured along with vibration data, namely the thermal conductivity value (TAC). As the chest wall rises during breathing, the skin of the participant pushes against the inside clothing and as a result of the concentrated indirect contact with the skin under the clothing the thermal conductivity value (TAC) fluctuates as the fingertip senses the change in temperature and friction. Therefore, both TAC data and PDC data were recorded to assess respiratory rate in order to add robustness to the algorithm.

5.2.2 Waveform Pre-processing

In order to reduce noise and smooth the waveform of both the pulse and respiratory data, in all cases, two stages of filtering were applied to the data. As a human heart beat is a low frequency sound, various low pass filters were evaluated for the first stage of filtering. Infinite impulse response (IIR) filters generally achieve a required response with a much lower filter order than finite

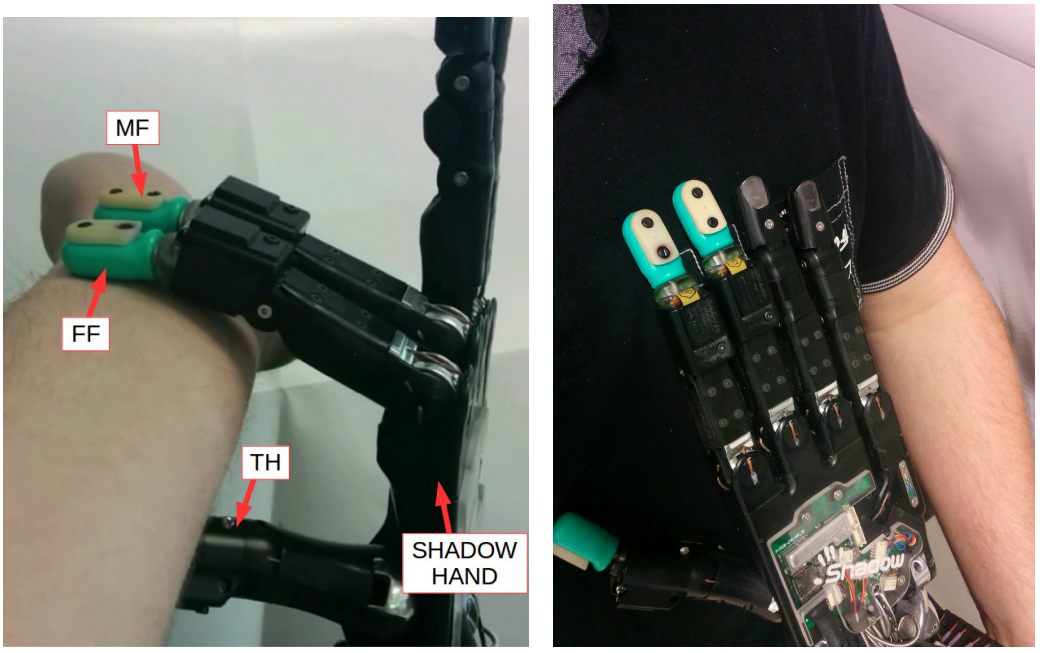

(a) (b)

Figure 5.2: (a) Image showing the Shadow Hand taking the participant's pulse (b) Image showing the Shadow Hand resting on the participant's chest to measure RR

impulse response (FIR) filters and therefore are more efficient (Elliott, 2001). Various types of IIR filters including Chebyshev Types I and II, Butterworth, and elliptic were evaluated along with various cut off frequencies and filter orders. Following the application of the various filters, the filtered signal was visually inspected to determine if all of the troughs representing heart beats and breaths taken in the waveform were preserved whilst as many incorrect troughs (i.e. noise) as possible, were removed. By visual inspection of filtered signals following a range of filtering types, it was found that a Butterworth IIR filter with a cut off frequency of 10Hz and a filter order of 10 performed best, as it produced the preferred smoothing without loss of valuable data. Therefore this filter was used throughout the pulse and respiratory experiments presented.

A wavelet decomposition algorithm (Mallat, 2008) was then employed as the second stage of filtering to perform smoothing of the waveforms. Wavelets are very efficient in dealing with noisy data series due to their multi-scaling property (Haven et al., 2012). Wavelets are defined by the wavelet function, $\psi(x)$, (i.e. the mother wavelet) and a scaling function , $\phi(x)$, (know as the father wavelet) in the time domain. Effectively, the wavelet is a band-pass filter, meaning that every time the wavelet is stretched by a factor two in the time domain, its bandwidth is halved. Therefore, with every stretch of the

wavelet only half of the remaining spectrum would be covered (Kaiser, 1994). This means that an infinite number of wavelets would be required to cover the entire spectrum. Hence, a low-pass filter known as the scaling function, first introduced by Mallat (1989), is designed so that its spectrum neatly fits in the space left open by the wavelets. It is used to filter the lowest level of the transform and ensure that all the spectrum is covered.

Discrete wavelet transform (DWT) algorithms with two wavelet functions, namely Haar and spline (SPL) (Luo et al., 2006) and various levels of decomposition were evaluated. The Haar wavelet is a wavelet family compiled of a sequence of rescaled "square-shaped" functions and is the simplest possible wavelet (Misiti et al., 2007). The Haar wavelet function, $\psi(x)_h$, is defined by Equation 5.1 and the Haar scaling function, $\phi(x)_h$, is defined by Equation 5.2 (Misiti et al., 2007).

$$\psi(x)_h = \begin{cases} 1 & \text{for } 0 \leq x < \frac{1}{2}, \\ -1 & \text{for } \frac{1}{2} \leq x < 1, \\ 0 & \text{otherwise} \end{cases} \tag{5.1}$$

$$\phi(x)_h = \begin{cases} 1 & \text{for } 0 \leq x < 1, \\ 0 & \text{otherwise} \end{cases} \tag{5.2}$$

The SPL wavelet function used in the DWT wavelet algorithm is the B-spline of order 2, namely the quadratic B-spline (Misiti et al., 2007). The SPL wavelet function, $\psi(x)_s$, is defined by Equation 5.3 and the SPL scaling function, $\phi(x)_s$, is defined by Equation 5.4 (Misiti et al., 2007).

$$\psi(x)_s = \begin{cases} \frac{1}{2}x^2 & \text{for } 0 \leq x < 1, \\ -x^2 + 3x - \frac{3}{2} & \text{for } 1 \leq x < 2, \\ \frac{1}{2}x^2 - 3x - \frac{9}{2} & \text{for } 2 \leq x < 3, \\ 0 & \text{otherwise} \end{cases} \tag{5.3}$$

$$Œ(x)_s = \frac{1}{4}N_3(2x) + \frac{3}{4}N_3(2x-1) + \frac{3}{4}N_3(2x-2) + \frac{1}{4}N_3(2x-3) \tag{5.4}$$

It was empirically found that a DWT wavelet algorithm with a SPL wavelet filtering algorithm and a wavelet decomposition value of 5 is the most effective algorithm providing smoothing without loss of information. Therefore, this

was applied to all waveforms collected for pulse and respiratory rate.

Reichardt and MacGinitie (1962) initially studied the use of lateral inhibition in various neural networks and since then there has been continuous interest in these networks, particularly in the field of sensory analysis. According to Bekesy (1967), lateral inhibition is an ubiquitous phenomenon which is assumed to be operative in all sensory systems. It is based on a concept of suppression by a given element on its topological neighbours where the capacity of an excited neuron reduces the activity of its neighbours. It is believed to be responsible for a number of self-organising processes in biological systems ((Kral and Majernik, 1996)). Using lateral inhibition couplings, the sharpening of Artificial Neural Networks (ANN) input data can be achieved ((Kral and Majernik, 1996; Li et al., 1992). Kral and Majernik (1996) study various lateral inhibition neural networks regarding their ability to sharpen input excitation curves. They also introduce two new entropy-like quantities, namely iteration entropy and the rate of convergence. In line with work done by Kral and Majernik (1996), who used lateral inhibition neural networks to smooth waveforms in their analysis of the auditory system, lateral inhibition as a third stage of smoothing was used to further smooth the pulse and respiratory waveforms. The method is capable of highlighting the peaks in a waveform and suppressing any data points that were not considered to be part of a peak by using a linear threshold output function with the lateral inhibition neural network. As lateral inhibition is used to emphasise peaks in data, the data is inverted for trough detection cases. The addition of lateral inhibition as a third stage of smoothing is evaluated against using only the low pass filter and the wavelet algorithm as a two-stage smoothing approach.

5.2.3 BPM and RR calculation

Upon visual inspection of the pulse waveforms following filtering from the low pass filter and smoothing using DWT wavelets, it is clear that there is a prominent trough in each case representing a pulse (heart beat) and breath taken, as seen in Figure 5.3(b). Therefore, by identifying and calculating the number of troughs in a 60 second window of the pulse waveform a calculation of the participant's BPM can be completed. However, as breathing is calculated by analysing the PDC and TAC readings from the BioTAC, i.e. the pressure and thermal conductivity, it was evident upon visual inspection following the first two stages of filtering and smoothing that in these waveforms peaks are more

prominent than troughs, as seen in Figure 5.4(b) and Figure 5.5(b). This is to be expected as when the chest wall raises (to accommodate an intake of air) the skin presses firmly against the clothing increasing thermal conductivity which is measurable using the BioTAC fingertip. Therefore by identifying the number of peaks (breaths taken) within a 60 second period of the respiratory data the participant's RR can be calculated.

Although the troughs and peaks can be clearly seen when inspecting the graphs, it is required that they are detected automatically in order to calculate the BPM and RR of a participant. In order to detect prominent troughs and peaks in the waveforms a modified version of a publicly available function called "peakdet" in MATLAB is utilised. This function detects the local maxima and minima in a wave signal. The function uses a threshold (default 0.5) of the difference between the suspected trough or peak and its surrounding values in order to declare it as a peak or trough.

However, due to the range of variance within the datasets for each modality (i.e. PAC, PDC and TAC), the default threshold was not adequate for accurately differentiating all the troughs and peaks from within the various waveforms. Therefore, a dynamic threshold was required. Two thresholding approaches were evaluated, one semi-automatic and one fully automatic. The semi-automatic approach enabled calibration per participant for improvement of accuracy as the troughs and peaks in the graphs vary in terms of how prominent they appear from their surrounding values across each participant. This helps to avoid any outstanding residual noise being detected as a trough or peak. As the troughs or peaks are required to be detected with respect to the resting waveform the calibrated dynamic threshold is calculated for each modality per participant using the standard deviation and is given by:

$$dt_m = x \times \sigma \tag{5.5}$$

where dt_m is the calibrated dynamic threshold for each modality per participant, x is a factor calibrated for each participant per modality, and σ is the standard deviation of the waveform. Various values of x were applied and tested for each modality and manually calibrated for each participant until an optimal value for the threshold was determined enabling accurate detection of troughs and peaks representing heart beats and breaths respectably.

The fully automatic thresholding approach was implemented based on the technique used by Jacobson (2001) in his approach for automatic peak detection

in ECG signals. The approach considers the fact that the slope of a leading edge of a peak is positive. The derivative of samples greater than zero are classified into two clusters, one consisting of peak slopes and the other consisting of the remaining values in the waveform. Using a nearest neighbour style approach to separate the two clusters, each data point in the waveform is considered in turn and assigned to the cluster whose mean is closest in value to the data point. Once this is completed for all data points, new means are calculated for the two clusters and the process is completed again where each data point is classified into the two clusters. At each iteration the difference between the means of the two clusters is calculated and the process continues until the difference is below a specified termination value. Due to the nature of the data analysed and considering how noisy it can be, the algorithm is designed to continue until the difference between the two means is less than 1 in the expectation that this would produce the most accurate threshold for each waveform, resulting in accurate peak detection. The results are presented for algorithms using the semi-automatic approach and the fully automatic approach in order to evaluate which method is most accurate.

5.2.4 Pulse to Pulse (PPI) and Breath to Breath Interval (BBI) Calculation

In order to determine if a pulse is regular, the time difference between each detected pulse, PPI, is calculated across the waveform. An individual may have a normal heart rate (i.e. between 60-100 BPM) but their pulse may not be beating at regular time intervals or may be following an irregular pattern, i.e. they would be classed as having an arrhythmic heart beat or a sinus arrhythmia. Likewise in order to determine if the participant's breathing is regular the BBI is calculated across the waveform. Both the PPI and BBI are time intervals between each pulse and breath respectively.

To classify the interval calculated from the collected waveforms, firstly the expected PPI (time difference between each detected pulse) and BBI (time difference between each detected breath) in the given time of the data collected (i.e. 60 seconds) are calculated in order for the heart rate and RR to be classified as regular and healthy. This expected interval, I_{exp} is defined as:

$$I_{exp} = \frac{t_{wf}}{N_{td}} \tag{5.6}$$

where I_{exp} is the expected interval in seconds (s) for the heart rate or RR to be regular, t_{wf} is the complete length of time (s) of the waveform and N_{td} is the number of peaks or troughs detected in the waveform.

The calculated actual interval between each individual pulse or breath detected in the waveform is calculated by:

$$I_{obs} = t_{ct} - t_{pt} \tag{5.7}$$

from a human chest where I_{obs} is the observed interval between each individual trough detected (s), t_{ct} is the time stamp of the current trough detection (s) and t_{pt} is the time stamp of the previous peak or trough detected.

A sliding window is utilised to reduce outliers or any residual noise in the waveform affecting the interval classification. Along with the I_{obs} being calculated at every time point, an average of all the I_{obs} values within the window at each step is calculated. The sliding window moves in time steps of 0.5 seconds and has a length of 5 seconds. Equation 5.8 determines how many sample windows are analysed across each dataset.

$$N_{sw} = \frac{N_{tds} - (l_{sw} \times N_{dps})}{(TS_{sw} \times N_{dps})} \tag{5.8}$$

where N_{sw} is the number of sample windows analysed across the complete dataset, N_{tds} is the number of data points in the complete dataset, l_{sw} is the length of the sliding window (s), N_{dps} is the number of data points recorded per second, and TS_{sw} is the time step of the sliding window (s). The average I for each window of data was calculated as:

$$I_{\bar{obsw}} = \frac{\sum_{I_{obsw}=1}^{N_{tdw}} I_{obsw}}{N_{tdw}} \tag{5.9}$$

where $I_{\bar{obsw}}$ is the average interval (s) between the troughs detected within the window, I_{obsw} is the individual interval between the troughs detected within the window (s) and N_{tdw} is the number of troughs detected within the window.

I_{obs} and $I_{\bar{obsw}}$ are then analysed against the expected interval required for a regular and healthy pulse rate, I_{exp}, (equation 5.6) in order to determine if the pulse is regular or arrhythmic. Clearly, due to the nature of the data, it is not realistic to expect every individual I_{obs} reading or the average interval reading of a 5

second window of data, $I_{obs\bar{w}}$, to be exactly the same as the expected rhythmic average, I_{exp}. Therefore, following discussion with a medical professional it was estimated that a tolerance of within $\pm$25% of the rhythmic average PPI at each pulse detected was sufficient to classify between regular (healthy) and arrhythmic pulse rates. If the individual PPI is within this tolerance then the heart rate is classified as being regular. Likewise the I_{obs} and $I_{obs\bar{w}}$ are analysed to determine if the participant's breathing is regular or irregular. A similar tolerance is suggested for the BBI to be within for the breathing to remain classified as regular.

5.3 Results

In the following section, results are presented for BPM and RR identified from waveforms following two forms of smoothing. Results for BPM and RR identified from waveforms following a third stage of smoothing by using lateral inhibition neural networks are also presented. The results are evaluated against the manual measurement of each participant's pulse measured by a medical professional. Furthermore, results for the calculation of the PPI and BBI are presented.

For comparison, the algorithm's performance is also evaluated against a modern off the shelf light-based pulse measurement device. During data collection, the participant's pulse was also measured using an Android smart-phone application called "Heat Rate Monitor" (Mellado, 2013). The smart-phone application requires the user to place their index finger against the camera lens of the phone. It then analyses the input from the camera feed, detecting the slight changes in red colour to identify pulses. The algorithm applies band pass filtering to the signal and then begins a sliding window approach to analyse the signal. Within the sliding window Fast Fourier Transform (FFT) is applied to the signal followed by a peak detection algorithm in which it classes each peak as a pulse. A smoothing algorithm is then applied to the signal to allow for it to appear back on the smart-phone screen as a smooth waveform with minimal noise.

Similarly, it was found that applying the low bandpass Butterworth IIR filter to the raw PAC, PDC and TAC data collected using the BioTAC, reduced noise and smoothed the waveform to a level that may in some cases be sufficient to clearly identify peaks and troughs. This can be seen in Figure 5.3(a) which

shows an example of the raw PAC data collected from the wrist of one of the participants and the filtered data following application of the IIR filter, in this case from participant 3.

Figure 5.4(a) and Figure 5.5(a) show graphs of the raw data and the data following the first stage of filtering with the low pass filter for the PDC and TAC datasets respectively collected when the fingertip was applied to the participant's chest (again participant 3 in this case). It can be seen from these graphs that although application of the low pass filter did not make a dramatic change to the data, it has still smoothed it slightly in the areas of the peaks and troughs where the data were noticeably noisier.

Application of the second stage of filtering, namely the DWT noise reduction process, to the raw data successfully further removed noise, smoothed and normalised the waveform to a level that would allow for successful trough and peak and therefore pulse and breath detection. The data contained significantly less noise compared with using a low pass filter alone. This is evident in Figure 5.3(b) which shows the PAC data following the application of the DWT noise reduction algorithm where the data are clearly less noisy than the raw or single stage filtered data. Figure 5.4(b) and Figure 5.5(b) show the PDC and TAC waveforms, respectively, of data recorded from the individual's wrist following the application of the DWT noise reduction algorithm. It is evident that the second stage of smoothing in the case of the respiratory data was especially effective resulting in a waveform where troughs and particularity peaks are easily identified.

As described in Section 5.2.2, a third smoothing algorithm, namely lateral inhibition, was also applied to each dataset to evaluate if it would improve the accuracy of pulse and breath detection in their respective datasets. It can be seen from Figure 5.6(a) that the application of the lateral inhibition algorithm does not reduce noise any further than the two stage filtering process (shown in Figure 5.3(b)) and therefore provides no further benefit. As is evident in Figure 5.6(b) and Figure 5.6(c), when analysing the respiratory data collected from the participants' chests, it is clear that lateral inhibition provides further smoothing of the data in comparison to the smoothing following the application of the two stage filter (shown in Figure 5.4(b) and Figure 5.5(b)). However, this does not necessarily mean that it will increase peak detection accuracy.

The trough/peak detection algorithm with the semi-automatic thresholding method has proven to work well for pulse and breath detection enabling accurate BPM calculations. Figure 5.7(a) shows the troughs (representing pulse)

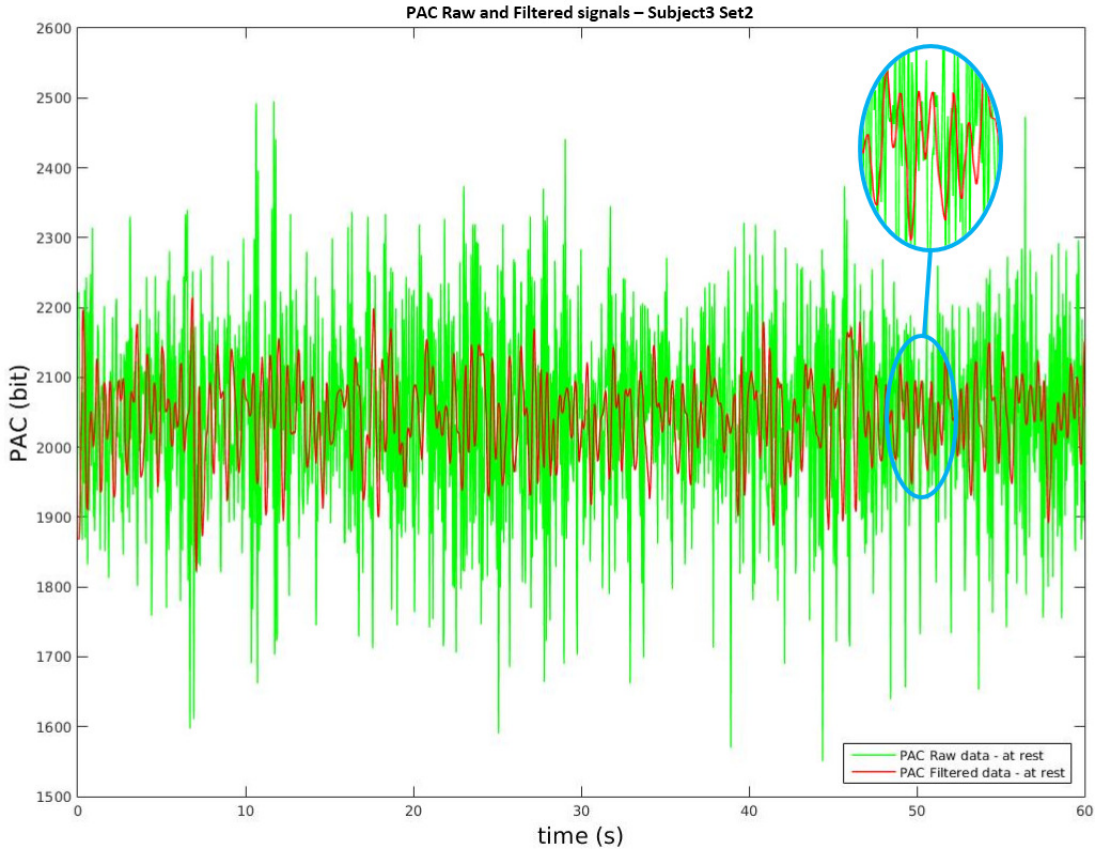

(a)

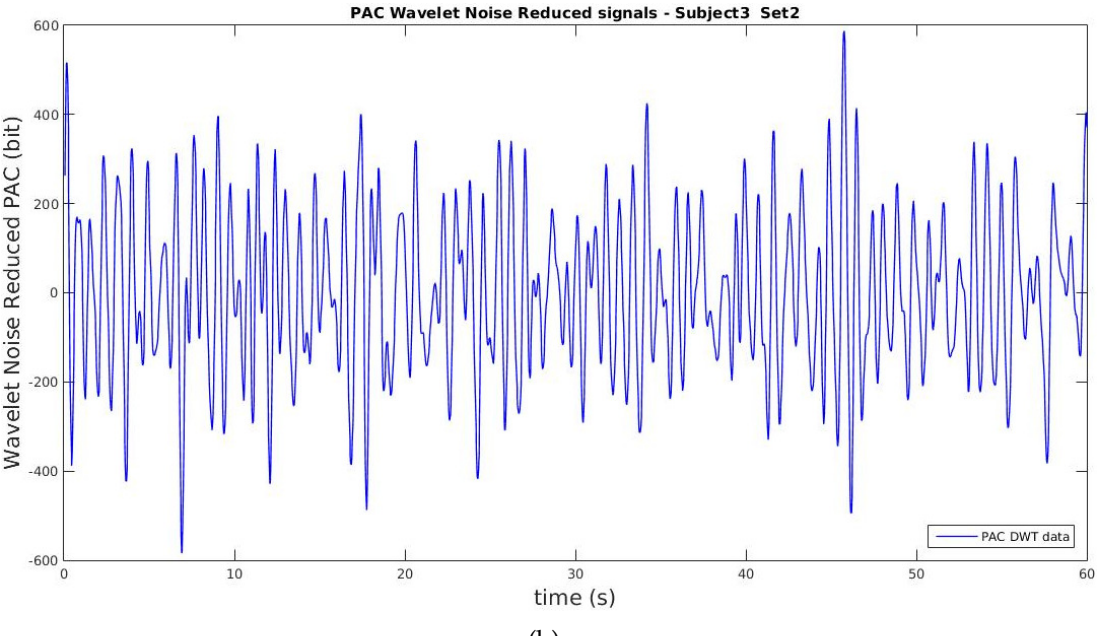

(b)

Figure 5.3: Graphs showing (a) the raw and low pass filtered PAC data collected from participant three's wrist and (b) the PAC data after wavelet smoothing was applied.

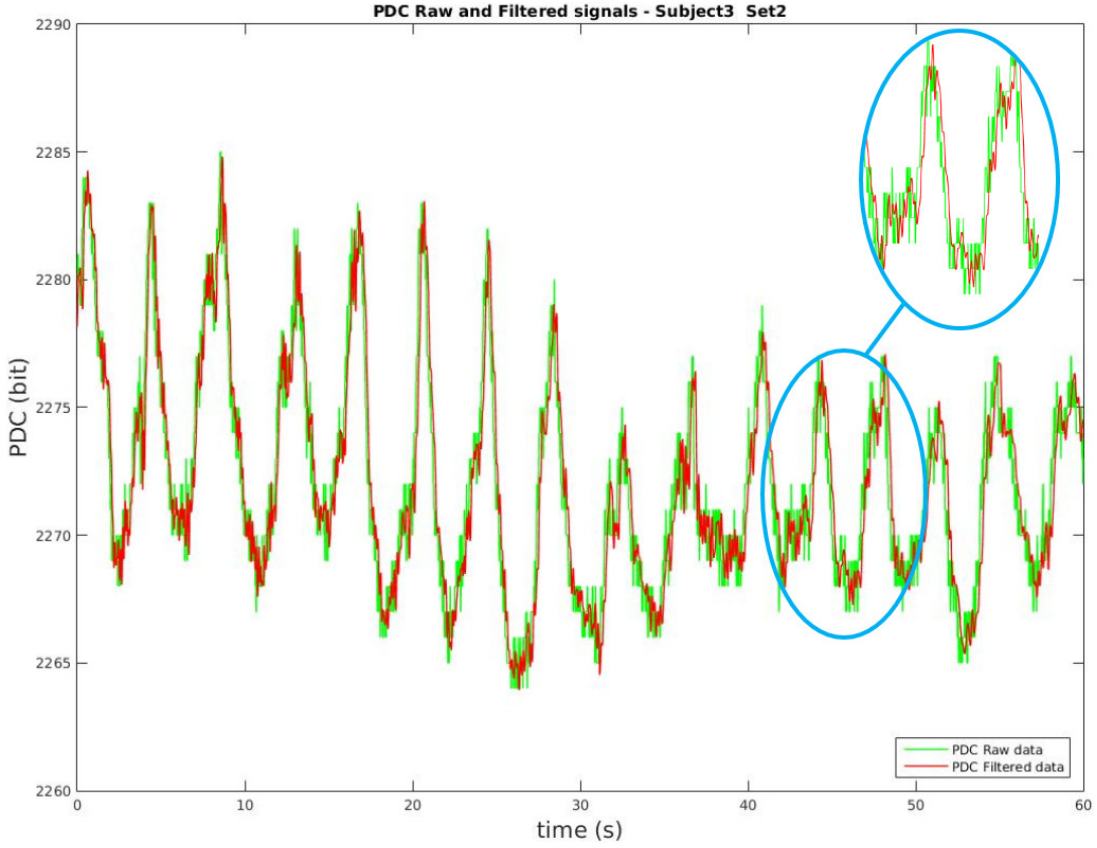

(a)

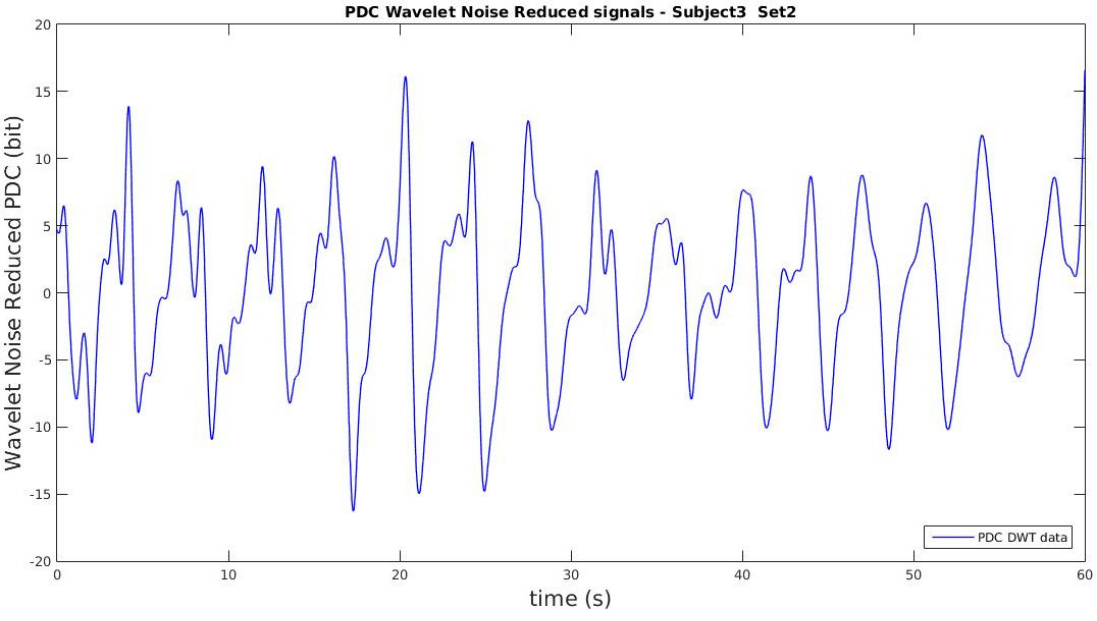

(b)

Figure 5.4: Graphs showing (a) the raw and low pass filtered PDC data collected from participant three's chest and (b) the PDC data after wavelet smoothing was applied.

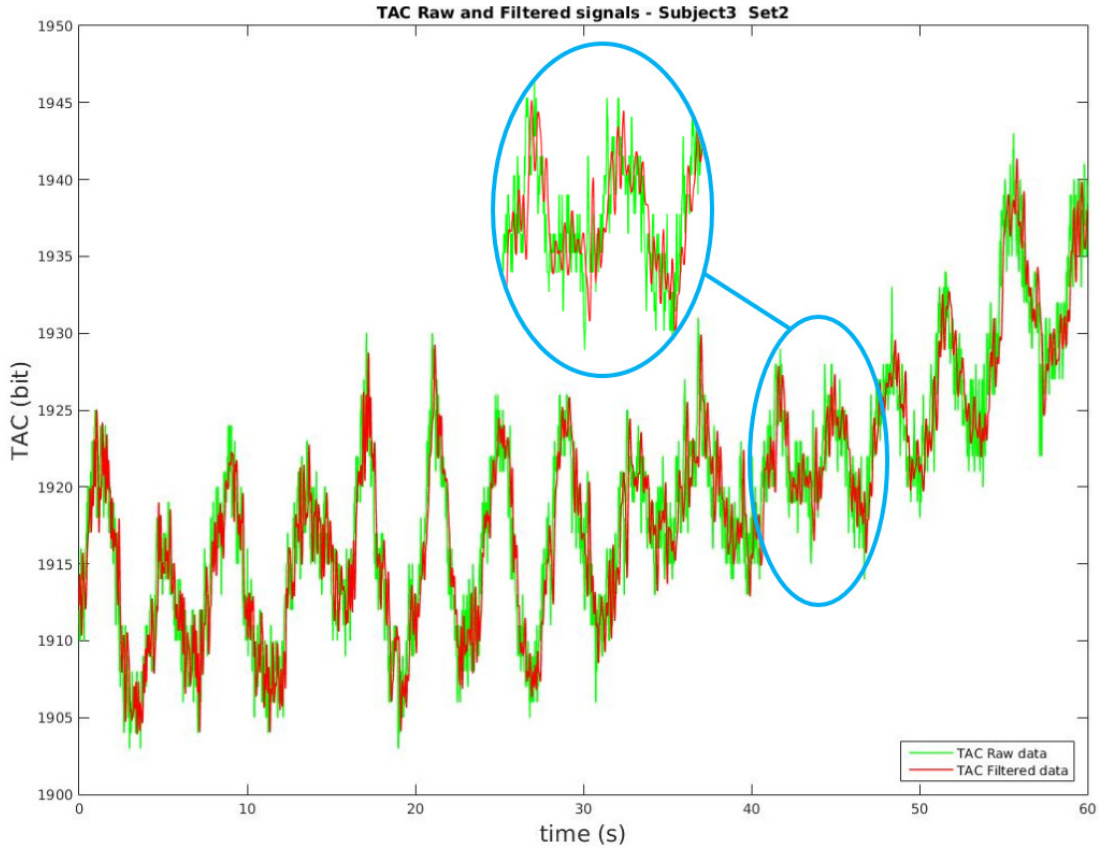

(a)

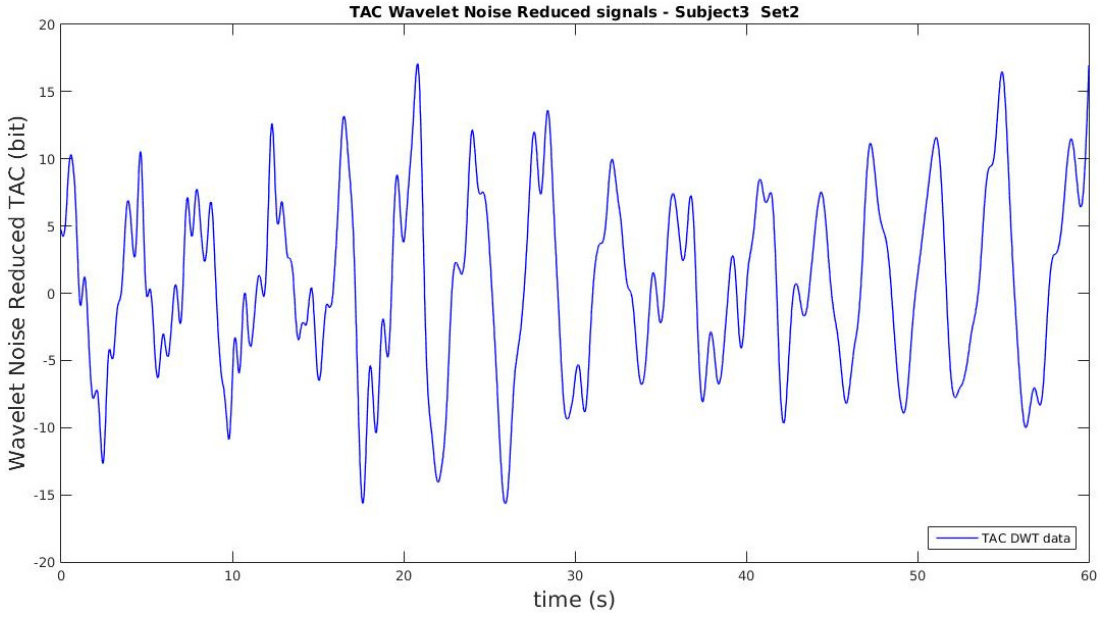

(b)

Figure 5.5: Graphs showing (a) the raw and low pass filtered TAC data collected from participant three's chest and (b) the TAC data after wavelet smoothing was applied.

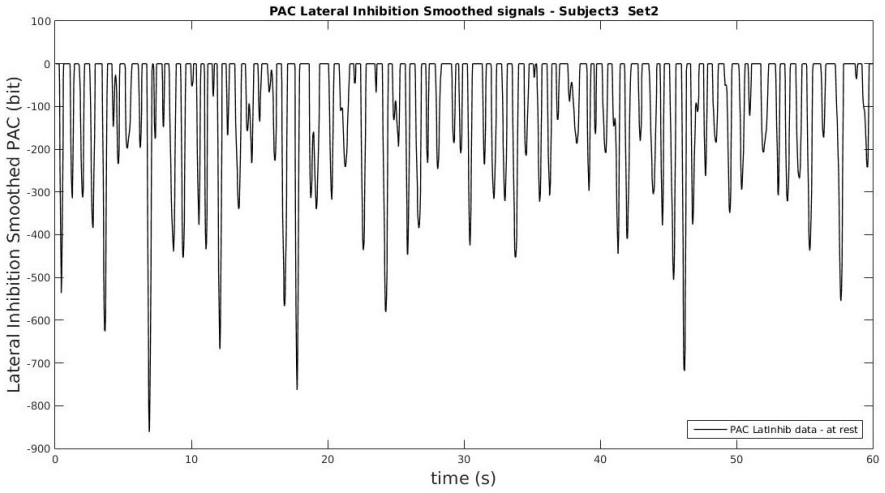

(a)

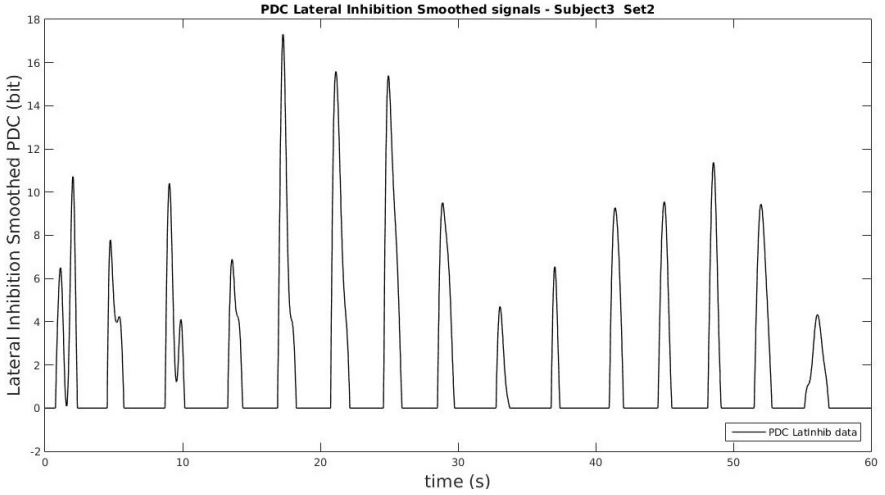

(b)

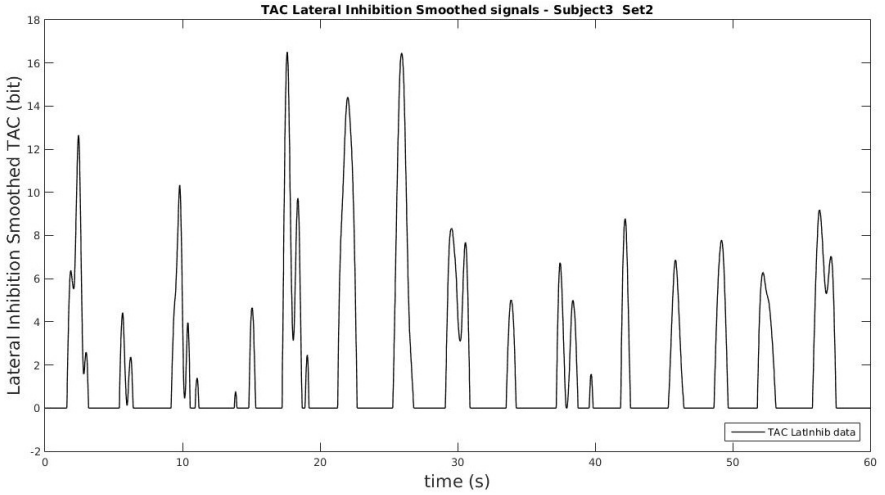

(c)

Figure 5.6: Graphs showing (a) the PAC data collected from participant three's wrist, (b) the PDC data and (c) the TAC data collected from participant three's chest following application of the lateral inhibition algorithm to all three categories of data.

detected by the trough detection algorithm using the semi-automatic thresholding method, highlighted by blue stars. Tuned threshold values for each participant were empirically found and ranged from 0.090-1.323 (representing value x in equation 5.5) Figures 5.7(b) and 5.7(c) show the breaths detected represented by peaks in the PDC and TAC waveforms respectively. It can be seen from all of the graphs in Figure 5.7 that the trough detection algorithm detects the majority if not all of the troughs or peaks in all cases when the thresholds are semi-automatically calculated with manual fine tuning. Tuned threshold values for each participant per modality were empirically found and ranged from 1.000-2.545 for PDC and from 0.600-2.500 for TAC(representing value x in equation 5.5). However, it can also be seen in Figure 5.7(b) that there can be some instances where it would be expected that a peak would be detected as a breath but it hasn't been detected (one such instance is highlighted by the green circle). This is an example of where the points on either side of the peak are just below the threshold for difference and therefore it is not classified as a breath. It is due to borderline cases like this that some of the calculated BPM and RR may be marginally incorrect when compared with the readings measured by a medical professional. However, the benefit of this approach is that the algorithm does not detect all peaks or troughs in the waveforms particularly when a series of them occur and would clearly be an incorrect representation of pulse or breaths. An example of this is highlighted by the purple circle in Figure 5.7(c) where there are three clear peaks however they are correctly not considered as breaths by the algorithm.

Following the application of the third stage of smoothing, namely lateral inhibition, the trough and peak detection algorithm was applied and the performance evaluated. Figure 5.8 shows examples of detected troughs in the PAC data and detected peaks in the PDC and TAC data following the application of the lateral inhibition smoothing algorithm. Although in most cases the algorithm performed well and detected the majority of peaks and troughs, the smoothing was not sufficient to highlight the correct points of the waveform that represented the pulses and breaths. This was caused by the algorithm amplifying incorrect troughs or peaks in the waveform which are in turn related to pulse and breaths, examples of which are highlighted by the green circles in the PAC, PDC and TAC graphs in Figure 5.8.

The trough/peak detection algorithm with fully automatic thresholding method has been shown to perform weaker than the semi-automatic thresholding method. It has proven to be over sensitive when detecting troughs and peaks.

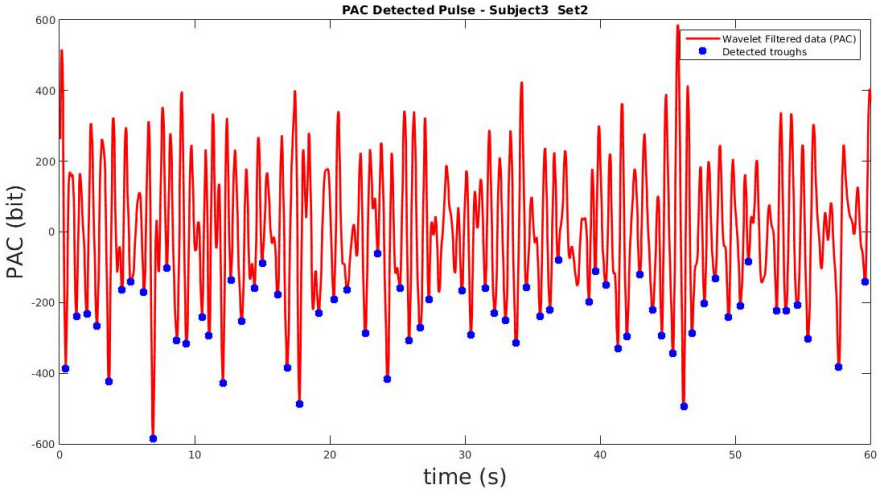

(a)

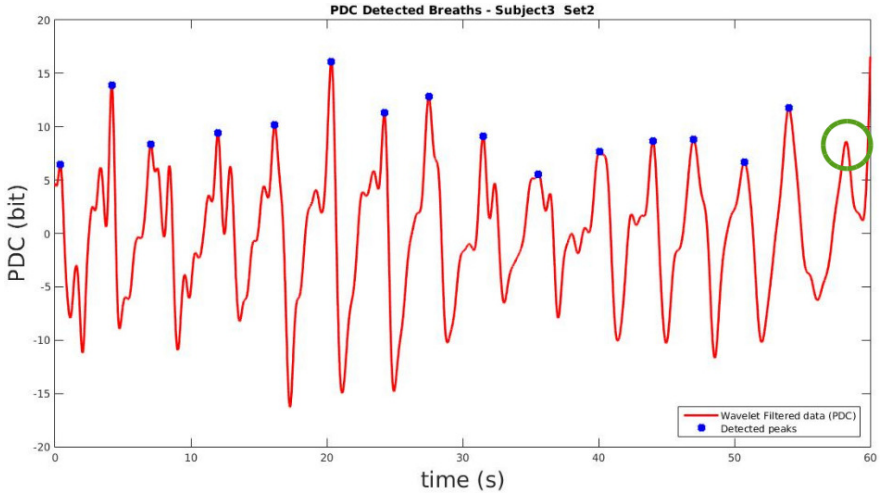

(b)

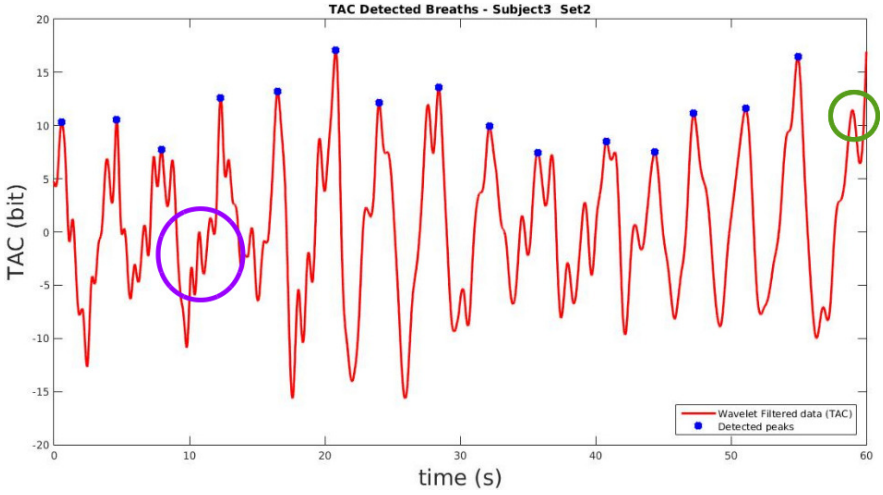

(c)

Figure 5.7: Graphs showing (a) the detected troughs in the PAC data relating to pulse, (b) detected peaks in the PDC and TAC data (c) representing breaths.

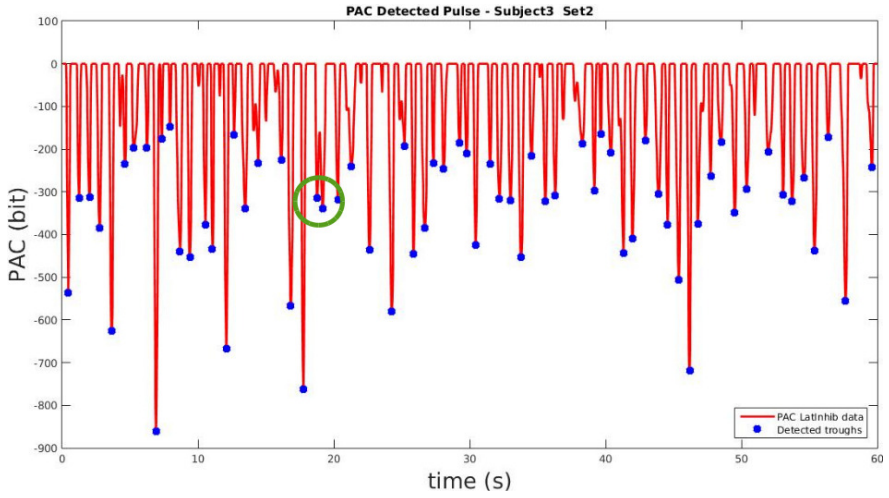

(a)

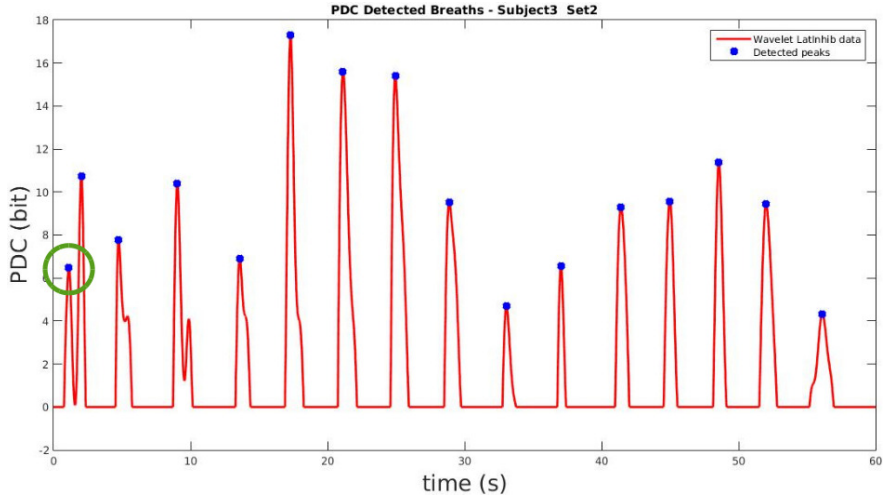

(b)

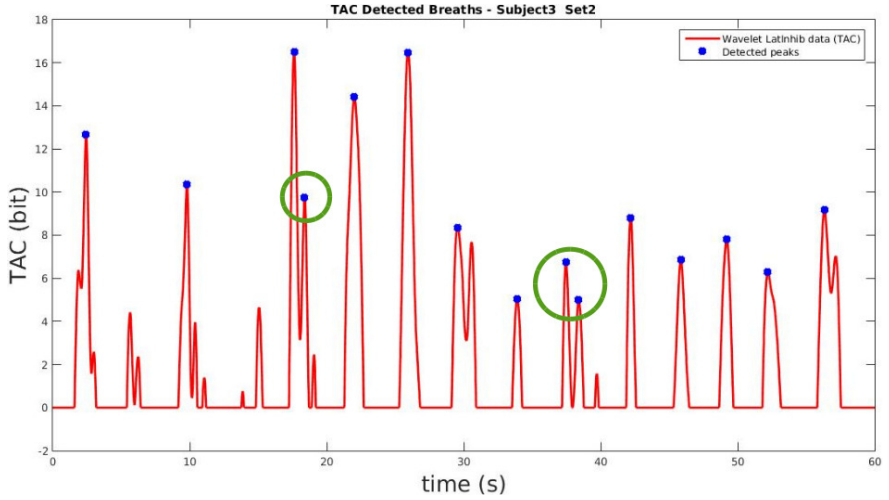

(c)

Figure 5.8: Graphs showing (a) the detected troughs in the PAC data relating to pulse, (b) detected peaks in the PAC and TAC data (c) representing breaths following the application of lateral inhibition smoothing.

An example of this is demonstrated in Figure 5.9 where there are too many peaks detected as breaths particularly in a short space of time, highlighted by the green circles.

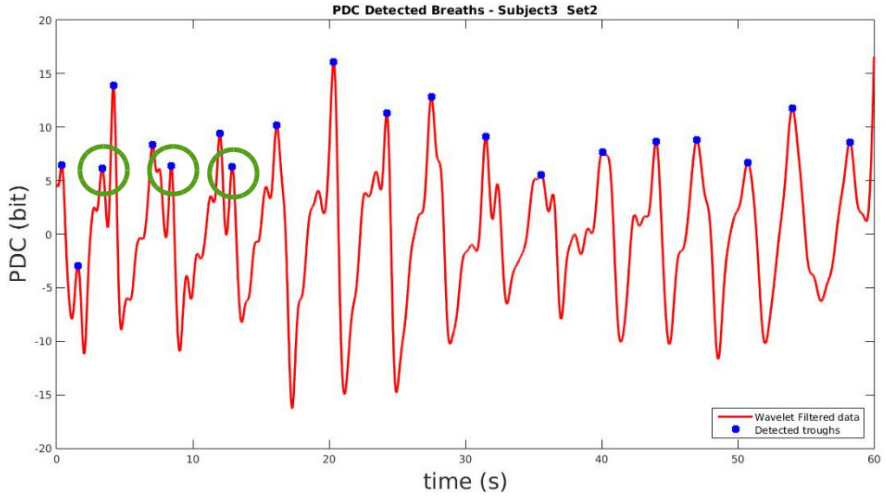

Figure 5.9: Graph showing the peaks detected in the PDC dataset with the use of fully automatic thresholding

Analysis of the results for collection of the BPM from the participants can be seen in Table 5.1. The average of the absolute difference between the calculated BPM and the actual BPM measured by a medical professional is shown for each method. The minimum and maximum difference from the actual BPM that each method measured is also shown in Table 5.1. A calculation of the accuracy of each method when classifying if the participant was bradycardic, normal or tachycardic is also presented in the "Correct Class (%)" row of Table 5.1. Results for the two stage filtering approach with semi-automatic thresholding are presented in the column labelled "2 Stage Filtering Semi-automatic (2SFS)". Results for the two stage approach with fully automatic thresholding are presented in the column labelled "2 Stage Filtering Fully-automatic (2SFF)". Results for the three stage approach (i.e. using low pass filtering, DWT and lateral inhibition smoothing) with semi-automatic thresholding are presented in the column labelled "3 Stage Filtering Semi-automatic (3SFS)" and the results for the three stage approach with fully automatic thresholding are presented in the column labelled "3 Stage Filtering Fully-automatic (3SFF)". The results using the Android smart-phone application (Mellado, 2013) are also presented in the column labelled "Smart Phone Application (SPA)". The complete results for the BPM calculated for each participant for the two stage and three stage filtering approaches can be seen in Table A.1 and Table A.2 respectively in Appendix A.

Table 5.1: Table comparing the BPM experimental results

Difference From Actual	**2SFS**	**2SFF**	**3SFS**	**3SFF**	**SPA**
Average	1.47	4.28	2.19	6.22	16.47
Min.	0	0	0	0	1
Max.	13	14	14	17	53
Correct Class (%)	97.22	97.22	97.22	100.00	91.67

It can be seen from Table 5.1 that the best performing approach is the two stage filtering/smoothing approach with the semi-automatic thresholding algorithm as it allows for calibration to be tuned per participant. This approach achieved an average of just 1.47 BPM difference from the actual measured BPM across all datasets. In fact, this method calculated the exact BPM in 13 instances out of the 36 datasets. This approach also correctly determined if the participant's heart rate was classified as bradycardic ("B"), normal ("N") or tachycardic ("T") in 97.22% of cases which collates to 35 of the 36 datasets. It can be assumed that this a poor quality dataset as the approach calculated the BPM with 100% accuracy in the other datasets collected for the same participant.

The three-stage filtering/ smoothing method also achieved 97.22% accuracy when classifying the heart rate. This method was slightly less accurate than the two-stage approach when measuring the BPM achieving an average of 2.19 BPM difference from the actual measured BPM. It is proven from the results presented in Table 5.1 that the addition of the lateral inhibition smoothing for a third stage of filtering/ smoothing does not provide any further benefit in improving the overall accuracy of BPM calculation, however it is still a viable approach which produced accurate results for classifying a heart rate.

The results presented in Table 5.1 show that the fully automatic thresholding approach did not produce results of similar accuracies to those produced by the semi-automatic thresholding method. However, it can be seen that although the algorithm did not determine the exact BPM, it achieves similarly high accuracies when classifying the heart rate. Therefore, it could be a useful approach to rapidly determine an estimate of the status of a person's heart rate in an emergency scenario.

Analysis of the results for the calculated RR can be seen in Table 5.2 and Table 5.3. The average, minimum and maximum of the absolute difference between the calculated RR and the actual RR measured by a medical professional is

shown in Table 5.2 and Table 5.3 for each method when using PDC and TAC respectively. A calculation of the accuracy of each method when classifying if the participant had a slow, normal or fast breathing rate is also presented in the "Correct Class (%)" rows of Table 5.2 and Table 5.3. The same labelling for column headings as Table 5.1 apply to Table 5.2 and Table 5.3. The complete results for the RR calculated from the PDC data using the two and three stage approaches can be seen in Table A.3 and Table A.4 respectively in Appendix A. Also, the complete results for the RR calculated from the TAC data using the two and three stage approaches can be seen in Table A.5 and Table A.6 respectively in Appendix A.

Table 5.2: Table comparing the RR experimental results with PDC data

Difference From Actual	**2SFS**	**2SFF**	**3SFS**	**3SFF**
Average	0.56	7.00	0.92	10.97
Min.	0	0	0	0
Max.	4	28	4	32
Correct Class (%)	91.67	41.67	91.67	22.22

Table 5.3: Table comparing the RR experimental results with TAC data

Difference From Actual	**2SFS**	**2SFF**	**3SFS**	**3SFF**
Average	0.72	5.39	0.83	11.89
Min.	0	0	0	1
Max.	7	24	4	21
Correct Class (%)	72.22	47.22	83.33	11.11

It can be seen from Table 5.2 and Table 5.3 that the best performing method was the two stage filtering/ smoothing with semi-automatic thresholding, as was the case with the BPM calculations. For example, it can be seen that when using PDC, the algorithm achieved on average 0.56 breaths away from the actual breathing rate and an average of 0.72 breaths away when using TAC. It has been proven that both the PDC and TAC data have performed similarly well. In fact the RR was calculated exactly correct 22 times out of a total of 36 datasets with the PDC data and 23 times with the TAC data. In the majority of cases the classification of the RR when using PDC and TAC was classified in the correct class, 91.97% of instances when using PDC data and 72.22% when

using TAC data. It is evident from the results in Table 5.2 and Table 5.3 that the fully automatic thresholding approach was not suitable for classifying the RR of the participants. It is also evident that although the addition of the third smoothing algorithm, namely lateral inhibition, did not lower the accuracy of the RR calculations, it also did not improve the calculations or classifications either and therefore is not worth extra computation time, as is the case when calculating the BPM.

5.3.1 PPI and BBI Calculation and analysis

The pulse to pulse (PPI) and breath to breath (BBI) intervals were successfully calculated between individual troughs detected and the average interval of troughs detected within a sliding window for each dataset. Analysing these values of PPI and BBI can determine if a participant's pulse was in sinus rhythm or a form of arrhythmia and if a participant's breathing is occurring in a regular rhythm. Due to the nature of the data being collected and the noise levels present in the data it is expected that the intervals between detected heart beats and breaths will not be exactly equal from pulse to pulse or breath to breath. This is similar to real life when medical professionals are reading pulse and RR manually. They would not be capable of detecting minor sub second differences in the intervals between pulses or breaths, rather assessing for a change to pulse or breathing intervals representing an irregular or stressed heart or breathing rate, hence the inclusion of the 25% tolerance for the interval times.

Table 5.4 shows an analysis of the PPIs calculated using each method. The average, minimum and maximum percentage of calculated intervals between each detected pulse ere within the 25% tolerance of the average interval. Table 5.5 presents the average, minimum and maximum percentage of the calculated intervals between each detected breath that were within the 25% tolerance of the average interval using PDC data and TAC data. The column headings labels have the same meanings as outlined previously for Table 5.1. It is evident from Table 5.4 that in some cases quite a few of the intervals are not within the tolerance which could represent an irregular pulse however none of the participants had an irregular pulse. As we are analysing accuracies in the scale of tenths and hundredths of a second for these measurements it is difficult to put a binary classification of regularity for a pulse waveform. However in some instances the majority of pulse intervals are within the tolerance, up to 98.88% is achieved by all methods. Similar to the method for calculating BPM, it is

evident from Table 5.4 that the most accurate method for assessing the interval between each heart beat is the two stage filtering/ smoothing approach with semi-automatic thresholding. All calculated PPI results for each participant using PDC and TAC data can be seen in Table A.8 and Table A.9 respectively in Appendix A.

Table 5.4: Table comparing the PPI experimental results

Percentage within tolerance	**2SFS**	**2SFF**	**3SFS**	**3SFF**
Average	73.56	72.07	68.96	65.68
Min.	38.16	38.67	33.75	34.94
Max.	98.88	98.88	98.88	98.88

Due to the nature of the breathing data collected and the fact that there is a lot fewer occurrences of a breath in one minute than a heart beat, it can be less challenging to calculate an accurate interval between each breath than between each heart beat. This is evident from the results in Table 5.5, where there are considerably higher percentages of breath intervals, on average within the 25% tolerance, particularly when using TAC data. Table 5.5 shows that assessment of the intervals between breaths can be very accurate when using the two stage filtering/smoothing approach with semi-automatic thresholding. With similarly accurate results being obtained using PDC data and the highest accuracy of 100.00% was obtained using PDC data as shown in Table 5.5, it is proven that, either PDC or TAC data can be used for analysis of breath intervals. All calculated BBI results for each participant can be seen in Table A.7 in Appendix A.

Table 5.5: Table comparing the BBI experimental results

Data type	**Percentage within tolerance**	**2SFS**	**2SFF**	**3SFS**	**3SFF**
PDC	Average	68.92	51.51	67.63	30.33
	Min.	23.53	33.33	41.18	9.09
	Max.	95.45	77.78	100.00	69.70
TAC	Average	71.87	46.40	69.17	26.84
	Min.	37.50	26.83	19.05	9.09
	Max.	91.67	70.73	95.45	66.67

Graphs showing examples of the calculated PPI between the individual pulses for a participant where the percentage accuracy of PPI was low (participant 4, set 2; 38.16%) and a participant where the percentage accuracy was very

high (participant 6, set 1; 98.88%) are shown in Figure 5.10(a) and Figure 5.10(b) respectively. The two stage filtering/smoothing method with semi-automatic thresholding was used for BPM calculation and PPI analysis in both cases. Also plotted on each graph in Figure 5.10 are the upper and lower limits of the 25% tolerance of the overall average PPI for that dataset, required to class the participant as having a regular pulse rate.

Graphs showing examples of the calculated BBI between the individual breaths for a participant where the percentage accuracy of BBI was low (participant 1, set 3; 41.18%) and a participant where the percentage accuracy was very high (participant 4, set 3; 91.67%) are shown in Figure 5.11(a) and Figure 5.11(b) respectively. Using TAC data, the two stage filtering/smoothing method with semi-automatic thresholding was used for RR calculation and BBI analysis in both cases. Also plotted on each graph in Figure 5.11 are the upper and lower limits of the 25% tolerance of the overall average BBI for that dataset, required to class the participant as having a regular breathing rate.

5.4 Discussion

The use of the BioTAC tactile sensors together with the algorithms presented can determine BPM and RR as accurately as a trained professional. It should be noted that when a medical professional is measuring a pulse in the majority of cases they will only measure for 10, 20 or maybe 30 seconds with their fingers on the participant's wrist to ascertain an estimate of their pulse rate. Although the pulses measured by the medical professional to compare with the accuracy of the system were measured over 60 seconds, there is still a possibility of slight human error. It is clear from the results presented that the artificial system is also capable of such estimates, and indeed accurate measurements of pulse. Often a medical professional is trying to measure vital signs in an emergency situation and therefore their measurements are not exact and have a slight margin of error as is the case with the algorithms presented. Often, when assessing a person's pulse, an estimate of their BPM and their pulse rhythm is sufficient. Likewise, when assessing a person's breathing, a medical professional will simply watch a person's chest for movement when breathing in and out and count how many times this occurs in one minute. In extreme circumstances where vision is inadequate or not possible, the medical professional will rest their hand on the participant's chest and try to determine a breathing rate via touch. The methods presented are capable of such measurements and with

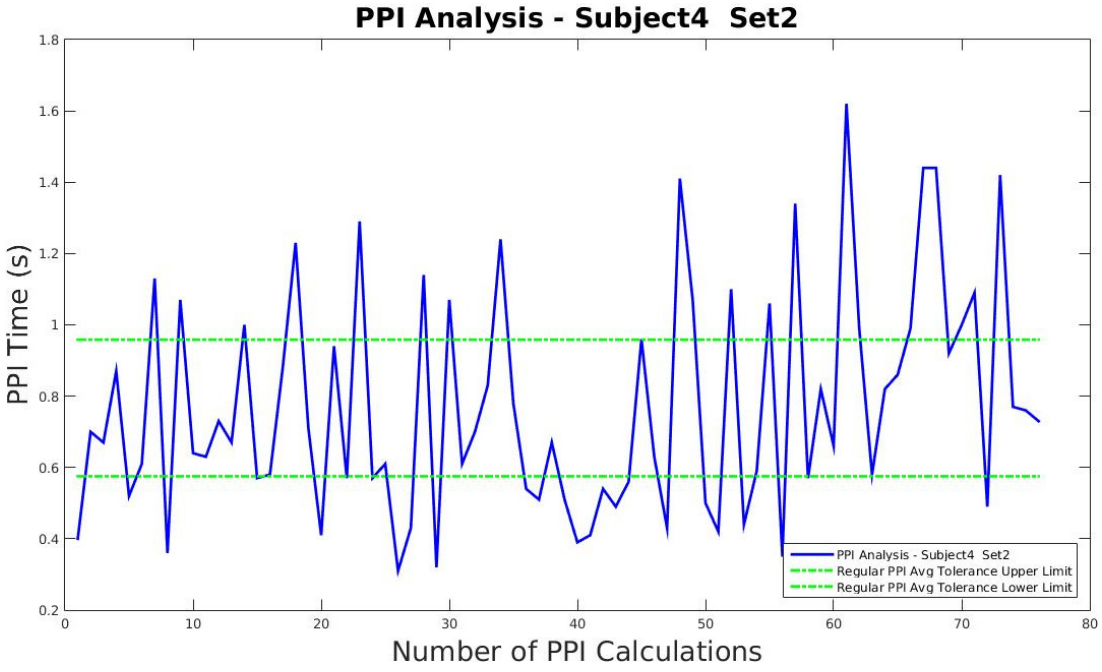

(a)

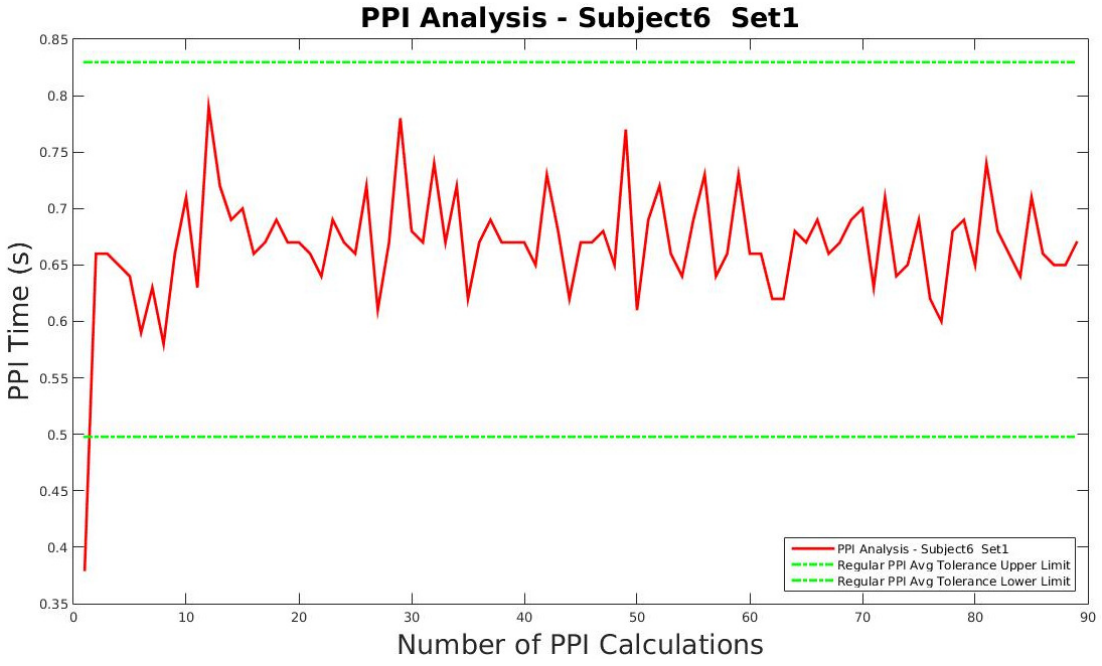

(b)

Figure 5.10: Graphs showing (a) calculated PPI between the individual pulses for participant 4 and (b) participant 6 and the tolerance of the overall average PPI required for regular pulse rate for each dataset

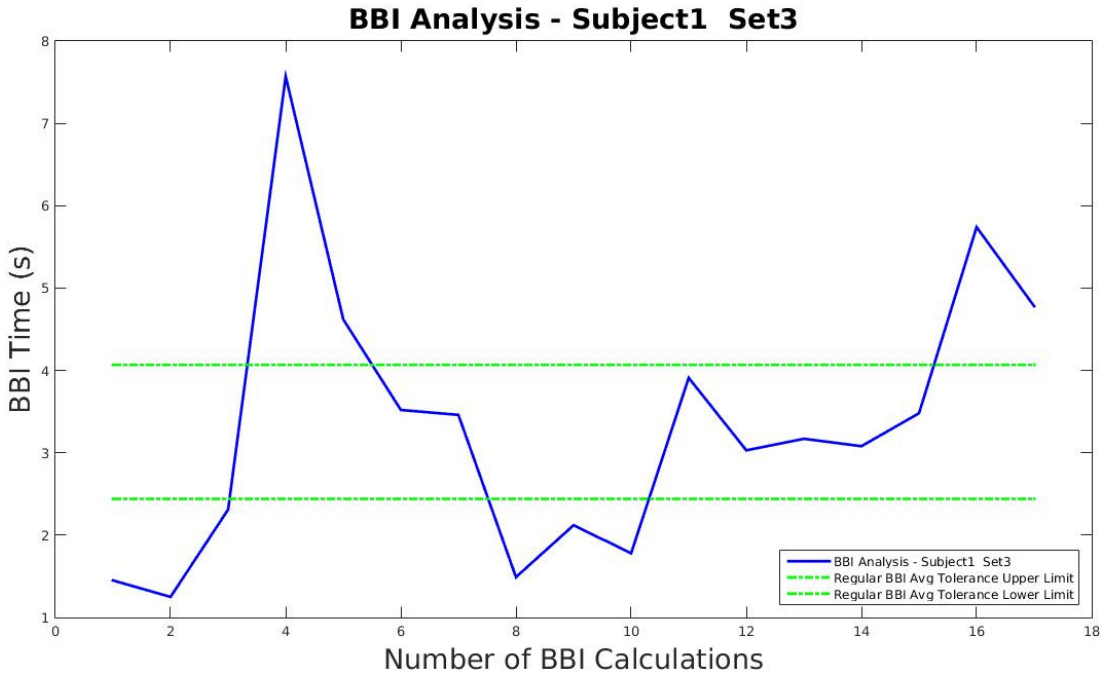

(a)

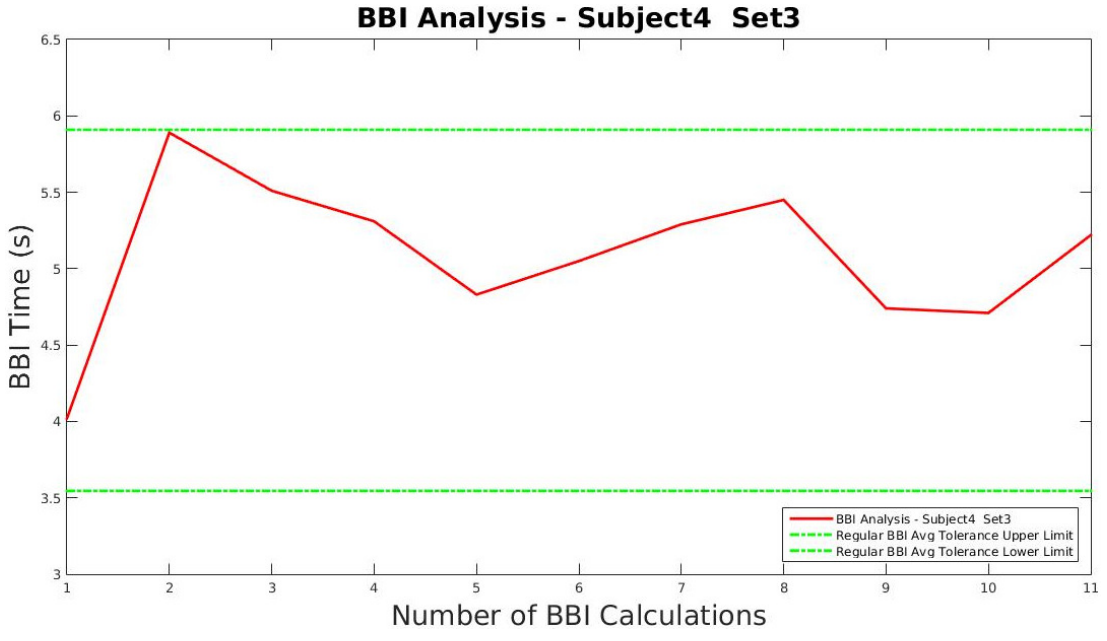

(b)

Figure 5.11: Graphs showing (a) calculated PPI between the individual pulses for participant 4 and (b) participant 6 and the tolerance of the overall average PPI required for regular pulse rate for each dataset

similar accuracies.

It would appear from the graph in Figure 5.10(a) that the variance of individual PPIs for participant 4 in set 2 would indicate a form of arrhythmia however this was not the case. Set 1 and set 3 clearly demonstrate that the participant was healthy and this was also verified by the medical professional. This dataset was relatively noisy in comparison to other two smoothed datasets for participant 4. This highlights the importance of successfully removing noise from the datasets. As seen in Figure 5.10(b), the only PPI that was not within tolerance was the first one and the reason for this is that the participant was in between heart beats when the analysis began and therefore it would have been calculated from time zero, meaning a shorter interval to his first detected heart beat would be expected. Figure 5.10(b) clearly indicates that participant 6 is in sinus rhythm. However, the classification of rhythm in the heart beat and respiratory rate has proven extremely difficult to classify precisely into categories due to the nature of the data collected. Furthermore, similar to calculating the BPM and RR, it not necessary to get an exact value with 100% accuracy in every instance, particularly when we are comparing our results from this artificial system to human measurements which in themselves will contain human error. The aim of this work was to measure two of the vital signs that indicate the current state of a person's health by detecting, measuring and classifying their BPM and RR as accurately as a medical professional. The methods presented have achieved this aim. At this point, it is possible to measure a human's pulse and respiratory rate and also estimate the rhythm of their pulse and breathing using these methods. Similar to a medical profession, there will not be 100% accuracy in each case. However, the methods have proven that they are capable of making an initial assessment of two human vital signs representing health. In order to determine an overall snapshot of a person's health and compensate for any possible inaccuracies of the system, particularity in borderline cases between bradycardic, normal or tachycardic heart rate or slow, normal or fast breathing and indeed borderline cases of pulse or breathing rhythm, these measurement approaches will be supplemented with one further vital sign, namely CRT in Chapter 6.

5.5 Conclusion and Future Work

Methods for detecting, measuring and analysing two human vital signs, namely BPM and RR were presented. The methods presented replicate, to some extent,

the methods carried out by medical professionals when measuring these two vital signs and could be used to equip a first responder robot. A method for detecting a human's pulse by making contact with the radial artery and respiratory rate by making contact with the chest using a BioTAC robotic fingertip was presented. The calculation of the participant's BPM and RR was also completed. Using data collected from the BioTAC fingertip, the algorithms are able to determine whether a person has a regular heart rate, is bradycardic or tachycardic and whether the person has a slow, normal or fast RR. It is clear that accuracies similar to that of a medical professional, can be achieved for the calculation of BPM and RR when using the methods presented in this chapter, particularly when using a robust two stage noise reduction algorithm comprising of a low pass filter and a DWT wavelet based smoothing algorithm to firstly smooth the data and then a peak/ trough detection algorithm with a semi-automatic thresholding technique. Due to the nature of the data a fully automatic thresholding approach was found to be adequate to gather an estimate of the participant's BPM and RR but not for an accurate calculation, as it was proven to be less accurate. Furthermore, it was found that the addition of a third stage of filtering by means of lateral inhibition did not improve the accuracy of detecting peaks and troughs in the datasets. As it is not just BPM or RR that should be considered when assessing one's blood circulation and breathing, determining the time between pulses PPI and breaths PPI is also important, as this shows if the individual's pulse is regular or in a form of arrhythmia and if the person's breathing is regular or irregular. Arrhythmic beat rates can represent signs of disease.

The methods presented performed reasonably well for pulses and breaths recorded from the participants. However, due to the nature of the data collected an exactly accurate PPI and BBI can be difficult to calculate and therefore a tolerance for time intervals between pulse and breaths was applied. Furthermore, calculating the BPM and RR and classifying them to determine an indication of a person's health is only one element of being able to ascertain a person's current health status. Bringing the results of the calculated BPM and RR and the associated rhythm analysis together with other vital signs into an artificial intelligence algorithm that can determine an overall "first-responder" status of a human's health is the next step in having a complete automated health analysis system for emergency scenarios. This is explored in Chapter 6.

CHAPTER

SIX

Measurement of Capillary Refill Time and Determination of Health Status

6.1 Introduction

The assessment of a human's cardiovascular system is another measurement that can help determine their current state of health. One method of assessing the cardiovascular system peripherally is by assessing the Capillary Refill Time (CRT). Although it would be preferable to have more detail like the blood pressure reading of the human to assess their cardiovascular system, it is not always possible to get these readings, especially in cases of emergency. One approach to measuring CRT is to press a finger into the centre of the human's forehead for approximately 5 seconds and then release it. If the skin returns to its normal colour within 0.5-4.5 seconds (depending on age, sex, temperature etc.) then it can be assumed that the cardiovascular system is performing normally. However, in the majority of cases it should be under 2 seconds for a healthy human (King et al., 2014). If normal colour returns within the expected time period from the press, then the skin is getting a healthy supply of blood; if not it could be a sign that the body has gone into shock or has cut off the blood supply to the skin. The skin is the first organ that the body cuts blood supply off to in the event of severe harm or illness. Therefore, this chapter describes a method which computes CRT by using the Shadow Robot Hand and a BioTAC sensor to press against the participant's forehead with a safe, pre-calculated force for 5 seconds. Image processing techniques are used to determine how long it takes for their skin colour to return to normal, by using a micro 1000

Television Lines (TVL) camera and visual processing algorithms.

In a disaster situation, where there are numerous casualties, triaging care for such casualties is a huge task. Casualties need to be prioritised and sorted, based on their need for treatment and it is foreseen that robots could be an extremely useful aid in helping responders to triage victims in non-accessible places, hazardous environments and large scale accidents or disasters (Chang and Murphy, 2007). To date, there has been limited research in the development of algorithms that are capable of measuring vital signs in a disaster zone, although some research exists which is aimed at helping responders to triage victims. Saeki et al. (2006) present algorithms to measure pulse and calculate the victim's blood oxygen saturation degree (SPO2) using an infra-red sensor. As haemoglobin absorbs infra-red the absorption rate of the infra-red ray will change in relation to the increase and decrease of blood flow, making it possible to measure Beats Per Minute (BPM). Additionally, the absorption of the red ray enables the calculation of SPO2. Saeki et al. (2006) show that pulse was successfully measured with up to 97% accuracy. Asaoka et al. (2008) extend the work of Saeki et al. (2006) by assessing the use of an electrocardiogram (ECG) measuring device consisting of capacitive coupling electrodes for use alongside the infra-red pulse and SPO2 measuring sensor. It was found that ECG could be measured along with pulse however the measurement of SPO2 remained inaccurate due to cross talk between sensors. Wong et al. (2009) also present preliminary findings towards a robotic system that they are developing for autonomous evaluation of battlefield casualties. They present a novel algorithm using ultrasound sensors to detect fractures in human bones and investigated the use of infra-red imaging for surface wound detection. The work is preliminary but the authors state that with further development the algorithms could be used on a robot in battlefields to assess the current health status of injured soldiers.

This thesis aims to use the calculated BPM and Respiratory Rate (RR) in Chapter 5 and a measurement of CRT to enable a robot to assess a human's current health status in, for example, a home environment or emergency situation. With a clear assessment of these three vital signs it is possible to have a solid indication of a person's current health and assess their need for emergency intervention. Equipped with this knowledge, a first response robot could update paramedics prior to their arrival to a user's home or act as a triage assistant in an emergency situation. This chapter outlines the algorithm developed to accurately calculate a human's CRT (Section 6.2). Details of a fuzzy system designed

to classify the human's health status based on their calculated BPM, RR and CRT are also presented in Section 6.3. The results in this chapter demonstrate that it possible to accurately measure CRT and use this measurement together with BPM and RR as inputs to a fuzzy system to ascertain a human's current health status.

6.2 Determination of CRT

To establish if an accurate measurement of a human's capillary refill time can be calculated by analysing the change in skin colour as a result of a press action being carried out on the centre of the participant's forehead, the Shadow Hand was equipped with a camera. A customised camera mount that can clip securely onto the fingernail of a BioTAC fingertip was designed and built using a 3D printer. The customised camera mount can be seen in Figure 6.1. A small 1000 TVL camera was inserted into the mount and the video data was recorded on a PC by using a Universal Serial Bus (USB) video grabber.

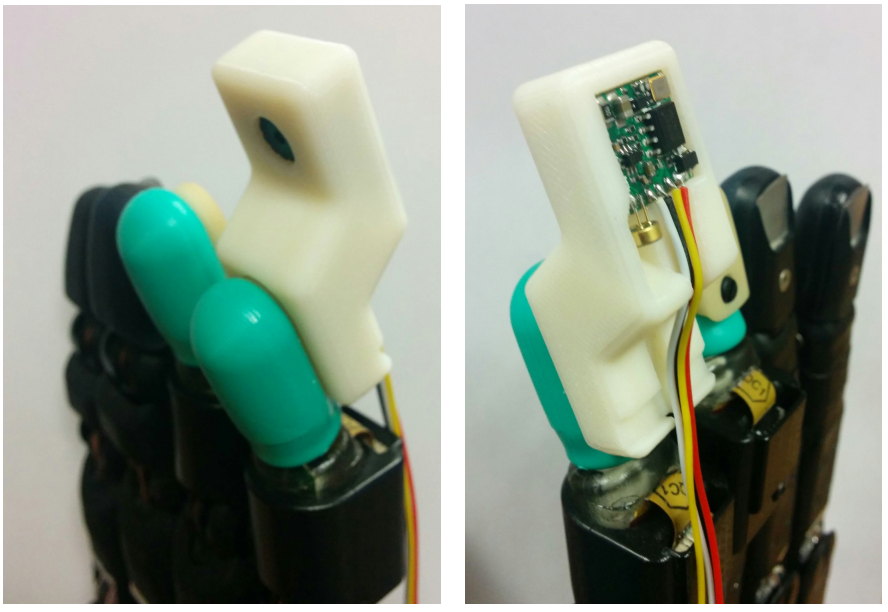

(a) (b)

Figure 6.1: Images showing the customised camera mount on the Shadow Hand from (a) the front and (b) the rear

6.2.1 Data Collection

Data collection involved the use of 12 healthy participants, as outlined in Section 5.2.1. participants were filtered according to the inclusion criteria, initially briefed and asked to complete a consent form. Each participant sat in a standard chair in front of the robot hand which was positioned very close to the participant's forehead. Data was collected at different times of the day meaning ambient light could have changed slightly from participant to participant. When video recording commenced, the region of interest (approximately $12cm^2$) on the forehead was captured for 5 seconds before the first finger of the Shadow Hand, equipped with the small 1000 TVL camera, was pressed against the centre of the participant's forehead for 5 seconds with a constant, painless force. The fingertip was then moved back to its starting position and video data of the area of interest on the participant's forehead was captured for a further 10 seconds. The short time before the fingertip applied pressure enables the camera to auto focus and capture the participant's natural skin colour so that it is possible to identify when their skin returns to its natural colour. Based on advice from a medical professional, 10 seconds was considered sufficient recording time after pressure as a CRT of anything more than 10 seconds was almost certainly a sign that the patient would be dead. An abnormal CRT (i.e. from 2-10 seconds) can be a sign of illness or that the body has gone into a state of shock. The applied force was measured using the ATI Nano17 6-axis Force/Torque (F/T) Sensor (ATi, 2017) from a trained medical professional mimicking the same procedure of measuring a human's RR. The impedance values measured by the array of electrodes on the BioTAC sensor were used to ensure that a constant force, similar to that of a medical professional, was applied in each case. At no stage was the participant's entire face or body filmed or recorded. A medical professional was consulted to verify that the action was completely safe and non-intrusive. There was a soft emergency stop in place to stop the robot hand from applying too much pressure on the participant at any time and furthermore the power could be cut instantaneously to the robot in case of emergency, posing very little risk to the participant at any time. This procedure was completed 3 times for each of the 12 participants.

6.2.2 Image Analysis

The videos were recorded at a frame rate of 30 frames per second (fps). The videos were split into still frames using the FFMpeg software (FFmpeg Develop-

ers, 2016) and imported into MATLAB (MATLAB, R2013) where the remaining analysis was completed. Figure 6.2(a) shows an image of a participant's forehead taken immediately after the press and shows the skin to be pale due to the capillaries being compressed and emptied and Figure 6.2(b) shows an image of the same participant's forehead as the capillaries begin to refill. This shows the skin to be much redder as it returns to its normal colour.

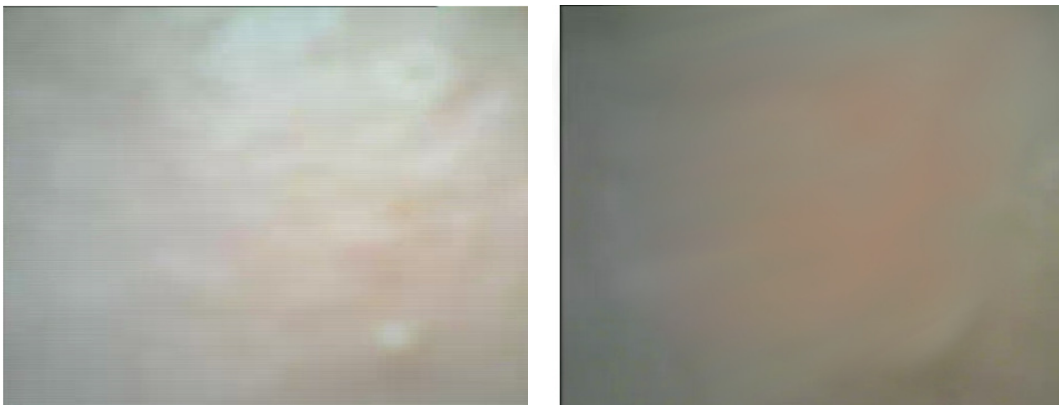

(a) (b)

Figure 6.2: a) An image of a participant's forehead taken immediately after the press; b) An image of the same participant's forehead taken as the capillaries begin to refill

The red, green and blue histograms were retrieved for each image per participant and the mean value of each colour's histogram calculated. A plot of the mean value for each colour histogram across a sequence of frames from one recording is shown in Figure 6.3.

As red is the most significant colour to signify the refill of the capillaries, the red pixel value is extracted from each recording and used for further analysis to determine the CRT. An image of the mean pixel value for red only is shown in Figure 6.4.

Prior to contact with the forehead it is evident that the average value of the red pixels is slightly higher than the average value post contact, phases 1 and 4 respectively, of the graph in Figure 6.4. This is due to shadows cast by the fingertip being close to the forehead causing the image to be darker than normal. Upon release of the fingertip from the forehead, it is expected that there would be an immediate drop detected in the red pixel value as the contact area is initially still whiter than normal due to the blood flow being temporarily stopped in the affected capillaries during contact, this is evident in phase 2 of the graph in Figure 6.4. In a healthy human, it is expected for this to be

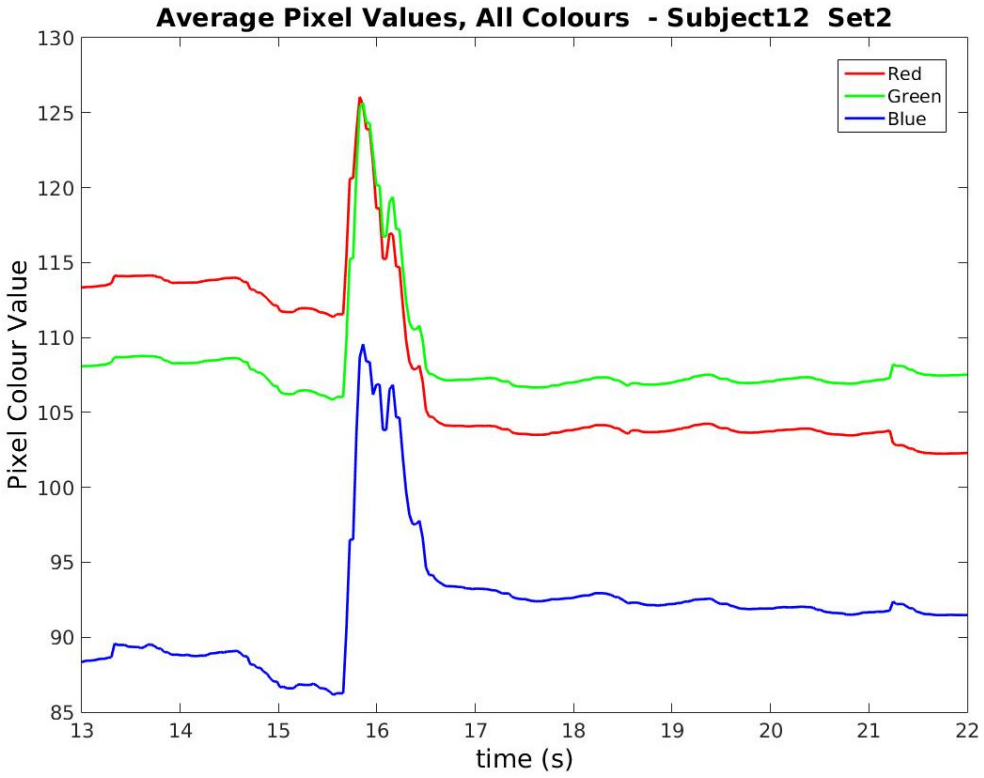

Figure 6.3: Graph showing the mean values of each histogram across a sequence of images

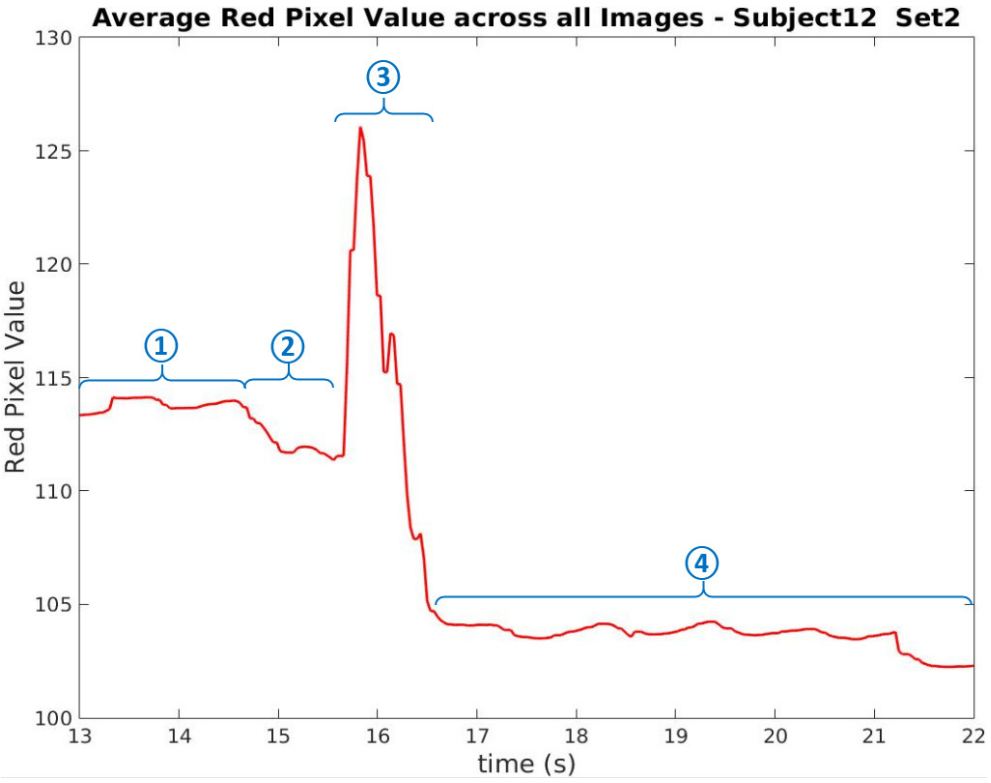

Figure 6.4: Graph showing the mean values of the red histogram across a sequence of images

rapidly followed by a rush of blood vessels to the area as the capillaries refill, resulting in a spike in the red pixel value, as witnessed in phase 3 of the graph Figure 6.4. The time from the instance that the skin regains blood flow (i.e. the beginning of phase 3) until the time it has settled at its original pigment (i.e. the beginning of phase 4) is the CRT. Phase 4 in Figure 6.4 shows that the skin appears to return to a steady colour where the red pixel value is lower than it was immediately before contact (in phase 1). This is due to the fact that the fingertip is now slightly further away from the forehead than it was when it was pressed against it, resulting in less shadows and ultimately a lighter colour being detected by the camera. Therefore, the exact time of transition from the drop in the red pixel value to the rise in the value of red pixels and the exact time when the skin settles, no longer changing colour, must be identified. Calculating the difference between these two times (i.e. the length of phase 3 in Figure 6.4) will result in an accurate measurement of CRT.

To identify the start and end times of the capillaries refilling, the graph is cropped to focus on the area surrounding the highest value of the red pixels. The time stamp of when the capillaries are being refilled (i.e. the highest peak) is calculated and the graph is cropped 5 seconds before and 10 seconds after to reduce the volume of data to analyse, hence increasing efficiency of the algorithm. In order to identify the time stamp when the spike in red pixel values started and ended, it was necessary to analyse the gradient of the graph at each time stamp. A sliding window was used to calculate the moving gradient along the graph using Equation 6.1 and each gradient and its corresponding time stamp were stored in an array for further analysis:

$$m_t = \frac{r_t - r_{t-1}}{T_t - T_{t-1}} \tag{6.1}$$

where m_t is the gradient at time t, r_t and r_{t-1} are the red pixel values at time t and $t-1$ respectively, T_t and T_{t-1} are the times at t and $t-1$ respectively.

To disregard insignificant gradients caused by noise and identify significant gradients, a dynamic threshold was calculated for each dataset. The threshold for identifying significant positive gradients was set as the mean of the positive gradients and the mean of the negative gradients was used as the threshold for identifying significant negative gradients. To compensate for the change in the average value of the red pixel before and after the press on the forehead, an average of the highest and lowest value of the red pixel is calculated. This value is taken as the mid-line of the red pixel value and is shown by the green line in

Figure 6.5. This mid-line was used as the baseline to demonstrate changes in gradient.

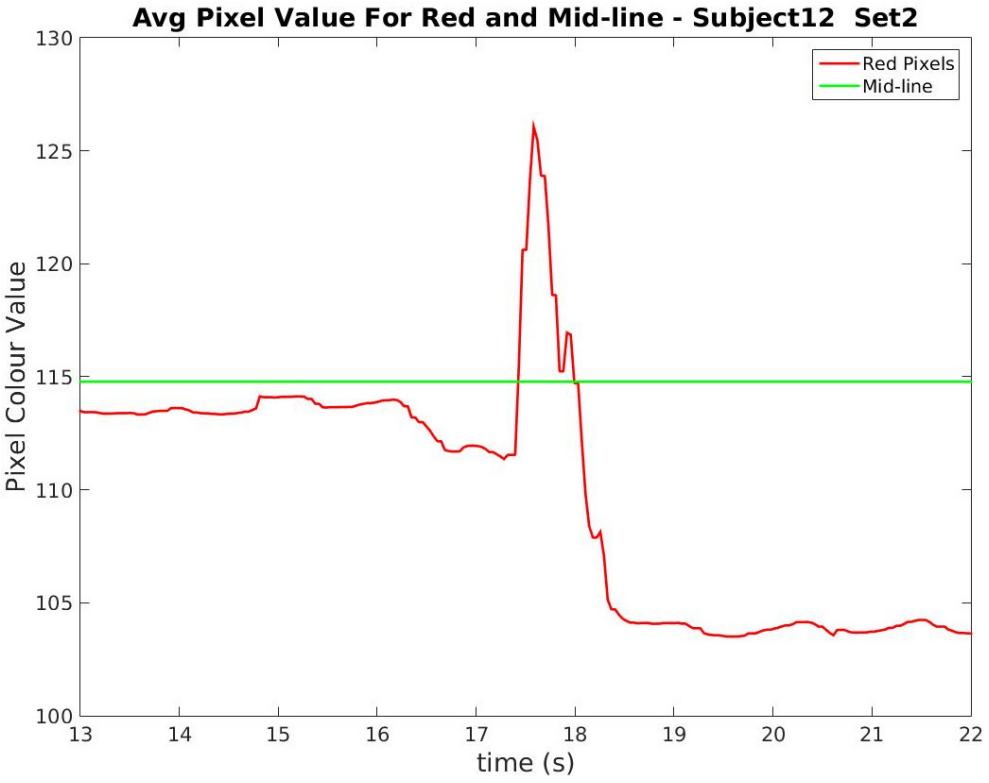

Figure 6.5: Graph showing the red pixel values and mid-line of the average between the largest and smallest values

Each identified significant positive gradient was represented as a positive step in the mid-line and significant negative gradient represented by a negative step, as seen in Figure 6.6. It is possible that artefacts in the red pixel graph mean a gradient which is larger than the threshold, but not of interest, is detected (illustrated by the dashed orange circles in Figure 6.6). In order to ensure these gradients are not considered, the gradients are analysed to identify periods where there is a series of gradient values consistently above the threshold (illustrated by the dashed purple circles in Figure 6.6). This enables identification of the significant positive and negative gradients of interest, i.e. indicating the start and end of the CRT.

The first period of consecutive positive gradients above the threshold is identified as the start of the time period where the capillaries are refilling with blood and the last period of consecutive negative gradients below the threshold is the end of the capillary refill time period (identified by the dashed, purple circles in Figure 6.6). Therefore the time stamp of one frame before the first period of consecutive positive gradients and after the last period of consecutive negative

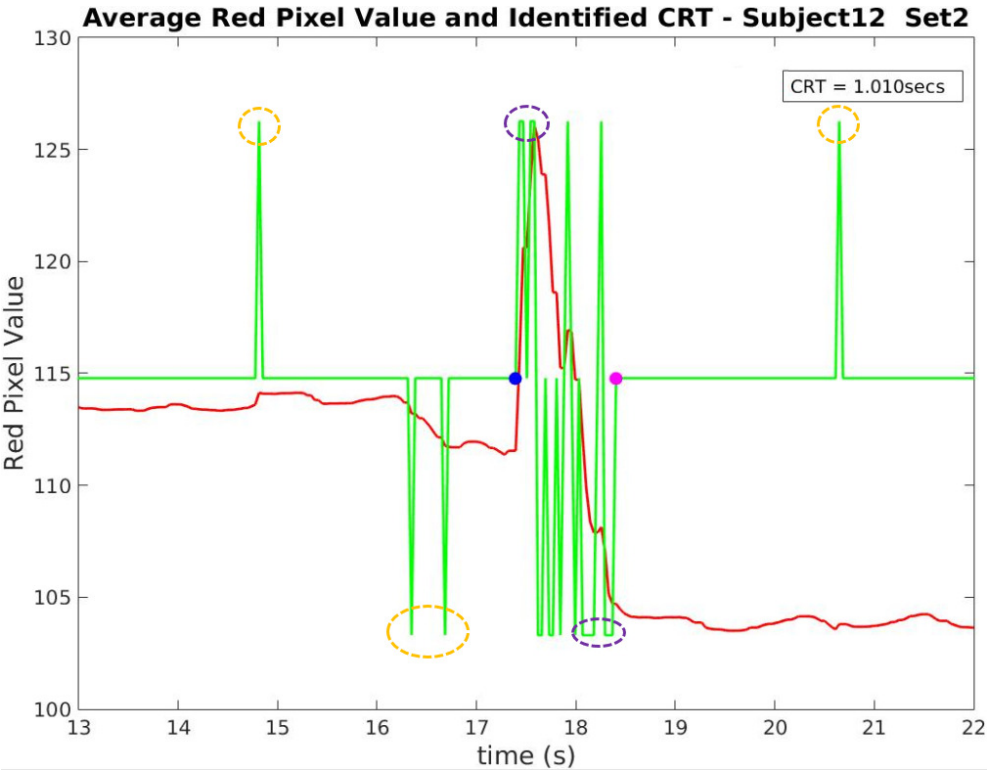

Figure 6.6: Graph showing the red pixel values and the identified significant gradients

gradients is identified. These are represented by the blue and magenta coloured dots respectively in Figure 6.6. The time difference between each instance is calculated and represents the CRT of the participant. The CRT is calculated for each of the three data sets collected for all 12 participants.

6.2.3 CRT Results and Discussion

This section presents results for the experiments calculating the CRT from 12 healthy human participants of varying skin tone. As there is no medical method for calculating a precise value of CRT, a medical professional verified that all participants were healthy and their CRT was below the expected duration of 2 seconds. Table 6.1 analyses the results of the calculated CRT following 3 sets of video data collected for each participant. The average, minimum and maximum calculated CRT in seconds of the 3 sets are shown for each participant. Also, the number of sets which correctly calculated the CRT as taking less than 2 seconds is stated for each participant. All of the calculated CRT values for each set and participant can be seen in Table B.1 in Appendix B. In some cases, for example if the participant is elderly or an infant, the CRT can be as high as 4.5

seconds. However, generally speaking the majority of people should have a CRT of no more than 2 seconds according to a medical professional and the (Royal College of Physicians of London, 2012). Since there were no elderly or infant participants assessed, 2 seconds is used as the threshold to determine if participants are healthy or in a state or shock or a critical condition.

Table 6.1: Table outlining the calculated CRT experimental results

Participant	**Average (*s*)**	**Min (*s*)**	**Max (*s*)**	**Sets** $< 2secs$
1	0.976	0.909	1.082	3
2	0.739	0.551	0.842	3
3	0.869	0.681	0.995	3
4	1.117	0.976	1.222	3
5	1.421	1.085	1.877	3
6	1.715	0.759	3.554	2
7	1.001	0.940	1.121	3
8	1.081	0.875	1.264	3
9	3.772	1.091	6.983	1
10	0.988	0.908	1.121	3
11	2.362	0.978	5.019	2
12	1.111	1.010	1.309	3

As shown in Table 6.1 the CRT was accurately calculated and correctly determined as less than 2 seconds in 32 of the 36 ($\approx$ 89%) tested video data sets. The video data for participant 9 proved to be the most difficult from which to accurately calculate the CRT, with two of the datasets being calculated as greater than 2 seconds. One of the sets was as high as almost 7 seconds and was a particularly noisy dataset which contained numerous prolonged positive gradients. These spikes in the red pixel value could be caused by an unexpected change in ambient lighting or a shaking of the camera during recording. However, in the majority of instances the values calculated are within the expected range of 0.5-2 seconds for healthy participants of varying skin colour, including Caucasian, Black and Indian. Therefore, the algorithm proved to be robust regardless of skin colour.

6.3 Triage Health Status Classification

To date, the majority of research in relation to robots being utilised in disaster zones has focused on being able to search the zone for survivors and determine safe routes to exit. Teleoperated robots that are able to move around disaster

sites collecting and transmitting data have been a common focus for researchers. However, methods and robots discussed in literature to date that are used to searching for victims, are not capable of any physical interaction with humans when identified. Furthermore, regardless of how a survivor is identified in a disaster zone there has been little work on the physical interaction with a human, for example, to release them from rubble or to use a robot to carry out a medical assessment of the survivor in situ. Samani and Zhu (2016) present a mobile robotic ambulance called "Ambubot", that is capable of transporting and using an automated external defibrillator (AED) on victims within a smart city either by manual teleoperation or fully automated operation. The mobile vehicle is equipped with numerous sensors standard to that of a mobile robot such as two high resolution video cameras, sonar sensors and laser scanners. Although an effective and potentially very useful robot for rapidly deploying an AED to patients who have just had a cardiac arrest in the city, there were some restraints with the autonomous use and mobility; adding omnidirectional mobility to the robot would help improve it. Furthermore, the robot requires a "smart city" infrastructure in which to operate, to provide the locations of people in need of an AED. Murphy et al. (2013) investigated the use of robots to interact with trapped victims in terms of four different schemes: one-way video with no audio (from the robot at the victim back to responders), two-way video with no audio, one-way video (from robot to responders) with two-way audio and two-way video with two-way audio. Although communication was achieved between responders and a victim in a simulated building collapse, the authors identified key areas that require improvement for communication between victims and responders, including transparency of robot state and minimalistic interfaces. Even with this level of communication it would be difficult to carry out remote assessment of the victim's current health status, particularly if the victim is unconscious. Therefore, a system that could carry out an assessment of of a participant's vital signs and enable triage of victims would be extremely useful in a disaster scenario.

Algorithms capable of using data collected from a Shadow Hand equipped with BioTAC fingertip sensors to determine a human's BPM and RR were presented in Chapter 5 and an approach to determining a human's CRT was presented earlier in this chapter. It is necessary to appropriately combine these vital signs to determine an overall health status of the human. A fuzzy classification system (Cios, 2001) was determined to be the most appropriate approach due to it having fuzzy boundaries between classes enabling it to handle noisy and inconsistent real data. This is described in the next section.

6.3.1 Fuzzy Classification Methodology

As outlined in Chapter 3, fuzzy sets have the capability to model uncertainly and slight inaccuracies within the reasoning process (Zadeh, 1965); accordingly a fuzzy classification algorithm was determined to be the most effective approach for classifying a human's health status based on the three vital signs discussed in this thesis. Fuzzy systems aim to model the human reasoning system, which Pal and Mandal (1991) state is approximate rather than precise in nature. Fuzzy logic systems have been used for numerous applications ranging from process control to medical diagnosis (Pal and Mandal, 1991; Ali et al., 2011; Dennis and Muthukrishnan, 2014; Nguyen et al., 2015). Other classification algorithms such as Artificial Neural Networks (ANN) and Support Vector Machine (SVM) were evaluated for classifying the measured vital signs data. However, due to the nature of vital signs data having overlapping boundaries for which a human is deemed "healthy", fuzzy logic approaches were determined to be the most suitable choice for classifying human's health status from the vital signs calculated via the methods outlined in this thesis. A medical professional advised that there was a finite number of possible outcomes of health status when measuring vital signs in a disaster zone. These possible outcomes could be written as rules within a fuzzy logic system. The widely accepted Mamdani fuzzy system is suited to human style input (in this case a reading of a vital sign) and the output of a Mamdani-type fuzzy system can be easily transformed to a linguistic form in comparison with a Sugeno-type fuzzy system (Blej and Azizi, 2016). Therefore, a standard Mamdani fuzzy system (Mamdani, 1974, 1977) was selected. A Mamdani system defines a function, f, which generates numerical outputs $y = f(x)$ from numerical inputs, x, by using a set of IF/THEN rules (Zimmermann, 2001). In this case the numerical inputs are the calculated BPM, RR and CRT values and the numerical output refers to a specific health status. In order to allow for some cases where the numerical value for one or more of the vital signs may be borderline between two classes it is necessary to have some overlap in the membership functions. Furthermore, there may be cases where the person is extremely healthy and naturally has a lower BPM or RR. Gaussian membership functions have been found to perform well for similar applications due to their smooth curved edges and style of overlap (Hameed, 2011) and therefore will be used in the fuzzy logic system in this approach.

The rules of the fuzzy logic system were determined based on the advice of a medical professional who determined possible status' of health based

on the measurement of BPM, RR and CRT in an emergency scenario and by referencing (Royal College of Physicians of London, 2012), which is the National Health Service (NHS) standard for the assessment of acute illness and severity. Graphs displaying the membership functions for each input are shown in Figure 6.7. The details of the membership functions for each of the inputs and their approximate ranges are shown in Table 6.2. The overlaps presented in the table allow for some abnormal readings of BPM and RR within reason.

Table 6.2: Table outlining the details of the Input Membership Functions

Input	**Membership Function**	**Range**
BPM	Zero	0-2
	Low	1-63
	Normal	50-110
	High	97-240
RR	Zero	0-2
	Below Average	1-13
	Normal	7-25
	Above Average	20-80
CRT	Normal	0-2.5
	Prolonged	2-11
	Infinite	10-60

The aim is to determine a participant's health by monitoring their BPM and RR over a 60 second period and taking one measurement of their CRT rather than continually monitoring their vital signs over a longer period of time. Therefore, there are 9 possible outcomes that can be determined in an emergency type scenario. The 9 outcomes were represented by triangular membership functions. As there were possible combinations that would not represent one of the 9 possible diagnoses', there was a tenth membership function included for all non-classified combinations, including unrealistic values of the vital signs that may have been caused by sensor error, for example. A graph displaying the output membership functions is shown in Figure 6.8. The MATLAB Fuzzy Logic Toolbox (2013) was used to develop the fuzzy algorithm, which includes 5 defuzzification methods. As it is required that the most likely output from the combination of vital sign inputs is selected, the 'centroid' defuzzification method was used. This method returns the centre of the area underneath the curve of the fuzzified outputs. It is the most common and effective method for converting the result to a crisp output (Naaz et al., 2011). The returned centroid

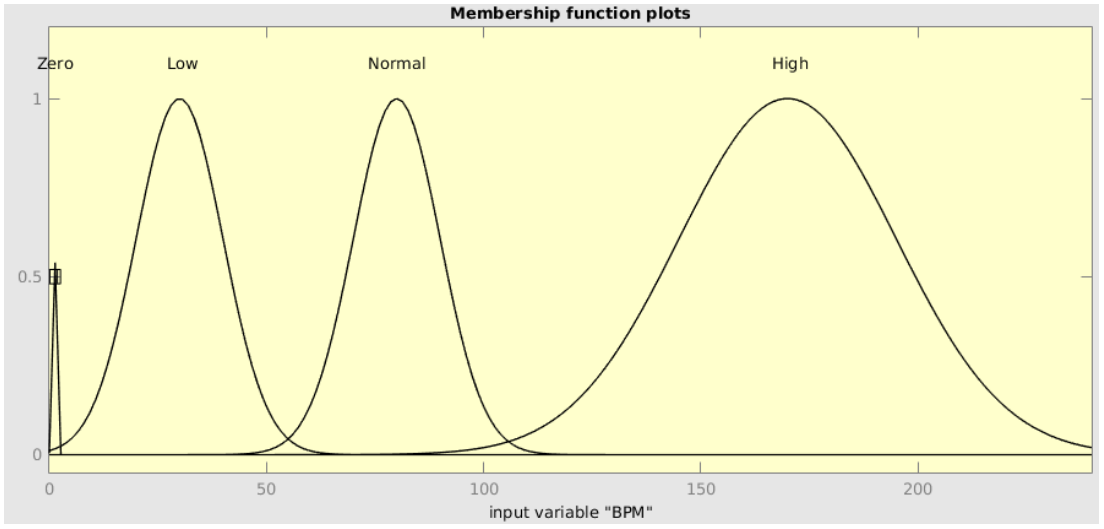

(a)

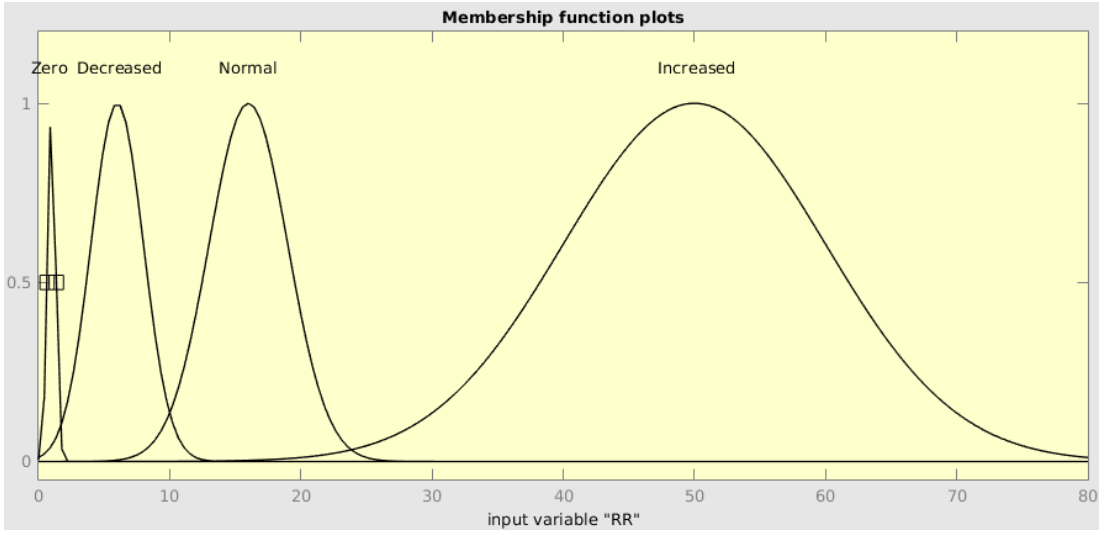

(b)

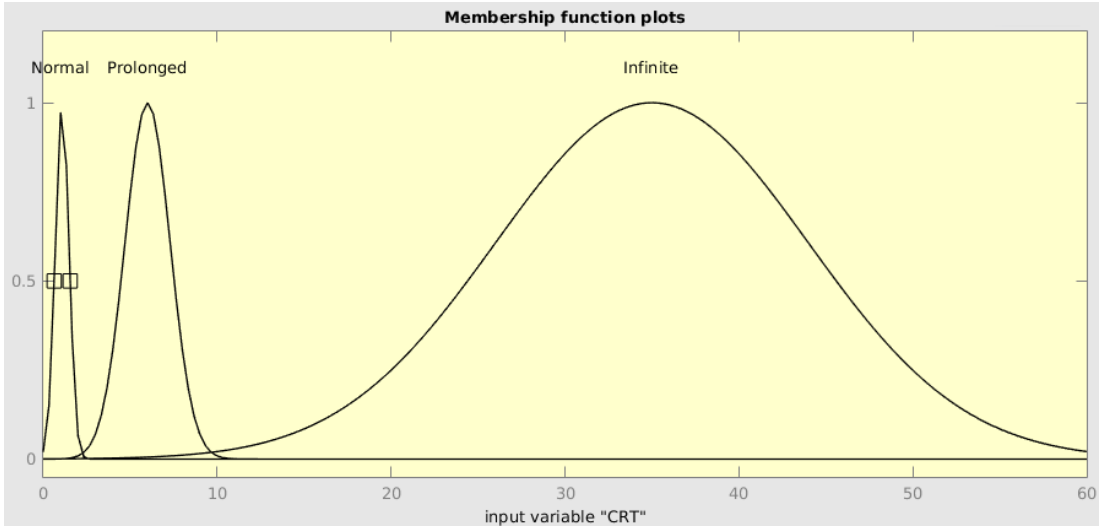

(c)

Figure 6.7: Graphs displaying membership functions for a) BPM; b) RR; c) CRT

value is rounded to the smallest integer greater than or equal to the centroid value. Table 6.3 shows pseudo code of the fuzzy rules related to the membership functions outlined in Table 6.2, the output integer related to each rule and a description of what each output represents in relation to the participant's health status.

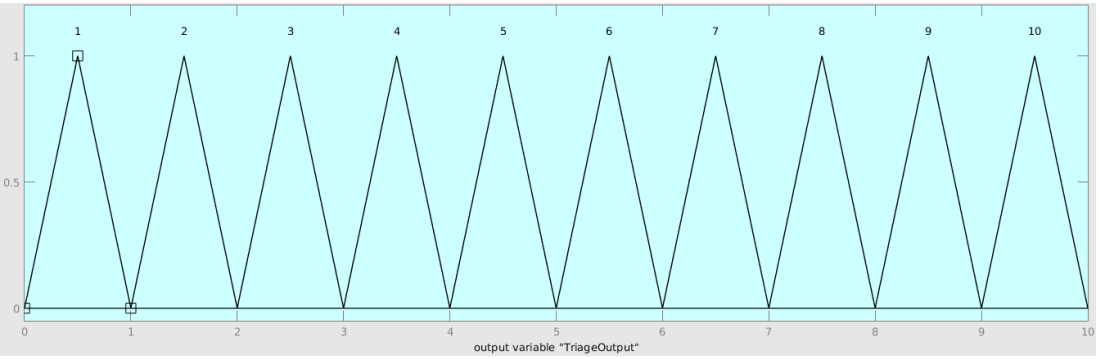

Figure 6.8: Graph showing the membership functions for the outputs of the Fuzzy System

Table 6.3: Table outlining the Outputs of the Fuzzy Logic System

Fuzzy Rule	**Output**	**Description**
If (BPM is Normal) and (RR is Normal) and (CRT is Normal)	1	Healthy
If (BPM is Low) and (RR is Normal) and (CRT is Normal)	2	Heart Block / Fit
If (BPM is Low) and (RR is Below Average) and (CRT is Normal)	3	Unconscious / Sleep
If (BPM is Normal) and (RR is Above Average) and (CRT is Normal)	4	Acute Deterioration
If (BPM is High) and (RR is Above Average) and (CRT is Normal)	5	Pain / Anxiety
If (BPM is High) and (RR is Below Average) and (CRT is Normal)	6	Central Nervous System (CNS) Depression / Traumatic brain injury (TBI) (Bang on Head)
If (BPM is High) and (RR is Above Average) and (CRT is Prolonged)	7	Hypovolemic shock / Open Wounds / Bleeding Out
If (BPM is Low) and (RR is Below Average) and (CRT is Prolonged)	8	Critical (close to death)
If (BPM is Zero) and (RR is Zero) and (CRT is Infinite)n	9	Dead

6.3.2 Fuzzy Classification Results and Discussion

To evaluate the fuzzy logic classifier synthetic data were used, consisting of 10,000 datasets of BPM, RR, CRT for each possible output. Simulating the output of the BPM, RR, CRT algorithms presented in Chapter 5 and Section 6.2, the values for each vital sign were generated using a pseudo-random number generator limited between the ranges for each sign as outlined in Table 6.2. For example, a range of values representing BPM were pseudo-randomly generated over the intervals 1-63, 50-110 and 97-240 to represent low, normal and high BPM respectively. There was a total of 90,000 (10,000 x 9) datasets created, representing all possible outcomes and ensuring that there were sufficient datasets which included values in the overlapping areas of the membership functions. As the synthesised dataset contained combinations of pseudo-randomly generated data to fulfil one of the 9 possible outcomes, it was possible that it would differ from the real collected data as there could be misreadings (due to sensor error) in the real data causing a combination that was not necessary to be included within the synthetic dataset. Furthermore, the synthetic dataset was generated based on what BPM, RR and CRT readings that are perceived as "normal" or "abnormal" by medical professionals. However, in reality it is possible that a human could have vital signs outside of the expected boundaries and still be perfectly fit and healthy. As this is not common, the synthetic dataset did not have data representing these profiles. The datasets were randomised, split into 5 parts and with 4 parts training one part testing as input into the fuzzy system. The output generated for each of the 5-folds was compared against the expected output and an average of the 5 validation accuracies was calculated, representing the percentage accuracy of the fuzzy logic classifier for synthetic data.

Following validation of the fuzzy logic system, the data collected from the participants was organised into the same format as the synthetic data, i.e. into datasets containing a calculated BPM, RR and CRT for each set of data collected per participant.

The average 5-fold validation percentage accuracy of the fuzzy logic system for classifying the synthetic datasets was 95.3%. The inaccuracies occurred where there was more than one vital sign in an overlap area of the membership functions. Considering the high performance of the classifier and the understandable reasons for any inaccuracies, the classifier was also tested with real participant data. The participant data were input into the fuzzy system and

evaluated in a similar manner to that of the synthetic data.

The percentage accuracy of the fuzzy logic system for classifying the vital signs calculated from the participants was 72.2%. Although this is considerably lower than the accuracy when classifying synthetic data, it is important to note that there were only 36 datasets from human participants in comparison with 90,000 synthetic datasets, meaning each incorrect classification has a greater effect on the overall accuracy percentage. As the data being classified by the fuzzy logic system was the outputs from the BPM, RR in Chapter 5 and CRT in Section 6.2, then some of the incorrect classifications are cumulative errors. For example, if the BPM, RR or CRT or more than one of them was incorrectly computed then it will not be possible for the fuzzy logic system to correctly classify the participant's health based on incorrect vital sign data. Considering that the accuracies of the algorithms were 97.22%, 91.67% and 88.89% when classifying what status their BPM, RR and CRT was respectively, then it is expected that the inaccuracies from these algorithms would cumulate towards inaccuracies during fuzzy logic classification. Furthermore, all 12 participants were healthy and included some very fit participants. Therefore, there were cases where the participants had as low as 6-7 breaths per minute and a BPM of under 60. This meant that at least two of the vital signs were outside what is considered to be normal for an average person. Unfortunately, the system cannot deal with outliers at this time due to lack of previous knowledge about the participant. It is expected that there will be exceptions which mean that some peoples vital signs lie outside of the expected boundaries even though they are perfectly healthy, however they would be exceptions rather than rules. In a disaster zone, if the system were to encounter any of these exceptions, it would merely result in the person being rescued earlier than perhaps needed, which is not a negative outcome. There is no information provided to the system to inform it if the participant is fit and thus it is normal for them to have a lower than average BPM and RR. Furthermore, it is important to reiterate that the assessment of each participant's health is being made from a short, one-off, 60 second monitor for BPM and RR and one measurement of CRT rather than continuous monitoring of their health over a prolonged period of time. Therefore, if the datasets containing such outliers were removed from the fuzzy classification, the accuracy of the fuzzy logic system when classifying the health status of the participants increases to 83.9%. Considering the data for CRT was collected at different times of the day producing different ambient light conditions and from a range of skin colours, the algorithm has proven to be robust. Although the overall accuracy of the fuzzy classification system is

lower when classifying participant data than synthetic data, an effective system to classify human health status in an emergency scenario based on a one-off assessment of BPM, RR and CRT has been developed.

6.4 Conclusion

This chapter presented an algorithm capable of determining a third vital sign of human health, namely CRT. A human's CRT should normally be less than 2 seconds if they are in a healthy state. The algorithm used tactile sensing data for control of the BioTAC fingertip and a camera to collect vision data which was later analysed to determine the duration of time lapsed before a participant's skin colour returned to its normal tone. The algorithm proved to be effective and robust across a range of skin tones, determining a correct measurement of CRT in 32 of the 36 participant datasets.

This chapter also presented a fuzzy logic classifier which utilises the three vital signs (BPM, RR and CRT) measured by the methods outlined in Chapter 5 and Section 4.2.1 of this chapter and determines an overall classification of health. The outputs of the fuzzy logic classifier was developed using the knowledge of a medical professional and by referring to the NHS standard for the assessment of acute illness and severity document (Royal College of Physicians of London, 2012). The classifier was evaluated for robustness with synthetic data initially and was then evaluated for its effectiveness to classify participant data. Although the classifier did not perform as well when classifying real data collected from the participants as it did when classifying synthetic data, it still proved to be an effective classifier capable of determining a human's health status from just one assessment of BPM, RR and CRT. This system could be used as part of a robotic triage system in an emergency scenario and play a key role in prioritising victims in an emergency situation.

CHAPTER

SEVEN

Conclusions and Future Work

Interest in the use of tactile sensing in artificial systems has grown considerably since the development of sophisticated multi-modal tactile sensors such as the BioTAC Biomimetic fingertip. This thesis focuses on the use of machine learning techniques and tactile sensing technology to perform tasks similar to those humans can complete due to their sophisticated tactile sensing capabilities, such as material identification and reading a human's vital signs. A brief description of human tactile sensing is provided in Chapter 2 emphasising its complexity, enabling humans to carry out integrate tasks which require sophisticated dexterity and tactile feedback. This outline demonstrates how difficult the human tactile system is to replicate, as is evident by the fact that sophisticated tactile sensors have only been developed in recent decades. An overview of such sensors and types of tactile sensor technologies is also provided in Chapter 2. Specifically a detailed introduction to the multi-modal tactile sensor which is used throughout this thesis, namely the BioTAC^{TM} biomimetic finger-shaped tactile sensor from Syntouch® (Syntouch, 2013), is provided.

Chapter 3 focuses on research which utilises tactile data collected from the tactile sensors outlined in Chapter 2. In particular, this chapter provides an overview of computational intelligence methods which have been utilised in applications using tactile sensing data. One such application is the classification of materials, for which an overview is provided and some of the ongoing challenges in the area highlighted. Classifying between objects of similar compressibility and/ or surface texture was highlighted as an ongoing issue and is one which is addressed by the methods developed for material classification in Chapter 4. Chapter 3 also provides an overview of key artificial intelligence based applications for which the BioTAC sensors have been utilised to date. This research has outlined that the BioTAC has not yet been utilised to measure human vital signs or to assess human health in disaster zones or following an

emergency. Therefore, this motivated the direction of this thesis. However, it was first necessary, to ascertain the capability of the BioTAC sensor by completing a task such as material classification in Chapter 4. Following the success of such a challenging task, it was decided to use the BioTAC sensor to measure human vital signs. This work is presented in Chapter 5 and Chapter 6.

A machine learning approach to material classification is presented in Chapter 4. This is capable of successfully classifying materials, including those which have similar compressibility and surface texture. Vibration and thermal data were collected relating to the surface texture and thermal conductivity of the materials respectively. Principal component analysis (PCA) was applied to extract features from the data and an evaluation of machine learning techniques including Support Vector Machine (SVM), Artificial Neural Networks (ANN), Gaussian Mixture Model (GMM), Linear Discriminant Analysis (LDA), Naïve Bayes (NB), *k*-Nearest Neighbour (*k*-NN) and Multi-Layer Perceptron (MLP) was completed. A novel hybrid combination of an SVM and ANN was also evaluated for its capability in the task of material classification. A two-stage SVM approach was found to perform best for material classification based on vibration and thermal based data. Performance evaluation involving human participants classifying the same set of materials was also presented in Chapter 4. The performance of the participants when attempting to classify the materials using only their sense of touch is presented. The machine learning techniques were compared against human performance. It was found that all of the machine learning techniques outperformed human performance; in fact the two-stage SVM approach outperformed humans by over 16%. Although the learning algorithms outperformed human performance in terms of accuracy, the algorithms require training and are therefore still slower than the adult participants.

Chapter 5 presents an overview of methods in the literature to measure human vital signs. Two vital signs that can be used to represent a human's health status are heart rate in Beats Per Minute (BPM) and Respiratory Rate (RR). Common methods in the literature for measuring these vital signs include the use of the Doppler effect, wearable sensors and vision based techniques. However, it would not be possible to depend on these techniques in a disaster zone or in the event of an emergency. Chapter 5 presented methods that were developed to measure a human's BPM and RR from tactile sensing. The method developed to measure BPM replicates the procedure carried out by medical personnel when measuring a human's pulse from their radial artery at the wrist. The method

presented for measuring RR aims to improve upon the current method used by medical personnel which involves watching the chest wall and counting the breaths taken in one minute. The method presented in this thesis uses tactile sensing to measure both vibration and changes in thermal properties to identify when a breath is taken. Furthermore, both methods determine the interval between each heart beat and breath and analyse it to determine if the human is in sinus rhythm or some form of arrhythmia and if they are breathing regularly or irregularly. Both methods use a third-order low bandpass filter and the application of wavelets to smooth the data prior to pulse and breath detection. Following ethical approval, data were collected from 12 healthy human volunteers using the Shadow robot Hand fitted with the BioTAC tactile sensors. The experiment was overseen by a medical professional and the performance of the developed methods was evaluated against groundtruth vital sign measurements conducted by the medical professional on each participant. It was determined that the method developed for analysing a human's heart rate could accurately measure a human's BPM and determine if the participant had a regular heart rate ($60 - 100$BPM), was bradycardic (< 60BPM) or tachycardic (> 100BPM). The method proved to be able to successfully determine if the participant was in sinus rhythm or some form of arrhythmia. The method developed to analyse a human's breathing proved capable of accurately determining how many breaths per minute were being taken by the participants and if they had a below average, average or above average RR. Furthermore, the method could determine if the participant had a regular breathing rate. Both methods required the use of a semi-automatic threshold which was tuned for each participant. Using a fully automatic threshold which did not require tuning did not produce the same level of accuracy in terms of a specific measurement of their exact BPM and RR. However, the fully automated method is viable, as it was able to determine the class of the participant's BPM and RR and could be a rapid method for determining two vital signs in a disaster zone without requiring previous knowledge about the victim's health.

A method to measure a third human vital sign is presented in Chapter 6. Capillary Refill Time (CRT) is the length of time it takes for the capillaries to refill in the centre of a person's chest, fingernail or forehead following pressure being applied by one's fingertip to prevent blood flow in the area. The CRT for an average healthy adult should be approximately 1 second but can be anything from 0-2 seconds. It can take as long as 4.5 seconds for an infant or elderly person, however even in variations of age it is normally a maximum of 2 seconds for a healthy individual. A time longer than 2 seconds can be an indication that

the body has gone into a state of shock or is in a critical condition. Chapter 6 presents a method which uses tactile sensing feedback to control the movement of the BioTAC fingertip and press it into participants' foreheads with a force measured from a medical professional when applying the same technique. A custom 3D printed mount attached a camera to the fingernail of the BioTAC fingertip enables recording of video footage of a small region of interest on the forehead where the press was applied. The video footage was split into images and image processing techniques were utilised to split the images into three colour histograms; red, green and blue. The red colour was analysed and a novel algorithm was developed to identify the start and end of the time period where the participants' capillaries refilled with blood. This method proved to correctly identify the time period in almost every dataset collected from the participants of varying skin colour, despite slight variations in ambient lighting. The capability to measure human vital signs using tactile and vision sensing could be extremely beneficial to assistive robots used in disaster or emergency scenarios. Therefore, a review of robotic systems used to assist humans in disaster zones was also presented in Chapter 6. A method for classifying a human's health status following accurate measurements of three vital signs, namely BPM, RR and CRT was presented. A fuzzy logic classification algorithm was utilised to classify the human's health status into one of nine possible classes based on the available vital signs and no historical knowledge of the person's health. These nine states of health were determined in collaboration with a medical professional and by consulting guidance documents of the (Royal College of Physicians of London, 2012). The Fuzzy Logic algorithm was evaluated with both synthetic and real data collected from the participants and proved to be an effective method of classifying a human's health status based on one assessment of their BPM, RR and CRT. Being able to remotely assess a human's health status by physical interaction of a victim with a robot system following a disaster or emergency would allow triage of all victims to take place and determine who is in most need of help. In turn, this could prove to be life saving for victims of the disaster and indeed help reduce the risk to the lives of emergency service workers.

7.1 Summary of Contributions

This thesis has presented a review of the state of the art in tactile sensing technology and algorithms. The key contributions in this work are:

- An evaluation of numerous classification algorithms and novel combinations of classification algorithms for material classification using tactile data.
- An evaluation of human performance for classifying materials via touch alone. It was evident that knowledge of surface texture played a key role for humans when identifying materials, as the task proved much more difficult when assessing only the material's compressibility and thermal properties.
- A novel method for material classification using tactile data, capable of classifying materials of similar compressibility and surface texture and outperforming human performance.
- The use of a robot to mimic medical procedures in order to accurately measure and analyse human BPM and heart beat rhythm via tactile sensing.
- The use of a robot to accurately measure and analyse human RR and breathing rhythm via tactile sensing, rather than a crude vision-based method used by medical personnel.
- Accurate measurement and analysis of human CRT via complementary use of robotic tactile sensing-based control and a micro 1000 Television Lines (TVL) camera.
- The ability to ascertain a human's health status by using a fuzzy based classification system to assess the measured BPM, RR and CRT.

7.2 Future Work

This thesis has provided a substantial body of work in the field of tactile sensing. However, there remains a considerable amount of work in the field of tactile sensing and in particular in the use of artificial intelligent systems carrying out human health assessment in disaster zones or emergencies. There are two main directions in which the work outlined in this thesis could be extended to further the robotics community.

7.2.1 Object Recognition and Grasping

Although methods for object and material identification using vision have been heavily researched, the tactile sensing based material classification method presented in Chapter 4 could be used in collaboration with vision based methods. If an object was identified using image processing techniques and an estimate of the physical size of the object is determined then the volume of the object can be calculated. The tactile sensing methods presented in Chapter 4 could identify the material from which the object is made and armed with the volume of the object, an estimate of the object's weight can be calculated. The incorporation of vision would further strengthen the identification of objects and materials. To train a robotic system on a vast array of objects and incorporate vision, a significant dataset of tactile data, static image and video data should be collected for numerous materials, objects, clothing and human skin. A deep learning structure could then be utilised for the robotic system to learn the vast dataset of materials and objects. This information could be used to help determine the effort and grasping method required to successfully lift previously unlearned objects. This would provide a useful skill to assistive robots in a home environment when learning the affordances of objects they have not previously encountered. It could also be used in a disaster zone when determining debris entrapping a human or when attempting to remove an object that may be preventing access to a trapped person's arm or head preventing assessment of their vital signs. For example, if a piece of debris is occluding a victim's arm, the robotic system could determine the size of the debris, what material the debris consists of and estimate its weight. This would enable to the robot to determine how much force and with which pose it should apply to lift and remove the debris, thus clearing access to the humans wrist in order to measure their pulse.

7.2.2 Extension of Assistive Robot Based Triage

The work in this thesis focussed on using the BioTAC fingertip to replicate the role of medical personnels' fingertips when assessing human vital signs. Collecting Electromyography (EMG) data from the arm of medical personnel when conducting standard medical assessments would provide useful knowledge and inform researchers on the correct kinematics for the control of robot arms and hands to conduct similar medical assessments. These methods, coupled with extensive knowledge of materials and objects, could be used to help a

robotic system guide a fingertip to the wrist, chest and forehead of a trapped victim and proceed to measure their vital signs. Although some methods have been presented in the literature to identify trapped persons in a disaster or emergency zone, combining tactile sensing with vision to firstly confirm victims in an emergency environment and secondly conduct a medical assessment of them, could prove to be very effective.

The fuzzy classification system utilised in Chapter 6 to classify an overall status of health considered only BPM, RR and CRT. The extension of this algorithm could include the consideration of the calculated Pulse to Pulse Interval (PPI), Breath to Breath Interval (BBI) and other vital signs. In order to consider these factors, the artificial system would require extensive medical knowledge and be trained in making intelligent observations of PPI and BBI data.

REFERENCES

Abe, S., 2012. Neural Networks and Fuzzy Systems: Theory and Applications. Springer US.
URL https://books.google.co.uk/books?id=1VLaBwAAQBAJ

Ali, A., Shamsuddin, S., Ralescu, A., Visa, S., Dec 2011. Fuzzy classifier for classification of medical data. In: 2011 11th International Conference on Hybrid Intelligent Systems (HIS). pp. 173–178.

Allen, J., 2007. Photoplethysmography and its application in clinical physiological measurement. Physiological Measurement 28 (3), R1–R39.

Almassri, A., Hasan, W., Ahmad, S., Ishak, A., Ghazali, A., Talib, D., Wada, C., 2015. Pressure sensor: State of the art, design, and application for robotic hand. Journal of Sensors 2015 (846487), 1–12.
URL https://doi.org/10.1155/2015/846487

Alonso-Martín, F., Gamboa-Montero, J., Castillo, J., Castro-González, A., Salichs, M., 2017. Detecting and classifying human touches in a social robot through acoustic sensing and machine learning. Sensors 17 (5).
URL http://www.mdpi.com/1424-8220/17/5/1138

Arian, M., Blaine, C., Loeb, G., Fishel, J., Feb 2014. Using the biotac as a tumor localization tool. In: 2014 IEEE Haptics Symposium (HAPTICS). pp. 443–448.

Asamura, N., Yokoyama, N., Shinoda, H., Nov 1998. Selectively stimulating skin receptors for tactile display. Computer Graphics and Applications, IEEE 18 (6), 32–37.

Asaoka, T., Kanaeda, Y., Magatani, K., Aug 2008. Development of the device to detect human's bio-signals by easy sensing. In: 2008 30th Annual International Conference of the IEEE Engineering in Medicine and Biology Society. pp. 526–529.

ATi, 2017. Ati f/t sensor: Nano17.
URL http://www.ati-ia.com/products/ft/ft_models.aspx?id=Nano17

Balasubramanian, R., Santos, V., 2014. The Human Hand As an Inspiration for Robot Hand Development. Springer Publishing Company, Incorporated.

Barrett, K., Boitano, S., Barman, S., Brooks, L., 2010. Ganongs Review of Medical Physiology 23rd edition. RCN Publishing Ltd.

Beckow, J., 2005. The truth about capillary refill. JEMS: a journal of emergency medical services 30 (1), 14–discussion.

Beebe, D., Hsieh, A., Denton, D., Radwin, R., 1995. A silicon force sensor for robotics and medicine. Sensors and Actuators A: Physical 50 (1), 55–65.
URL http://www.sciencedirect.com/science/article/pii/0924424796800859

Bekesy, G. v., 1967. Sensory Inhibition. Princeton University Press.
URL http://www.jstor.org/stable/j.ctt1m3nzmp

Bhattacharjee, T., Rehg, J., Kemp, C., Oct 2012. Haptic classification and recognition of objects using a tactile sensing forearm. In: 2012 IEEE/RSJ International Conference on Intelligent Robots and Systems. pp. 4090–4097.

Bhattacharjee, T., Wade, J., Chitalia, Y., Kemp, C., 2016. Data-driven thermal recognition of contact with people and objects. In: 2016 IEEE Haptics Symposium, HAPTICS 2016, Philadelphia, PA, USA, April 8-11, 2016. pp. 297–304.
URL http://dx.doi.org/10.1109/HAPTICS.2016.7463193

Bhattacharjee, T., Wade, J., Kemp, C., 2015. Material recognition from heat transfer given varying initial conditions and short-duration contact. In: Robotics: Science and Systems XI, Sapienza University of Rome, Rome, Italy, July 13-17, 2015.
URL http://www.roboticsproceedings.org/rss11/p19.html

Blej, M., Azizi, M., 2016. Comparison of mamdani-type and sugeno-type fuzzy inference systems for fuzzy real time scheduling. International Journal of Applied Engineering Research 11 (22), 11071–11075.

Boothby, A., Das, V., Lopez, J., Tsay, J., Nguyen, T., Banister, R., Lie, D., July 2013. Accurate and continuous non-contact vital signs monitoring using phased array antennas in a clutter-free anechoic chamber. In: 2013 35th Annual International Conference of the IEEE Engineering in Medicine and Biology Society (EMBC). pp. 2862–2865.

BRL, 2016. The tactip website.
URL http://www.brl.ac.uk/research/researchthemes/tactilerobotics/3d-printedtactilesensing.aspx

Chang, C., Lee, F., Lin, Y., Yang, Y., Jan 2016. Tunneling piezoresistive tactile sensing array for continuous blood pressure monitoring. In: 2016 IEEE 29th International Conference on Micro Electro Mechanical Systems (MEMS). pp. 169–172.

Chang, C., Murphy, R., April 2007. Towards robot-assisted mass-casualty triage. In: 2007 IEEE International Conference on Networking, Sensing and Control. pp. 267–272.

Chathuranga, D., Ho, V., Hirai, S., 2013. Investigation of a biomimetic fingertip's ability to discriminate fabrics based on surface textures. In: Advanced Intelligent Mechatronics (AIM), 2013 IEEE/ASME International Conference on. pp. 1667–1674.

Choi, B., Lee, S., Choi, H., Kang, S., Oct 2006. Development of anthropomorphic robot hand with tactile sensor : Skku hand ii. In: 2006 IEEE/RSJ International Conference on Intelligent Robots and Systems. pp. 3779–3784.

Choi, J., Kim, D., June 2009. A remote compact sensor for the real-time monitoring of human heartbeat and respiration rate. IEEE Transactions on Biomedical Circuits and Systems 3 (3), 181–188.

Chorley, C., Melhuish, C., Pipe, T., Rossiter, J., June 2009. Development of a tactile sensor based on biologically inspired edge encoding. In: 2009 International Conference on Advanced Robotics. pp. 1–6.

Chuang, C., Wang, M., Yu, Y., Mu, C., Lu, K., Lin, C., May 2013. Flexible tactile sensor for the grasping control of robot fingers. In: 2013 International Conference on Advanced Robotics and Intelligent Systems. pp. 141–146.

Ciobanu, V., Petrescu, A., Hendrich, N., Zhang, J., Oct 2013. Tactile sensor value preprocessing pipeline. In: System Theory, Control and Computing (ICSTCC), 2013 17th International Conference. pp. 674–680.

Ciobanu, V., Popescu, D., Petrescu, A., July 2014. Point of contact location and normal force estimation using biomimetical tactile sensors. In: Complex, Intelligent and Software Intensive Systems (CISIS), 2014 Eighth International Conference on. pp. 373–378.

Cios, K., 2001. Fuzzy classifier design. Neurocomputing 36 (243), 1–4.
URL http://dblp.uni-trier.de/db/journals/ijon/ijon36.html#Cios01

Clark, F., Horch, W., 1986. Kinethesia. John Wiley and Sons.

Cortes, C., Vapnik, V., 1995. Support-vector networks. Machine Learning 20 (3), 273–297.
URL http://dx.doi.org/10.1007/BF00994018

Cybenko, G., 1989. Approximation by superpositions of a sigmoidal function. Mathematics of Control, Signals and Systems 2 (4), 303–314.
URL http://dx.doi.org/10.1007/BF02551274

Dahiya, R., Metta, G., Valle, M., Sandini, G., Feb 2010. Tactile sensing - from humans to humanoids. Robotics, IEEE Transactions on 26 (1), 1–20.

Dahiya, R., Valle, M., 2008. Tactile Sensing for Robotic Applications.
URL http://www.intechopen.com/books/sensors-focus-on-tactile-force-and-stress-sensors/tactile_sensing_for_robotic_applications

Dahiya, R., Valle, M., 2013. Tactile Sensing Technologies. Springer Netherlands, Dordrecht, pp. 79–136.
URL http://dx.doi.org/10.1007/978-94-007-0579-1_5

Dahiyal, R., Valle, M., Metta, G., Lorenzelli, L., Collini, C., July 2007. Tactile sensing arrays for humanoid robots. In: 2007 Ph.D Research in Microelectronics and Electronics Conference. pp. 201–204.

Dargahi, J., Parameswaran, M., Payandeh, S., Sept 2000. A micromachined piezoelectric tactile sensor for an endoscopic grasper-theory, fabrication and experiments. Journal of Microelectromechanical Systems 9 (3), 329–335.

Dario, P., De Rossi, D., Aug 1985. Tactile sensors and the gripping challenge: Increasing the performance of sensors over a wide range of force is a first step toward robotry that can hold and manipulate objects as humans do. IEEE Spectrum 22 (8), 46–53.

Decherchi, S., Gastaldo, P., Dahiya, R., Valle, M., Zunino, R., June 2011. Tactile-data classification of contact materials using computational intelligence. Robotics, IEEE Transactions on 27 (3), 635–639.

Dempster, A., Laird, N., Rubin, D., 1977. Maximum likelihood from incomplete data via the em algorithm. JOURNAL OF THE ROYAL STATISTICAL SOCIETY, SERIES B 39 (1), 1–38.

Dennis, B., Muthukrishnan, S., 2014. Agfs: Adaptive genetic fuzzy system for medical data classification. Applied Soft Computing 25, 242–252.
URL http://www.sciencedirect.com/science/article/pii/S1568494614004852

Drimus, A., Kootstra, G., Bilberg, A., Kragic, D., 2011. Classification of rigid and deformable objects using a novel tactile sensor. In: Advanced Robotics (ICAR), 2011 15th International Conference on. pp. 427–434.

Drimus, A., Petersen, M., Bilberg, A., Sept 2012. Object texture recognition by dynamic tactile sensing using active exploration. In: RO-MAN, 2012 IEEE. pp. 277–283.

Duan, K.-B., Keerthi, S., 2005. Which Is the Best Multiclass SVM Method? An Empirical Study. Springer Berlin Heidelberg, Berlin, Heidelberg, pp. 278–285.
URL http://dx.doi.org/10.1007/11494683_28

Eeonyx, 2017. Eeonyx piezoresistive fabric sensors.
URL http://eeonyx.com/product_category/pressure-sensors/

Elliott, S., 2001. In: ELLIOTT, S. (Ed.), Signal Processing for Active Control. Academic Press, London.
URL http://www.sciencedirect.com/science/article/pii/B9780122370854500016

Engelbrecht, A., 2007. Computational Intelligence: An Introduction, 2nd Edition. Wiley Publishing.

Ferrigno, G., Baroni, G., Casolo, F., Momi, E., Gini, G., Matteucci, M., Pedrocchi, A., May 2011. Medical robotics. IEEE Pulse 2 (3), 55–61.

FFmpeg Developers, 2016. ffmpeg tool (version be1d324).
URL http://ffmpeg.org/

Fishel, A., 2012. Design and use of a biomimetic tactile microvibration sensor with human-like sensitivity and its application in texture discrimination using bayesian exploration. Ph.D. thesis, Dissertations & Theses Gradworks, University of Southern California.

Fishel, J., Loeb, G., 2012a. Bayesian exploration for intelligent identification of textures. Frontiers in Neurorobotics 6 (4).
URL http://journal.frontiersin.org/article/10.3389/fnbot.2012.00004

Fishel, J., Loeb, G., June 2012b. Sensing tactile microvibrations with the biotac comparison with human sensitivity. In: 2012 4th IEEE RAS EMBS International Conference on Biomedical Robotics and Biomechatronics (BioRob). pp. 1122–1127.

Fishel, J., Santos, V., Loeb, G., 2008. A robust micro-vibration sensor for biomimetic fingertips. In: 2008 2nd IEEE RAS & EMBS International Conference on Biomedical Robotics and Biomechatronics. IEEE, pp. 659–663.

Flanagan, J., Wing, A., 1993. Modulation of grip force with load force during point-to-point arm movements. Experimental Brain Research 95 (1), 131–143.
URL http://dx.doi.org/10.1007/BF00229662

Fraden, J., 2003. Handbook of Modern Sensors: Physics, Designs, and Applications (Handbook of Modern Sensors). SpringerVerlag.

Friesen, R., Wiertlewski, M., Peshkin, M. A., Colgate, J., June 2015. Bioinspired artificial fingertips that exhibit friction reduction when subjected to transverse ultrasonic vibrations. In: World Haptics Conference (WHC), 2015 IEEE. pp. 208–213.

Fukunaga, K., 1990. Introduction to Statistical Pattern Recognition (2Nd Ed.). Academic Press Professional, Inc., San Diego, CA, USA.

Gagarin, R., Celik, N., Huang, G., Iskander, M., July 2012. Microwave stethoscope, a new noninvasive multiple vital signs sensor: Human clinical trials. In: Proceedings of the 2012 IEEE International Symposium on Antennas and Propagation. pp. 1–2.

Gagarin, R., Huang, G., Rabbi, A., Iskander, M., July 2014. Textile sensor for monitoring vital signs. In: 2014 IEEE Antennas and Propagation Society International Symposium (APSURSI). pp. 965–966.

Gault, T., Farag, A., June 2013. A fully automatic method to extract the heart rate from thermal video. In: 2013 IEEE Conference on Computer Vision and Pattern Recognition Workshops. pp. 336–341.

Gibson, E. J., 1988. Exploratory behavior in the development of perceiving, acting, and the acquiring of knowledge. In: Annual Review of Psychology. Vol. 39. pp. 1–41.

Goger, D., Gorges, N., Worn, H., May 2009. Tactile sensing for an anthropomorphic robotic hand: Hardware and signal processing. In: 2009 IEEE International Conference on Robotics and Automation. pp. 895–901.

Gray, B., Fearing, R., Apr 1996. A surface micromachined microtactile sensor array. In: Proceedings of IEEE International Conference on Robotics and Automation. Vol. 1. pp. 1–6.

Gu, C., Li, C., June 2014. From tumor targeting to speech monitoring: Accurate respiratory monitoring using medical continuous-wave radar sensors. IEEE Microwave Magazine 15 (4), 66–76.

Hall, M., Frank, E., Holmes, G., Pfahringer, B., Reutemann, P., Witten, I., 2009. The WEKA data mining software: an update. SIGKDD Explorations 11 (1), 10–18.

Hameed, I., Jun. 2011. Using gaussian membership functions for improving the reliability and robustness of students' evaluation systems. Expert Systems with Applications 38 (6), 7135–7142.
URL http://dx.doi.org/10.1016/j.eswa.2010.12.048

Hameed, I., Sorensen, C., 2010.
URL http://www.intechopen.com/books/export/citation/BibTex/fuzzy-systems/fuzzy-systems-in-education-a-more-reliable-system-for-student-eva

Hasegawa, H., Mizoguchi, Y., Tadakuma, K., Ming, A., Ishikawa, M., Shimojo, M., May 2010. Development of intelligent robot hand using proximity, contact and slip sensing. In: 2010 IEEE International Conference on Robotics and Automation. pp. 777–784.

Haven, E., Liu, X., Shen, L., 2012. De-noising option prices with the wavelet method. European Journal of Operational Research 222 (1), 104–112.
URL http://www.sciencedirect.com/science/article/pii/S037722171200313X

He, D., Winokur, E., Sodini, C., Nov 2015. An ear-worn vital signs monitor. IEEE Transactions on Biomedical Engineering 62 (11), 2547–2552.

Heo, J., Chung, J., Lee, J., 2006. Tactile sensor arrays using fiber bragg grating sensors. Sensors and Actuators A: Physical 126 (2), 312–327.
URL http://www.sciencedirect.com/science/article/pii/S0924424705006084

Ho, V., Araki, T., Makikawa, M., Hirai, S., 2012. Experimental investigation of surface identification ability of a low-profile fabric tactile sensor. In: Intelligent Robots and Systems (IROS), 2012 IEEE/RSJ International Conference on. pp. 4497–4504.

Ho, V., Kondo, D., Okada, S., Araki, T., Fujita, E., Makikawa, M., Hirai, S., 2011. Development of a low-profile sensor using electro-conductive yarns in recognition of slippage. In: Intelligent Robots and Systems (IROS), 2011 IEEE/RSJ International Conference on. pp. 1946–1953.

Hoelscher, J., Peters, J., Hermans, T., 2015. Evaluation of tactile feature extraction for interactive object recognition. In: Proceedings of 15th IEEE-RAS International Conference on Humanoid Robots. IEEE, Seoul, pp. 310–317.

Howe, R., 1994. Tactile sensing and control of robotic manipulation. Journal of Advanced robotics 8 (3), 245–261.

Hu, J., Edsinger, A., Lim, Y.-J., Donaldson, N., Solano, M., Solochek, A., Marchessault, R., May 2011. An advanced medical robotic system augmenting healthcare capabilities - robotic nursing assistant. In: 2011 IEEE International Conference on Robotics and Automation. pp. 6264–6269.

Hui, J., Block, A., Taylor, C., Kuchenbecker, K., April 2016. Robust tactile perception of artificial tumors using pairwise comparisons of sensor array readings. In: 2016 IEEE Haptics Symposium (HAPTICS). pp. 305–312.

Inaba Rubber, 2017. Conductive rubber.
URL http://www.inaba-rubber.co.jp/en/b_products/inastomer/index.html

Islam, M., Wu, Q. M. J., Ahmadi, M., Sid-Ahmed, M., 2007. Investigating the performance of naive- bayes classifiers and k- nearest neighbor classifiers. In: Convergence Information Technology, 2007. International Conference on. pp. 1541–1546.

Iyer, B., Kumar, A., Pathak, N. P., Ghosh, D., Dec 2013. Concurrent multi-band rf system for search and rescue of human life during natural calamities. In: IEEE MTT-S International Microwave and RF Conference. pp. 1–4.

Jacobson, A. L., Oct 2001. Auto-threshold peak detection in physiological signals. In: Engineering in Medicine and Biology Society, 2001. Proceedings of the 23rd Annual International Conference of the IEEE. Vol. 3. pp. 2194–2195.

Jain, A., Mao, J., Mohiuddin, K., Mar. 1996. Artificial neural networks: A tutorial. Computer 29 (3), 31–44.
URL http://dx.doi.org/10.1109/2.485891

Jamali, N., Sammut, C., may 2010. Material classification by tactile sensing using surface textures. In: Robotics and Automation (ICRA), 2010 IEEE International Conference on. pp. 2336–2341.

Jamali, N., Sammut, C., 2011. Majority voting: Material classification by tactile sensing using surface texture. Robotics, IEEE Transactions on 27 (3), 508–521.

Jamone, L., Metta, G., Nori, F., Sandini, G., Dec 2006. James: A humanoid robot acting over an unstructured world. In: 2006 6th IEEE-RAS International Conference on Humanoid Robots. pp. 143–150.

Jianfeng, W., Lianjie, Z., Jianqing, L., Zhipeng, M., CongYan, C., 2011. Experiment on roughness identification using thermal tactile sensor. In: Electric Information and Control Engineering (ICEICE), 2011 International Conference on. pp. 378–381.

Johansson, R., Flanagan, J., 2009. Coding and use of tactile signals from the fingertips in object manipulation tasks. Nat. Rev Neuroscience 10 (5), 345–359.
URL http://dx.doi.org/10.1038/nrn2621

Johansson, R., Vallbo, A., 1979. Tactile sensibility in the human hand: relative and absolute densities of four types of mechanoreceptive units in glabrous skin. The Journal of Physiology 286 (1), 283–300.

Johansson, R. S., Westling, G., 1984. Roles of glabrous skin receptors and sensorimotor memory in automatic control of precision grip when lifting rougher or more slippery objects. Experimental Brain Research 56, 550–564.

Johnson, M., Cole, F., Raj, A., Adelson, E., 2011. Microgeometry capture using an elastomeric sensor. ACM Transactions on Graphics (Proc. ACM SIGGRAPH) 30 (4), 46:1–46:8.

Johnsson, M., Balkenius, C., Sept 2008. Recognizing texture and hardness by touch. In: Intelligent Robots and Systems, 2008. IROS 2008. IEEE/RSJ International Conference on. pp. 482–487.

Johnsson, M., Balkenius, C., June 2011. Sense of touch in robots with self-organizing maps. Robotics, IEEE Transactions on 27 (3), 498–507.

Jurie, F., Triggs, B., Oct 2005. Creating efficient codebooks for visual recognition. In: Computer Vision, 2005. ICCV 2005. Tenth IEEE International Conference on. Vol. 1. pp. 604–610.

Kaboli, M., Cheng, G., Sep 2015. Dexterous hands learn to re-use the past experience to discriminate in-hand objects from the surface texture. In: 33rd Annual Conference of the Robotics Society of Japan (RSJ 2015). Robotics Society of Japan, Tokyo.

Kaboli, M., De La Rosa, A., Walker, R., Cheng, G., Nov 2015. In-hand object recognition via texture properties with robotic hands, artificial skin, and novel tactile descriptors. In: Humanoid Robots (Humanoids), 2015 IEEE-RAS 15th International Conference on. pp. 1155–1160.

Kaiser, G., 1994. A Friendly Guide to Wavelets. Birkhauser Boston Inc., Cambridge, MA, USA.

Kampmann, P., Kirchner, F., 2014. Integration of fiber-optic sensor arrays into a multi-modal tactile sensor processing system for robotic end-effectors. Sensors 14 (4), 6854–6876.
URL http://www.mdpi.com/1424-8220/14/4/6854

Kappassov, Z., Corrales, J.-A., Perdereau, V., 2015. Tactile sensing in dexterous robot hands - review. Robotics and Autonomous Systems 74, Part A, 195–220.
URL http://www.sciencedirect.com/science/article/pii/S0921889015001621

Karlen, W., Pickard, A., Daniels, J., Kwizera, A., Ibingira, C., Dumont, G., Ansermino, J., Oct 2011. Automated validation of capillary refill time measurements using photo-plethysmogram from a portable device for effective triage in children. In: 2011 IEEE Global Humanitarian Technology Conference. pp. 66–71.

Kawamura, T., Inaguma, N., Nejigane, K., Tani, K., Yamada, H., 2013. Measurement of slip, force and deformation using hybrid tactile sensor system for robot hand gripping an object. International Journal of Advanced Robotic Systems 10 (1), 83.
URL http://dx.doi.org/10.5772/55476

Kerr, E., McGinnity, T., Coleman, S., Dec 2013. Material classification based on thermal properties - a robot and human evaluation. In: 2013 IEEE International Conference on Robotics and Biomimetics, December 12-14 2013, Shenzhen, China. pp. 1048–1053.

Kerr, E., McGinnity, T., Coleman, S., Dec 2014a. Material classification based on thermal and surface texture properties evaluated against human performance. In: 2014 IEEE International Conference on Control, Automation, Robotics and Vision, ICARCV 2014, Singapore, Dec 2014.

Kerr, E., McGinnity, T., Coleman, S., Aug 2014b. Tactile approach to material classification - evaluated with human performance. In: Irish Machine Vision and Image Processing 2014, Northern Ireland. pp. 175–180.

Kerr, E., McGinnity, T., Coleman, S., 2017. Tactile sensing based material classification. Elsevier Journal of Expert Systems with Applications.

Kerr, E., McGinnity, T., Coleman, S., Shepherd, A., July 2015. Towards pulse detection and rhythm analysis using a biomimetic fingertip. In: 2015 IEEE International Joint Conference on Neural Networks, July 12-17 2015, Killarney, Ireland.

King, D., Morton, R., Bevan, C., 2014. How to use capillary refill time. Archives of Disease in Childhood - Education and Practice 99 (3), 111–116.
URL http://ep.bmj.com/content/99/3/111

Klawonn, F., Angelov, P., 2006. Evolving extended naive bayes classifiers. In: Data Mining Workshops, 2006. ICDM Workshops 2006. Sixth IEEE International Conference on. pp. 643–647.

Kral, A., Majernik, V., 1996. On lateral inhibition in the auditory system. Gen. Physiol. Biophys. 15, 109–127.

Kroemer, O., Lampert, C., Peters, J., 2011. Learning dynamic tactile sensing with robust vision-based training. IEEE Transaction on Robotics (27(3)), 1552–3098, intelligent Autonomous Systems.
URL http://tubiblio.ulb.tu-darmstadt.de/55385/

Kuncheva, L., 2012. Fuzzy Classifier Design. Studies in Fuzziness and Soft Computing. Physica-Verlag HD.
URL https://books.google.co.uk/books?id=ScuqCAAAQBAJ

Kuo, H., Lin, C., Yu, C., Lo, P., Lyu, J., Chou, C., Chuang, H., April 2016. A fully integrated 60-ghz cmos direct-conversion doppler radar rf sensor with clutter canceller for single-antenna noncontact human vital-signs detection. IEEE Transactions on Microwave Theory and Techniques 64 (4), 1018–1028.

Kuo, H. C., Chou, C. C., Lin, C. C., Yu, C. H., Huang, T. H., Chuang, H. R., May 2015. A 60-ghz cmos direct-conversion doppler radar rf sensor with clutter canceller for single-antenna noncontact human vital-signs detection. In: 2015 IEEE Radio Frequency Integrated Circuits Symposium (RFIC). pp. 35–38.

Lederman, S., Klatzky, R., jul 1987. Hand movements: A window into haptic object recognition. Cognitive Psychology 19 (3), 342–368.

Lee, J.-H., Kim, Y., Ku, J., Park, H.-J., 2013. Optical-based artificial palpation sensors for lesion characterization. Sensors 13 (8), 11097–11113.
URL http://www.mdpi.com/1424-8220/13/8/11097

Lee, M., Nicholls, H., 1999a. Review article tactile sensing for mechatronics-a state of the art survey. Mechatronics 9 (1), 1–31.
URL http://www.sciencedirect.com/science/article/pii/S0957415898000452

Lee, M. H., Nicholls, H. R., Feb 1999b. Review article tactile sensing for mechatronics-a state of the art survey. Mechatronics 9 (1), 1–31.

Li, G.-H., Qin, C.-D., Wang, Z.-S., 1992. Neurite branching pattern formation: Modeling and computer simulation. Journal of Theoretical Biology 157 (4), 463–486.
URL http://www.sciencedirect.com/science/article/pii/S0022519305806642

Li, R., Adelson, E., June 2013. Sensing and recognizing surface textures using a gelsight sensor. In: 2013 IEEE Conference on Computer Vision and Pattern Recognition. pp. 1241–1247.

Lin, C.-H., Erickson, T., Fishel, J., Wettels, N., Loeb, G., 2009. Signal processing and fabrication of a biomimetic tactile sensor array with thermal, force and microvibration modalities. In: ROBIO. IEEE, pp. 129–134.
URL http://dblp.uni-trier.de/db/conf/robio/robio2009.html#LinEFWL09

Lin, J., Oct 1975. Noninvasive microwave measurement of respiration. Proceedings of the IEEE 63 (10), 1530–1530.

Liu, J., Hou, Y., Zhang, H., Jia, P., Su, S., Fang, G., Liu, W., Xiong, J., 2017. A wide-range displacement sensor based on plastic fiber macro-bend coupling. Sensors 17 (1).

Loeb, G., Fishel, J., 2009. The role of fingerprints in vibrotactile discrimination. Whitepaper for DoD Physics of Biology, University of Southern California.

Loeb, G. E., Tsianos, G., Fishel, J., Wettels, N., Schaal, S., 2011. Understanding haptics by evolving mechatronic systems. Progress in Brain Research 192, 129–144.

Loomis, J., Lederman, S., 1986. Tactual perception. John Wiley and Sons, New York, Ch. 31, pp. 1–41.

Lowe, D., 1999. Object recognition from local scale-invariant features. In: Computer Vision, 1999. The Proceedings of the Seventh IEEE International Conference on. Vol. 2. pp. 1150–1157.

Lu, G., Yang, F., Jing, X., Yu, X., Zhang, H., Xue, H., Wang, J., May 2011. Contact-free monitoring of human vital signs via a microwave sensor. In: 2011 5th International Conference on Bioinformatics and Biomedical Engineering. pp. 1–3.

Lucarotti, C., Oddo, C., Vitiello, N., Carrozza, M., 2013. Synthetic and bio-artificial tactile sensing: A review. Sensors 13 (2), 1435–1466.
URL http://www.mdpi.com/1424-8220/13/2/1435

Luo, J. W., Bai, J., Shao, J. H., September 2006. Application of the wavelet transforms on axial strain calculation in ultrasound elastography. Progress in Natural Science 16 (9), 942–947.

Luo, S., Liu, X., Althoefer, K., Liu, H., 2015. Tactile object recognition with semi-supervised learning. In: Liu, H., Kubota, N., Zhu, X., Dillmann, R., Zhou, D. (Eds.), Intelligent Robotics and Applications. Vol. 9245 of Lecture Notes in Computer Science. Springer International Publishing, pp. 15–26.

Maheshwari, V., Saraf, R., 2006. High-resolution thin-film device to sense texture by touch. Science 312 (5779), 1501–1504.

Mahfouz, M., To, G., Kuhn, M., Dec 2011. No strings attached. IEEE Microwave Magazine 12 (7), S34–S48.

Mallat, S., 2008. A Wavelet Tour of Signal Processing, Third Edition: The Sparse Way, 3rd Edition. Academic Press.

Mallat, S. G., Jul. 1989. A theory for multiresolution signal decomposition: The wavelet representation. IEEE Trans. Pattern Anal. Mach. Intell. 11 (7), 674–693.
URL http://dx.doi.org/10.1109/34.192463

Mamdani, E., December 1974. Application of fuzzy algorithms for control of simple dynamic plant. Electrical Engineers, Proceedings of the Institution of 121 (12), 1585–1588.

Mamdani, E., dec 1977. Application of fuzzy logic to approximate reasoning using linguistic synthesis. IEEE Transactions on Computers 26 (12), 1182–1191.
URL http://dx.doi.org/10.1109/TC.1977.1674779

Marks, L. E., 1988. Similarities and differences among the senses. In: The International Journal of Neuroscience. Vol. 19. pp. 1–11.

Martinez, A., Kak, A., Feb 2001. Pca versus lda. Pattern Analysis and Machine Intelligence, IEEE Transactions on 23 (2), 228–233.

MATLAB, R2013. version 8.10.0 (R2013a). The MathWorks Inc., Natick, Massachusetts.

MATLAB Fuzzy Logic Toolbox, 2013. MATLAB Fuzzy Logic Toolbox version 8.10.0 (R2013a). The MathWorks Inc., Natick, Massachusetts.

Mellado, I., 2013. Uavster website.
URL http://www.ignaciomellado.es/blog/Measuring-heart-rate-with-a-smartphone-camera

Mi, X., Nakazawa, F., Nov 2014. A multipoint thin film polymer pressure/force sensor to visualize traditional medicine palpations. In: IEEE SENSORS 2014 Proceedings. pp. 843–846.

Mika, S., Rätsch, G., Weston, S., Schölkopf, B., Müller, K.-R., 1999. Fisher discriminant analysis with kernels.

Milighetti, G., Emter, T., Kuntze, H., Bechler, D., Kroschel, K., Sept 2006. Combined visual-acoustic grasping for humanoid robots. In: 2006 IEEE International Conference on Multisensor Fusion and Integration for Intelligent Systems. pp. 1–6.

Misiti, M., Misiti, Y., Oppenheim, G., Poggi, J.-M., 2007. Wavelets and their Applications. Wiley Publishing.

Monkman, G. J., Taylor, P., 1993. Thermal tactile sensing. Robotics and Automation, IEEE Transactions on 9 (3), 313–318.

Moreira, C., 2011. Learning to rank academic experts. Ph.D. thesis, Master Thesis, Technical University of Lisbon.

Möser, M., 2009. Structure-borne sound. Springer Berlin Heidelberg, Berlin, Heidelberg, pp. 117–142.
URL http://dx.doi.org/10.1007/978-3-540-92723-5_4

Mount, D., Ayra, S., 2010. Ann: Alibrary for approximate nearest neighbour searching.
URL https://www.cs.umd.edu/~mount/ANN/

Mouradian, V., Poghosyan, A., Hovhannisyan, L., Oct 2014. Continuous wearable health monitoring using novel ppg optical sensor and device. In: 2014 IEEE 10th International Conference on Wireless and Mobile Computing, Networking and Communications (WiMob). pp. 120–123.

Müller, K.-R., Mika, S., Rätsch, G., Tsuda, K., Schölkopf, B., 2001. An introduction to kernel-based learning algorithms. IEEE TRANSACTIONS ON NEURAL NETWORKS 12 (2), 181–201.

Murphy, R., Srinivasan, V., Henkel, Z., Suarez, J., Minson, M., Straus, J., Hempstead, S., Valdez, T., Egawa, S., Nov 2013. Interacting with trapped victims using robots. In: 2013 IEEE International Conference on Technologies for Homeland Security (HST). pp. 32–37.

Naaz, S., Alam, A., Biswas, R., 2011. Effect of different defuzzification methods in a fuzzy based load balancing application. IJCSI-International Journal of Computer Science Issues 8 (5).

National Instruments, 2017. Labview software.
URL http://www.ni.com/labview/

Nguyen, T., Khosravi, A., Creighton, D., Nahavandi, S., 2015. Medical data classification using interval type-2 fuzzy logic system and wavelets. Applied Soft Computing 30, 812–822.
URL http://www.sciencedirect.com/science/article/pii/S1568494615001076

Nowlin, W., Apr 1991. Experimental results on bayesian algorithms for interpreting compliant tactile sensing data. In: Proceedings. 1991 IEEE International Conference on Robotics and Automation. Vol. 112. pp. 378–383.

Ojala, T., Pietikäinen, M., Mäenpää, T., jul 2002. Multiresolution gray-scale and rotation invariant texture classification with local binary patterns. IEEE Trans. Pattern Anal. Mach. Intell. 24 (7), 971–987.
URL http://dx.doi.org/10.1109/TPAMI.2002.1017623

Omata, S., Murayama, Y., Constantinou, C., 2004. Real time robotic tactile sensor system for the determination of the physical properties of biomaterials. Sensors and actuators. A, Physical 112 (2–3), 278–285, eng.
URL http://www.refdoc.fr/Detailnotice?idarticle=8120165

Otieno, H., Were, E., Ahmed, I., Charo, E., Brent, A., Maitland, K., 2004. Are bedside features of shock reproducible between different observers? Archives of Disease in Childhood 89 (10), 977–979.
URL http://adc.bmj.com/content/89/10/977

Pacchierotti, C., Prattichizzo, D., Kuchenbecker, K., 2014. A Data-Driven Approach to Remote Tactile Interaction: From a BioTac Sensor to any Fingertip Cutaneous Device. Springer Berlin Heidelberg, Berlin, Heidelberg, pp. 418–424.
URL http://dx.doi.org/10.1007/978-3-662-44193-0_52

Pacchierotti, C., Prattichizzo, D., Kuchenbecker, K., Oct 2015. Displaying sensed tactile cues with a fingertip haptic device. IEEE Transactions on Haptics 8 (4), 384–396.

Pal, S., Mandal, D., 1991. Fuzzy logic and approximate reasoning: An overview. IETE Journal of Research 37 (5-6), 548–560.
URL http://dx.doi.org/10.1080/03772063.1991.11437008

Pezzementi, Z., Plaku, E., Reyda, C., Hager, G., june 2011. Tactile-object recognition from appearance information. Robotics, IEEE Transactions on 27 (3), 473–487.

Prescott, T., Ahissar, E., Izhikevich, E., 2015. Scholarpedia of Touch. Scholarpedia. Atlantis Press.
URL https://books.google.co.uk/books?id=SHf_CgAAQBAJ

Press, W., Teukolsky, S., Vetterling, W., Flannery, B., 2007. Numerical Recipes 3rd Edition: The Art of Scientific Computing, 3rd Edition. Cambridge University Press, New York, NY, USA.

Qian, Y., Song, A., Yan, R., May 2011. Design and realization of an array pulse detecting tactile sensor. In: 2011 IEEE International Instrumentation and Measurement Technology Conference. pp. 1–5.

R Core Team, 2013. R: A Language and Environment for Statistical Computing. R Foundation for Statistical Computing, Vienna, Austria.
URL http://www.R-project.org/

Ramos-Garcia, R., Da Silva, F., Kondi, Y., Sazonov, E., Dunne, L., Nov 2016. Analysis of a coverstitched stretch sensor for monitoring of breathing. In: 2016 10th International Conference on Sensing Technology (ICST). pp. 1–6.

Reichardt, W., MacGinitie, G., 1962. Zur theorie der lateralen inhibition. Kybernetik 1, 155–165.

Ren, L., Wang, H., Naishadham, K., Liu, Q., Fathy, A., May 2015. Non-invasive detection of cardiac and respiratory rates from stepped frequency continuous wave radar measurements using the state space method. In: 2015 IEEE MTT-S International Microwave Symposium. pp. 1–4.

Rish, I., 2001. An empirical study of the naive bayes classifier. Tech. rep.

Roke, C., Melhuish, C., Pipe, T., Drury, D., Chorley, C., 2012. Lump localisation through a deformation-based tactile feedback system using a biologically inspired finger sensor. Robotics and Autonomous Systems 60 (11), 1442–1448, towards Autonomous Robotic Systems 2011.
URL http://www.sciencedirect.com/science/article/pii/S0921889012000589

Roke, C., Spiers, A., Pipe, T., Melhuish, C., April 2013. The effects of laterotactile information on lump localization through a teletaction system. In: 2013 World Haptics Conference (WHC). pp. 365–370.

Romano, J., Hsiao, K., Niemeyer, G., Chitta, S., Kuchenbecker, K., Dec 2011. Human-inspired robotic grasp control with tactile sensing. IEEE Transactions on Robotics 27 (6), 1067–1079.

Rosenblatt, F., 1962. Principles of neurodynamics: perceptrons and the theory of brain mechanisms. Report (Cornell Aeronautical Laboratory). Spartan Books.
URL https://books.google.co.uk/books?id=7FhRAAAAMAAJ

Rothwell, J., Traub, M., Day, B., Obeso, J., Thomas, P., Marsden, C., 1982. Manual motor performance in a deafferented man. Brain 105, 515–542.

Royal College of Physicians of London, 2012. National Early Warning Score (NEWS): Standardising the Assessment of Acute-Illness Severity in the NHS. Royal College of Physicians of London.
URL https://books.google.co.uk/books?id=5sVdMwEACAAJ

Rumelhart, D., Hinton, G., Williams, R., 1986. Parallel distributed processing: Explorations in the microstructure of cognition, vol. 1. MIT Press, Cambridge, MA, USA, Ch. Learning Internal Representations by Error Propagation, pp. 318–362.
URL http://dl.acm.org/citation.cfm?id=104279.104293

Saeki, Y., Takamura, K., Magatani, K., Aug 2006. The measurement technique of human's bio-signals. In: 2006 International Conference of the IEEE Engineering in Medicine and Biology Society. pp. 1351–1354.

Sakoe, H., Chiba, S., 1978. Dynamic programming algorithm optimization for spoken word recognition. Acoustics, Speech and Signal Processing, IEEE Transactions on 26 (1), 43–49.

Samani, H., Zhu, R., 2016. Robotic automated external defibrillator ambulance for emergency medical service in smart cities. IEEE Access 4, 268–283.

Sato, K., Kamiyama, K., Nii, H., Kawakami, N., Tachi, S., Sept 2008. Measurement of force vector field of robotic finger using vision-based haptic sensor. In: Intelligent Robots and Systems, 2008. IROS 2008. IEEE/RSJ International Conference on. pp. 488–493.

Schalkoff, R., 1997. Artificial Neural Networks, 1st Edition. McGraw-Hill Higher Education.

Scheibert, J., Leurent, S., Prevost, A., Debrégeas, G., 2009. The role of fingerprints in the coding of tactile information probed with a biomimetic sensor. Science 323 (5920), 1503–1506.
URL http://science.sciencemag.org/content/323/5920/1503

Schmidt, P., Maël, E., Würtz, R., Dec 2006. A sensor for dynamic tactile information with applications in human-robot interaction and object exploration. Robot. Auton. Syst. 54 (12), 1005–1014.
URL http://dx.doi.org/10.1016/j.robot.2006.05.013

Schmitz, A., Maiolino, P., Maggiali, M., Natale, L., Cannata, G., Metta, G., June 2011. Methods and technologies for the implementation of large-scale robot tactile sensors. IEEE Transactions on Robotics 27 (3), 389–400.

Schneider, A., Sturm, J., Stachniss, C., Reisert, M., Burkhardt, H., Burgard, W., oct 2009. Object identification with tactile sensors using bag-of-features. In: Intelligent Robots and Systems, 2009. IROS 2009. IEEE/RSJ International Conference on. pp. 243–248.

Schulz, S., Pylatiuk, C., Kargov, A., Oberle, R., Bretthauer, G., Nov 2004. Progress in the development of anthropomorphic fluidic hands for a humanoid robot. In: 4th IEEE/RAS International Conference on Humanoid Robots, 2004. Vol. 2. pp. 566–575.

Schunk, 2017. Schunk sdh multi-jointed 3-finger gripper.
URL http://de.schunk.com/fr_en/gripping-systems/series/sdh/

Shadow Robot Company, 2017. Shadow dexterous hand.
URL http://www.shadowrobot.com/products/dexterous-hand/

Shimojo, M., Araki, T., Ming, A., Ishikawa, M., April 2010. A high-speed mesh of tactile sensors fitting arbitrary surfaces. Sensors Journal, IEEE 10 (4), 822–830.

Smitsman, A. W., Schellingerhout, R., 2000. Exploratory behavior in blind infants: How to improve touch? In: Infant Behavior and Development. Vol. 23. pp. 485–511.

SolidWorks, 2016. The Solid Works Website.
URL http://www.solidworks.com

Someya, T., September 2013. Building bionic skin. IEEE Spectrum 50 (9), 50–56.

Someya, T., Tsuyoshi, S., Shingo, I., Yusaku, K., Hiroshi, K., Takayasu, S., 2004. A large-area, flexible pressure sensor matrix with organic field-effect transistors for artificial skin applications. Proceedings of the National Academy of Sciences of the United States of America 101 (27), 9966–9970.
URL http://www.pnas.org/content/101/27/9966.abstract

Šprager, S., Donlagić, D., Zazula, D., Oct 2010. Monitoring of basic human vital functions using optical interferometer. In: IEEE 10th INTERNATIONAL CONFERENCE ON SIGNAL PROCESSING PROCEEDINGS. pp. 1–4.

Šprager, S., Donlagić, D., Zazula, D., Dec 2012. Overnight heartbeat monitoring by using unobtrusive optical interferometric measurements. In: 2012 IEEE-EMBS Conference on Biomedical Engineering and Sciences. pp. 847–852.

Stollnberger, G., Moser, C., Giuliani, M., Stadler, S., Tscheligi, M., Szczesniak-Stanczyk, D., Stanczyk, B., Aug 2016. User requirements for a medical robotic system: Enabling doctors to remotely conduct ultrasonography and physical examination. In: 2016 25th IEEE International Symposium on Robot and Human Interactive Communication (RO-MAN). pp. 1156–1161.

Strozik, K., Pieper, C., Roller, J., 1997. Capillary refilling time in newborn babies: normal values. Archives of Disease in Childhood - Fetal and Neonatal Edition 76 (3), F193–F196.
URL http://fn.bmj.com/content/76/3/F193.abstract

Syntouch, 2013. The syntouch website.
URL http://www.syntouchllc.com/Products/BioTac/

Tasli, H., Gudi, A., den Uyl, M., Oct 2014. Remote ppg based vital sign measurement using adaptive facial regions. In: 2014 IEEE International Conference on Image Processing (ICIP). pp. 1410–1414.

Tekscan, 2017. Flexiforce sensors.
URL https://www.tekscan.com/flexiforce-load-force-sensors-and-syst

Tenzer, Y., Jentoft, L., Howe, R., Sept 2014. The feel of mems barometers: Inexpensive and easily customized tactile array sensors. IEEE Robotics Automation Magazine 21 (3), 89–95.

Tiest, W., 2010. Tactual perception of material properties. Vision Research 50 (24), 2775–2782, perception and Action: Part I.
URL //www.sciencedirect.com/science/article/pii/S0042698910004967

Tiwana, M., Redmond, S., Lovell, N., 2012. A review of tactile sensing technologies with applications in biomedical engineering. Sensors and Actuators A: Physical 179 (4), 17–31.
URL http://www.sciencedirect.com/science/article/pii/S0924424712001641

Total Phase, 2017. Cheetah spi/usb device.
URL http://www.totalphase.com/products/cheetah-spi/

Tran, D., Lee, H., Kim, C., June 2015. A robust real time system for remote heart rate measurement via camera. In: 2015 IEEE International Conference on Multimedia and Expo (ICME). pp. 1–6.

Vallbo, A., Johansson, R., 1978. The tactile sensory innervation of the glabrous skin of the human hand. Oxford: Pergamon Press Ltd., pp. 29–54.

Varma, M., Zisserman, A., Apr 2005. A statistical approach to texture classification from single images. Int. J. Comput. Vision 62 (1-2), 61–81.

Veiga, F., van Hoof, H., Peters, J., Hermans, T., Sept 2015. Stabilizing novel objects by learning to predict tactile slip. In: Intelligent Robots and Systems (IROS), 2015 IEEE/RSJ International Conference on. pp. 5065–5072.

Vidal-Verdú, F., Barquero, M., Castellanos-Ramos, J., Navas-González, R., Sánchez, J., Serón, J., García-Cerezo, A., 2011. A large area tactile sensor patch based on commercial force sensors. Sensors 11 (5), 5489–5507.
URL http://www.mdpi.com/1424-8220/11/5/5489

Wade, J., Bhattacharjee, T., Kemp, C., 2015. A handheld device for the in situ acquisition of multimodal tactile sensing data. CoRR abs/1511.03152.
URL http://arxiv.org/abs/1511.03152

Walker, R., June 2004. Developments in dextrous hands for advanced robotic applications. In: Proceedings World Automation Congress, 2004. Vol. 15. pp. 123–128.

Walraven, G., 2011. Basic Arrhythmias. EKG Series. Pearson.
URL https://books.google.co.uk/books?id=U7eimgEACAAJ

Wasserman, P., 1989. Neural computing: Theory and Practice. A van Nostrand Reinhold book. Van Nostrand Reinhold.
URL https://books.google.co.uk/books?id=DtgmAAAAMAAJ

Weiss, K., Worn, H., 2004. Tactile sensor system for an anthropomorphic robotic hand. In: IEEE International Conference on Manipulation and Grasping. Genoa, Italy.

Weiss Robotics, 2017. Tactile sensors.
URL https://www.weiss-robotics.com/en/start-page/

Wettels, N., Fishel, J., Loeb, G., 2014. Multimodal Tactile Sensor. Springer International Publishing, Cham, pp. 405–429.
URL http://dx.doi.org/10.1007/978-3-319-03017-3_19

Wettels, N., Loeb, G., Dec 2011. Haptic feature extraction from a biomimetic tactile sensor: Force, contact location and curvature. In: Robotics and Biomimetics (ROBIO), 2011 IEEE International Conference on. pp. 2471–2478.

Wettels, N., Parnandi, A., Moon, J., Loeb, G., Sukhatme, G., Dec 2009. Grip control using biomimetic tactile sensing systems. IEEE/ASME Transactions on Mechatronics 14 (6), 718–723.

Wettels, N., Santos, V., Johansson, R., Loeb, G., 2008. Biomimetic tactile sensor array. Advanced Robotics 22 (8), 829–849.
URL http://dblp.uni-trier.de/db/journals/ar/ar22.html#WettelsSJL08

Winstone, B., Griffiths, G., Melhuish, C., Pipe, T., Rossiter, J., Dec 2012. Tactip; tactile fingertip device, challenges in reduction of size to ready for robot hand integration. In: 2012 IEEE International Conference on Robotics and Biomimetics (ROBIO). pp. 160–166.

Wolffenbuttel, M., Regtien, P., 1991. Polysilicon bridges for the realization of tactile sensors. Sensors and Actuators A: Physical 26 (1), 257–264.
URL http://www.sciencedirect.com/science/article/pii/092442479187002K

Wong, K., Lo, S., Lin, C., Lasser, B., Mun, S., Sept 2009. Imaging components for a robotic casualty evaluation system. In: 2009 Annual International Conference of the IEEE Engineering in Medicine and Biology Society. pp. 467–470.

Wu, H.-Y., Rubinstein, M., Shih, E., Guttag, J., Durand, F., Freeman, W., 2012. Eulerian video magnification for revealing subtle changes in the world. ACM Trans. Graph. (Proceedings SIGGRAPH 2012) 31 (4).

Xie, H., Jiang, A., Wurdemann, H., Liu, H., Seneviratne, L., Althoefer, K., 3 2014. Magnetic resonance-compatible tactile force sensor using fiber optics and vision sensor. IEEE SENSORS JOURNAL 14 (3), 829–838.

Xu, D., Loeb, G., Fishel, J., May 2013. Tactile identification of objects using bayesian exploration. In: Robotics and Automation (ICRA), 2013 IEEE International Conference on. pp. 3056–3061.

Yamamoto, T., Wettels, N., Fishel, J., Lin, C.-H., Loeb, G., 2012. Biotac biomimetic multi-modal tactile sensor. Journal of the Robotics Society of Japan 30 (5), 496–498.

Yuan, X., Li, H., Sun, K., 2011. The cut sets, decomposition theorems and representation theorems on intuitionistic fuzzy sets and interval valued fuzzy sets. Science China Information Sciences 54 (1), 91–110.
URL http://dx.doi.org/10.1007/s11432-010-4078-6

Yuji, J., Sonoda, C., Oct 2006. A pvdf tactile sensor for static contact force and contact temperature. In: 2006 5th IEEE Conference on Sensors. pp. 738–741.

Yussof, H., Masahiro, O., Hirofumi, S., Nobuyuki, M., 2009. Tactile Sensing-based Control System for Dexterous Robot Manipulation. Springer Netherlands, Dordrecht, pp. 199–213.
URL http://dx.doi.org/10.1007/978-1-4020-8919-0_15

Zadeh, L., 1965. Fuzzy sets. Information and Control 8 (3), 338–353.
URL http://www.sciencedirect.com/science/article/pii/S001999586590241X

Zhang, H., So, E., Feb 2002. Hybrid resistive tactile sensing. IEEE Transactions on Systems, Man, and Cybernetics, Part B (Cybernetics) 32 (1), 57–65.

Zhang, T., Liu, H., Jiang, L., Fan, S., Yang, J., Feb 2013. Development of a flexible 3-d tactile sensor system for anthropomorphic artificial hand. IEEE Sensors Journal 13 (2), 510–518.

Zimmermann, H., 2001. Fuzzy Set Theory - and Its Applications. Springer Netherlands.
URL https://books.google.co.uk/books?id=Uqtwf6bcUxMC

APPENDIX

A

Appendix A

This appendix chapter includes tables outlining detailed results from the BPM, RR, PPI and BBI measurements outlined in Chapter 5.

Calculation of the heart rate BPM for three datasets collected per subject, the accuracy of the calculated BPM and the heart rate classification of either normal heart rate, bradycardic or tachycardic can be seen in Table A.1 and Table A.2. Table A.1 presents all results for the approach using a two stage filtering/smoothing process (i.e. using low pass filtering and discrete wavelet transform (DWT) smoothing). Results for the two stage filtering approach with semi-automatic thresholding are presented in the column labelled "2 Stage Filtering Semi-automatic (2SFS)". Results for the two stage approach with fully automatic thresholding are presented in the column labelled "2 Stage Filtering Fully-automatic (2SFF)". Table A.2 presents all results for the three stage filtering/smoothing process (i.e. using low pass filtering, DWT and lateral inhibition smoothing). Results for the three stage approach with semi-automatic thresholding are presented in the column labelled "3 Stage Filtering Semi-automatic (3SFS)" and the results for the three stage approach with fully automatic thresholding are presented in the column labelled "3 Stage Filtering Fully-automatic (3SFF)". The actual BPM measured from the subject's wrist by a trained medical professional for each subject is also stated in Table A.1 and Table A.2 in the column labelled "Actual BPM". The difference between each of the calculated values and the actual BPM is stated in each table for each dataset in the column next to each calculated value and labelled as the method abbreviation followed by "diff". The classification of the subject's heart rate based on the calculated BPM values is stated for each dataset in the column next to the accuracy column and labelled as the method abbreviation followed by "class" in each table. The classification is labelled as either bradycardic ("B") for a BPM value less than 60BPM, normal ("N") for a BPM value less between 60-100BPM or tachycardic ("T") for a BPM value greater than 100BPM. The BPM measured from each subject at each set using the Android smart-phone application (Mellado, 2013) is also presented in the column labelled "Smart Phone Application (SPA)" in each table.

The calculated RR for each set of data for each subject, the accuracy of the calculated RR in comparison to the measured RR by a trained medical professional and the classification of the subject's breathing can be seen in Table A.3,

Table A.1: Table comparing the BPM experimental results using the two stage filtering/smoothing approach.

Subject	Set	Actual BPM	sp BPM	2SFS	2SFS diff	2SFS class	2SFF	2SFF diff	2SFF class
1	1	73	88	73	0	N	66	-7	N
	2	73	86	71	-2	N	63	-10	N
	3	73	81	74	+1	N	65	-8	N
2	1	74	81	70	-4	N	68	-6	N
	2	74	93	75	+1	N	75	+1	N
	3	74	77	73	-1	N	69	-5	N
3	1	67	71	69	+2	N	73	+6	N
	2	67	71	64	-3	N	70	+3	N
	3	67	75	67	0	N	73	+6	N
4	1	76	81	75	-1	N	65	-11	N
	2	76	107	76	0	N	65	-11	N
	3	76	85	76	0	N	62	-14	N
5	1	66	92	68	+2	N	65	-1	N
	2	66	119	64	-2	N	60	-6	N
	3	66	88	66	0	N	64	-2	N
6	1	87	77	89	+2	N	89	+2	N
	2	87	85	88	+1	N	88	+1	N
	3	87	74	86	-1	N	84	-3	N
7	1	82	97	84	+2	N	75	-7	N
	2	82	89	81	-1	N	79	-3	N
	3	82	83	80	-2	N	80	-2	N
8	1	63	97	50	-13	B	54	-9	B
	2	63	65	63	0	N	65	+2	N
	3	63	89	63	0	N	66	+3	N
9	1	72	93	72	0	N	72	0	N
	2	72	91	72	0	N	76	+4	N
	3	72	115	73	+1	N	76	+4	N
10	1	76	87	76	0	N	74	-2	N
	2	76	65	77	+1	N	77	+1	N
	3	76	97	79	+3	N	79	+3	N
11	1	71	95	71	0	N	71	0	N
	2	71	95	72	+1	N	72	+1	N
	3	71	85	72	+1	N	71	0	N
12	1	63	85	68	+5	N	67	+4	N
	2	63	87	63	0	N	60	-3	N
	3	63	85	63	0	N	60	-3	N

Table A.2: Table comparing the BPM experimental results using the three stage filtering/smoothing approach.

Subject	Set	Actual BPM	sp BPM	3SFS	3SFS diff	3SFS class	3SFF	3SFF diff	3SFF class
1	1	73	88	78	+5	N	78	+5	N
	2	73	86	66	-7	N	69	-4	N
	3	73	81	73	0	N	78	5	N
2	1	74	81	71	-3	N	74	0	N
	2	74	93	80	+6	N	83	+9	N
	3	74	77	71	-3	N	79	+5	N
3	1	67	71	69	+2	N	76	+9	N
	2	67	71	67	0	N	81	+14	N
	3	67	75	67	0	N	77	+10	N
4	1	76	81	77	+1	N	68	-8	N
	2	76	107	76	0	N	74	-2	N
	3	76	85	75	-1	N	68	-8	N
5	1	66	92	66	0	N	70	+4	N
	2	66	119	61	-5	N	64	-2	N
	3	66	88	66	0	N	73	+7	N
6	1	87	77	89	+2	N	89	+2	N
	2	87	85	87	0	N	91	+4	N
	3	87	74	84	-3	N	89	+2	N
7	1	82	97	82	0	N	81	-1	N
	2	82	89	81	-1	N	81	-1	N
	3	82	83	80	-2	N	80	-2	N
8	1	63	97	49	-14	B	53	-10	N
	2	63	65	69	+6	N	80	+17	N
	3	63	89	63	0	N	73	+10	N
9	1	72	93	75	+3	N	76	+4	N
	2	72	91	72	0	N	78	+6	N
	3	72	115	72	0	N	73	+1	N
10	1	76	87	73	-3	N	75	-1	N
	2	76	65	76	0	N	78	+2	N
	3	76	97	78	+2	N	79	+3	N
11	1	71	95	71	0	N	83	+12	N
	2	71	95	72	+1	N	75	+4	N
	3	71	85	68	-3	N	76	+5	N
12	1	63	85	66	+3	N	80	+17	N
	2	63	87	61	-2	N	77	+14	N
	3	63	85	64	+1	N	77	+14	N

Table A.4, Table A.5 and Table A.6. Table A.3 and Table A.4 present the results from the two and three stage filtering/ smoothing method respectively when using collected absolute fluid pressure (PDC) data. Table A.5 and Table A.6 present the results from the two and three stage filtering/ smoothing method respectively when using collected thermal flow (TAC) data. Again the RR results are obtained using the semi-automatic thresholding ("2SFS") and fully automatic thresholding ("2SFF") algorithms. The actual RR measured from the subject's chest by a trained medical professional for each subject is also stated in each table in the column labelled "Actual RR". The difference between each of the calculated values and the actual RR is stated in each table for each dataset in the column labelled as the method abbreviation followed by "diff". The classification of the subject's breathing rate based on the calculated RR values is stated in each table for each dataset in the column next to the accuracy column and labelled as the method abbreviation followed by "class". The classification is labelled as either being classified as either a either slow ("S") for a value of less than 12 breaths per minute, normal ("N") for a value of between 12-20 breaths per minute or fast ("F") breathing rate over 20 breaths per minute.

Table A.7 shows the percentage of the calculated intervals between each detected pulse that were within the 25% tolerance of the average interval. Table A.8 and Table A.9 present the percentage of the calculated intervals between each detected breath that were within the 25% tolerance of the average interval using PDC data and TAC data respectively. All of the aforementioned tables present the percentage accuracy of the intervals within the tolerance for all the evaluated methods of BPM and RR calculation; the two stage filtering/ smoothing approach with semi-automatic thresholding ("2SFS") and fully automatic thresholding ("2SFF") and the three stage filtering/ smoothing method with semi-automatic thresholding ("3SFS") and fully automatic thresholding ("3SFF").

Table A.3: Table comparing the RR experimental results using the two stage filtering/smoothing approach with PDC data.

Subject	Set	Actual RR	2SFS	2SFS diff	2SFS class	2SFF	2SFF diff	2SFF class
1	1	16	17	+1	N	31	+15	F
	2	17	16	-1	N	29	+12	F
	3	17	17	0	N	36	+19	F
2	1	21	21	0	F	22	+1	F
	2	20	21	+1	N	21	+1	F
	3	21	22	+1	F	22	+1	F
3	1	16	17	0	N	18	+2	N
	2	15	15	0	N	20	+5	N
	3	17	17	0	N	26	+9	F
4	1	11	11	0	S	22	+11	F
	2	12	12	0	N	17	+5	N
	3	11	12	+1	N	12	+1	N
5	1	10	10	0	S	20	+10	N
	2	11	11	0	S	14	+3	N
	3	11	11	0	S	17	+6	N
6	1	12	12	0	N	11	-1	S
	2	11	12	+1	N	12	+1	N
	3	11	11	0	S	11	0	S
7	1	13	14	+1	N	20	+7	N
	2	14	14	0	N	28	+14	F
	3	13	16	+3	N	24	+11	F
8	1	10	6	-4	S	6	-4	S
	2	10	10	0	S	23	+13	F
	3	9	7	-2	S	9	0	S
9	1	8	8	0	S	25	+17	F
	2	7	7	0	S	24	+17	F
	3	7	7	0	S	35	+28	F
10	1	11	11	0	S	12	+1	N
	2	12	11	-1	S	14	+2	N
	3	12	12	0	N	27	+15	F
11	1	14	15	+1	N	27	+13	F
	2	13	12	-1	N	17	+4	N
	3	13	13	0	N	14	+1	N
12	1	8	8	0	S	9	+1	S
	2	8	7	-1	S	7	-1	S
	3	8	8	0	S	8	0	S

Table A.4: Table comparing the RR experimental results using the three stage filtering/smoothing approach with PDC data.

Subject	Set	Actual RR	3SFS	3SFS diff	3SFS class	3SFF	3SFF diff	3SFF class
1	1	16	17	+1	N	26	+10	F
	2	17	17	0	N	27	+10	F
	3	17	17	0	N	33	+16	F
2	1	21	21	0	F	21	0	F
	2	20	20	0	N	20	0	N
	3	21	23	+2	F	24	+3	F
3	1	16	17	+1	N	20	+4	N
	2	15	16	+1	N	18	+3	N
	3	17	17	0	N	24	+7	F
4	1	11	11	0	S	16	+5	N
	2	12	12	0	N	28	+16	F
	3	11	11	0	S	23	+12	F
5	1	10	8	-2	S	21	+11	F
	2	11	13	+2	N	27	+16	F
	3	11	11	0	S	24	+13	F
6	1	12	12	0	N	21	+9	F
	2	11	11	0	S	21	+10	F
	3	11	11	0	S	17	+6	N
7	1	13	16	+3	N	21	+8	F
	2	14	12	-2	N	21	+7	F
	3	13	15	+2	N	24	+11	F
8	1	10	8	-2	S	24	+14	F
	2	10	10	0	S	26	+16	F
	3	9	11	+2	S	24	+15	F
9	1	8	6	-2	S	22	+14	F
	2	7	8	+1	S	29	+22	F
	3	7	7	0	S	32	+25	S
10	1	11	10	-1	S	19	+8	N
	2	12	12	0	N	19	+7	N
	3	12	13	+1	N	27	+15	F
11	1	14	14	0	N	26	+12	F
	2	13	11	-2	S	15	+2	N
	3	13	11	-2	S	20	+7	N
12	1	8	8	0	S	40	+32	F
	2	8	4	-4	S	29	+21	F
	3	8	8	0	S	23	+8	F

Table A.5: Table comparing the RR experimental results using the two stage filtering/smoothing approach with TAC data.

Subject	Set	Actual RR	2SFS	2SFS diff	2SFS class	2SFF	2SFF diff	2SFF class
1	1	16	14	-2	N	20	+4	N
	2	17	17	0	N	27	+10	F
	3	17	17	0	N	27	+10	F
2	1	21	21	0	F	23	+2	F
	2	20	20	0	N	20	0	N
	3	21	22	+1	F	23	+2	F
3	1	16	17	0	N	20	+4	N
	2	15	15	0	N	16	+1	N
	3	17	24	+7	F	41	+24	F
4	1	11	11	-1	S	16	+5	N
	2	12	12	0	N	18	+6	N
	3	11	11	0	S	13	+2	N
5	1	10	10	0	S	12	+2	N
	2	11	10	-1	S	11	0	S
	3	11	12	+1	N	13	+2	N
6	1	12	12	0	N	11	-1	S
	2	11	11	0	S	11	0	S
	3	11	11	0	S	11	0	S
7	1	13	13	0	N	14	+1	N
	2	14	14	0	N	20	+6	N
	3	13	11	-2	S	14	+1	N
8	1	10	12	+2	N	20	+10	N
	2	10	9	-1	S	9	-1	S
	3	9	9	0	S	13	+4	N
9	1	8	11	+3	N	26	+18	F
	2	7	7	0	S	16	+9	N
	3	7	7	0	S	19	+12	N
10	1	11	11	0	S	17	+6	N
	2	12	11	-1	S	19	+7	N
	3	12	12	0	N	24	+12	F
11	1	14	14	0	N	30	+16	F
	2	13	12	-1	N	15	+2	N
	3	13	13	0	N	13	0	N
12	1	8	8	0	S	15	+7	N
	2	8	5	-3	S	9	+1	S
	3	8	8	0	S	14	+6	N

Table A.6: Table comparing the RR experimental results using the three stage filtering/smoothing approach with TAC data.

Subject	Set	Actual RR	3SFS	3SFS diff	3SFS class	3SFF	3SFF diff	3SFF class
1	1	16	16	0	N	22	+6	F
	2	17	17	0	N	32	+15	F
	3	17	21	+4	N	25	+8	F
2	1	21	21	0	F	27	+6	F
	2	20	20	0	N	21	+1	F
	3	21	22	+1	F	23	+2	F
3	1	16	13	-3	N	24	+8	F
	2	15	15	0	N	27	+12	F
	3	17	17	0	N	33	+16	F
4	1	11	11	0	S	28	+17	F
	2	12	13	+1	N	28	+16	F
	3	11	11	0	S	27	+16	F
5	1	10	11	+1	S	23	+13	F
	2	11	11	0	S	19	+8	N
	3	11	12	+1	N	32	+21	F
6	1	12	12	0	N	20	+8	N
	2	11	11	0	S	14	+3	N
	3	11	11	0	S	17	+6	N
7	1	13	14	+1	N	25	+12	F
	2	14	14	0	N	27	+13	F
	3	13	12	-1	N	28	+15	F
8	1	10	13	+3	N	29	+19	F
	2	10	9	-1	S	12	+2	N
	3	9	8	-1	S	16	+7	N
9	1	8	7	-1	S	29	+21	F
	2	7	4	-3	S	24	+17	F
	3	7	7	0	S	24	+17	F
10	1	11	11	0	S	28	+17	F
	2	12	14	+2	N	32	+20	F
	3	12	11	-1	S	23	+11	F
11	1	14	14	0	N	32	+18	F
	2	13	12	-1	N	18	+5	N
	3	13	13	0	N	25	+12	F
12	1	8	6	-2	S	27	+19	F
	2	8	6	-2	S	16	+8	N
	3	8	8	0	S	21	+13	F

Table A.7: Table comparing the calculated PPIs using from PAC data.

Subject	Set	2SFS (%)	2SFF (%)	3SFS (%)	3SFF (%)
1	1	52.63	40.85	44.87	46.91
	2	48.68	46.48	39.74	45.68
	3	51.32	46.48	41.03	48.15
2	1	52.63	54.79	50.00	53.09
	2	46.05	45.33	46.25	55.42
	3	44.74	41.33	38.75	50.60
3	1	85.53	83.56	80.77	82.72
	2	61.84	68.49	66.67	59.26
	3	64.47	64.38	57.69	70.37
4	1	65.79	65.33	58.75	62.65
	2	38.16	38.67	33.75	34.94
	3	56.58	52.00	56.25	50.60
5	1	46.05	41.33	43.75	45.78
	2	60.53	64.00	63.75	55.42
	3	71.05	64.00	65.00	60.24
6	1	98.88	98.88	98.88	98.88
	2	95.51	95.51	94.38	97.80
	3	94.38	92.13	92.13	94.51
7	1	78.65	68.54	70.79	68.13
	2	98.88	98.88	98.88	96.70
	3	97.75	96.63	97.75	95.60
8	1	82.02	88.76	79.78	83.52
	2	97.75	91.01	76.40	47.25
	3	89.89	89.89	79.78	63.74
9	1	85.39	84.27	80.90	81.32
	2	74.16	71.91	70.79	61.54
	3	79.78	77.53	75.28	72.53
10	1	92.13	88.76	82.02	80.22
	2	97.75	96.63	92.13	91.21
	3	95.51	94.38	93.26	90.11
11	1	57.30	56.18	49.44	40.66
	2	83.15	82.02	74.16	64.84
	3	87.64	91.01	78.65	75.82
12	1	67.42	65.17	64.04	46.15
	2	74.16	71.91	74.16	46.15
	3	74.16	77.53	71.91	46.15

Table A.8: Table comparing the calculated BBIs using from PDC data.

Subject	Set	2SFS (%)	2SFF (%)	3SFS (%)	3SFF (%)
1	1	23.53	64.52	70.59	42.31
	2	64.71	48.39	88.24	33.33
	3	47.06	52.78	52.94	51.52
2	1	95.24	77.78	100.00	69.70
	2	95.24	77.78	95.24	66.67
	3	90.91	75.00	91.30	63.64
3	1	88.24	66.67	88.24	45.45
	2	82.35	36.11	76.47	24.24
	3	52.94	47.22	41.18	30.30
4	1	77.27	66.67	78.26	39.39
	2	86.36	47.22	78.26	18.18
	3	86.36	58.33	86.96	9.09
5	1	63.64	52.78	78.26	24.24
	2	72.73	47.22	56.62	18.18
	3	72.73	33.33	73.91	15.15
6	1	68.18	44.44	73.91	30.30
	2	95.45	58.33	91.30	39.39
	3	86.36	52.78	86.96	30.30
7	1	81.82	41.67	56.62	21.21
	2	59.09	50.00	47.83	24.24
	3	45.45	47.22	47.83	27.27
8	1	54.55	52.78	52.17	12.12
	2	54.55	38.89	47.83	24.24
	3	72.73	36.11	43.48	18.18
9	1	59.09	33.33	47.83	28.57
	2	45.45	47.22	47.83	25.71
	3	50.00	52.78	43.48	22.86
10	1	72.73	69.44	73.91	22.86
	2	72.73	38.89	65.22	17.14
	3	72.73	47.22	65.22	17.14
11	1	40.91	38.89	52.17	45.71
	2	72.73	36.11	73.91	37.14
	3	77.27	58.33	69.57	28.57
12	1	50.00	44.44	60.87	30.00
	2	77.27	58.33	60.87	17.50
	3	72.73	55.56	69.57	20.00

Table A.9: Table comparing the calculated BBIs using from TAC data.

Subject	Set	2SFS (%)	2SFF (%)	3SFS (%)	3SFF (%)
1	1	80.00	40.00	87.50	34.78
	2	70.59	55.56	23.53	50.00
	3	41.18	33.33	19.05	43.75
2	1	79.17	58.54	85.71	24.24
	2	83.33	68.29	95.24	60.61
	3	91.67	70.73	95.45	66.67
3	1	88.24	51.85	57.14	31.25
	2	82.35	62.96	52.38	12.50
	3	37.50	43.90	28.57	27.27
4	1	83.33	41.46	63.64	15.15
	2	79.17	41.46	95.45	27.27
	3	91.67	48.78	86.36	27.27
5	1	79.17	39.02	72.73	33.33
	2	83.33	53.66	81.82	27.27
	3	70.83	41.46	63.64	27.27
6	1	70.83	56.10	72.73	30.30
	2	79.17	56.10	90.91	24.24
	3	70.83	51.22	86.36	36.36
7	1	83.33	51.22	72.73	15.15
	2	70.83	39.02	72.73	18.18
	3	70.83	41.46	81.82	15.15
8	1	62.50	51.22	59.09	15.15
	2	62.50	51.22	68.18	27.27
	3	54.17	51.22	59.09	33.33
9	1	62.50	36.59	59.09	18.18
	2	54.17	29.27	54.55	30.30
	3	62.50	39.02	54.55	27.27
10	1	75.00	29.27	63.64	18.18
	2	66.67	26.83	54.55	18.18
	3	70.83	36.59	63.64	15.15
11	1	66.67	43.90	63.64	15.15
	2	70.83	39.02	86.36	33.33
	3	79.17	53.66	90.91	27.27
12	1	75.00	46.34	77.27	9.09
	2	70.83	41.46	81.82	18.18
	3	66.67	48.78	68.18	12.12

APPENDIX

B

Appendix B

This appendix chapter presents a table outlining detailed results for each subject and dataset collected for the CRT measurements outlined in Chapter 6.

Table B.1: Table outlining all of the calculated CRT experimental results

Subject	**Set 1**	**Set 2**	**Set 3**
1	0.976	1.082	0.909
2	0.823	0.842	0.551
3	0.681	0.933	0.995
4	1.152	1.222	0.976
5	1.302	1.085	1.877
6	0.759	3.554	0.832
7	0.943	0.940	1.121
8	1.264	0.875	1.102
9	6.983	1.091	3.242
10	0.935	0.908	1.121
11	1.091	5.019	0.978
12	1.309	1.010	1.012